Optimization and new applications of edge-illumination based X-ray phase contrast CT

Anna Zamir

Department of Medical Physics and Biomedical Engineering

UCL

A thesis submitted for the degree of

Doctor of Philosophy

October, 2017

I, Anna Zamir confirm that the work presented in this thesis is my own. Where information has been derived from other sources, I confirm that this has been indicated in the thesis.

Signed: 

Abstract

The Edge Illumination (EI) method is a phase contrast imaging technique suitable for use with conventional X-ray sources, which has demonstrated its great potential for translation into real-world environments. The increase in image contrast provided by it, in particular for low-absorbing materials, along with its ability to be operated as a computed tomography (CT) modality, make it an especially advantageous technique for biomedical applications.

The work presented in this thesis aimed to develop new image acquisition and processing strategies to further advance the current capabilities of EI CT, such that it could be used in a robust way for a wide range of biomedical applications. This was achieved by the development of two retrieval algorithms, which are required for the extraction of quantitative information of various sample properties.

The first algorithm targets applications which involve high-resolution, multi-modal lab-based CT scans. It has been shown that, during these long scans, the variation in system parameters across the field-of-view and over time can lead to significant image artefacts in reconstructed CT slices. The proposed algorithm is capable of correcting for both types of variations, leading to the quantitative retrieval of sample properties from long CT scans in non-ideal environments.

The second algorithm was aimed at applications which require fast CT scans, possibly at the expense of spatial resolution and quantitative information. A previously developed algorithm enabled a substantial reduction in scan times for homogeneous samples, by reducing the number of required images per angular view. The new algorithm presented here has extended the previous one to non-homogeneous samples, therefore expanding the range of objects which could benefit from a reduction in scan times through use of this approach.

In addition, perinatal post-mortem imaging has been identified as a new biomedical application which could benefit from EI CT in the future. Promising results are reported from a proof-of-principle scan carried out using a gold standard X-ray phase contrast imaging method at a synchrotron.

Impact Statement

The developments presented in this thesis have led to the optimization of the Edge Illumination computed tomography (CT) imaging method. Using a simple experimental setup, the Edge Illumination method is capable of detecting the refraction of X-rays, in addition to their absorption, thus leading to increased image contrast when compared to conventional X-ray imaging.

In this thesis, through collaboration with radiologists from Great Ormond Street Hospital, perinatal post-mortem imaging has been identified as a new application which could benefit from the use of the Edge Illumination method. Furthermore, by developing two new algorithms, the method has been optimized for the performance of both fast CT scans of samples made of more than one material, and quantitative, high-resolution scans acquired in non-ideal environments. As such, this research provides a significant contribution to making Edge Illumination a robust technique which can be used in different imaging environments, and which has the flexibility to be adjusted for optimal use depending on the application. Therefore, this work forms an integral part of the transformation of Edge Illumination CT into a widely used imaging tool. For example, the "fast" algorithm working with non-homogeneous samples can open the way to *in-vivo* pre-clinical imaging, while the quantitative, high-resolution algorithm could be suitable for use in complex cases in e.g. virtual histology.

In addition to the direct impact on the optimization of the Edge Illumination method, this work could be potentially used by other research groups to achieve similar results using different X-ray phase contrast methods. Should these developments contribute to the construction of a commercial imaging system capable

of providing increased image contrast in addition to the extraction of quantitative sample information, this could have significant impact on a range of research fields. While the work presented here focused on applications in the biomedical field, this technology could benefit other fields, such as, for example, materials science. Examples of potential outcomes, biomedical and not, include the development of new therapies by monitoring the effect of a given treatment in a small-animal model, the design and characterization of scaffolds used for tissue engineering purposes, and the quantitative evaluation and analysis of materials of interest.

Acknowledgements

I feel incredibly fortunate to have been surrounded by so many supportive people, who became true friends, throughout my time at UCL. I would first like to thank Prof. Alessandro Olivo, my primary supervisor, for his support over the last four years. His scientific enthusiasm is infectious, and he is not only a world-class scientist, but an attentive, supportive mentor who cares about the personal wellbeing of his students. I would not have been able to complete this thesis without both his academic mentoring and his continuous reassurance. I would also like to express my deep gratitude to Dr. Charlotte Hagen, my second supervisor, for sharing her knowledge and experience in Edge-Illumination CT, and for her ongoing support, encouragement and patience.

Many thanks go to my colleagues at the Advanced X-ray Imaging group at UCL, all of which I am now proud to call my friends. In particular I would like to thank Dr. Marco Endrizzi and Dr. Paul Diemoz for their fruitful discussions and invaluable help during the development of the retrieval algorithms presented in this thesis. I owe special thanks to Dr. Fabio Vittoria, who spent countless hours sharing his knowledge with me and took a keen interest in my project; I will always be grateful for his patience and friendship. I would also

like to thank Dr. Gibril Kallon, Dr. Dario Basta, Dr. Daniel O'Flynn and Chiaki Crews for their support, kind words and humor during challenging times.

I am further grateful for the support of the scientists of the ID17 beamline at the ESRF during the synchrotron experiment, and for Dr. Owen Arthurs and Prof. Neil Sebire's medical input with regard to post-mortem imaging.

I would also like to mention my cousin Adam and my friends, Roni, Rony, Marta and Elena, who were there for me all along, during good times and bad.

I will forever be grateful to the Fordham family, Caroline and David in particular, for being my London family and opening their hearts and home to me.

Special thanks go to the late Zvi Meitar of blessed memory, and his lovely wife, Ofra. Their unparalleled generosity enabled me to study at UCL, and I will always be thankful for that.

Finally, my deepest gratitude goes to the most important people in my life, my family. I thank my husband and best friend, Dan, my parents, Muki and Galia, my brother, Asaf, and my sister, Daniella. Their unrelenting belief in me made me believe in myself, and I would not have been the person I am today without them.

Contents

List of Figures

List of Tables

Acronyms

ABI	Analyzer Based Imaging
CNR	Contrast-to-Noise Ratio
COR	Centre-of-Rotation
CT	Computed Tomography
EI	Edge Illumination
ESRF	European Synchrotron Radiation Facility
FBP	Filtered Back-Projection
FOV	Field-of-View
FSP	Free-Space Propagation
FST	Fourier Slice Theorem
FT	Fourier Transform
GI	Grating Interferometry
IC	Illumination Curve
LDPE	Low-Density Polyethylene
MRI	Magnetic Resonance Imaging
NHS	National Health Service
NPS	Noise Power Spectrum
PMMA	Polymethyl Methacrylate

RC	Rocking Curve
RHS	Right-Hand Side
RID	Refractive Index Decrement
SR	Synchrotron Radiation
TIE	Transport-of-Intensity Equation
XPCi	X-ray Phase Contrast imaging

Introduction

X-rays have been used for imaging since they were first discovered by Wilhelm Roentgen in 1895 [5]. Early experiments of the then unknown radiation, demonstrated that X-rays could pass through most opaque objects, yet denser materials such as bone and metals seemed to stop them. The potential of using this characteristic feature for the purpose of imaging was immediately recognized, and a multitude of both medical and industrial applications quickly developed. Soon after early experiments, reports of symptoms such as hair loss and burns were filed, yet the general assumption was that exposure to this radiation, which could not be seen or felt, posed no risk.

Decades of research have followed, and it is now known that X-rays are a form electromagnetic radiation, with wavelengths in the range of 0.1-100 Å and energies around 0.1-100 keV. These short wavelengths, which are comparable to the size of an atom, enable X-rays to pass through matter, unless an interaction on the atomic level occurs, in which case X-rays can be absorbed or scattered. It is these interactions which form the basis of X-ray imaging, as the contrast in a conventional X-ray image is attenuation-based, i.e. it is the difference in the amount of X-ray attenuation by different materials which enables the visualization of a detail against its background. However, the mechanism by which X-rays

are attenuated involves the transfer of energy between an X-ray and an electron, which can, as a consequence, be freed from the atom. X-radiation is therefore a form of ionizing radiation, capable of harming and destroying living cells.

While X-ray production, detection and protection have been all greatly improved over the last century, the underlying principles of X-ray imaging remained the same: an X-ray beam produced by a source is directed at the object of interest. X-rays which pass through the object are then measured by an X-ray detector, placed behind the object. The intensity of the detected X-rays over the field-of-view (FOV) then forms the image.

The technique's relatively simple and inexpensive setup has resulted in its widespread global use, with a variety of applications in both medicine and industry. Notwithstanding the technique's commercial success, for many decades it suffered from two main drawbacks. The first, the problem of overlapping structures in a planar image, was solved in 1971 by the development of the first computed tomography (CT) scanner, marking a significant advancement in the field of X-ray imaging. By acquiring multiple images over an angular range and using dedicated algorithms, the entire volume of an object could be reconstructed. The second limitation however, is inherent to the contrast mechanism employed, causing the technique to suffer from poor visualization of low-attenuating materials, or poor differentiation between ones with similar attenuation properties. In particular, this poses a problem for many medical applications of X-ray imaging, where it is necessary to visualize different soft tissues. In certain applications, soft tissue contrast could be improved by the use of radio-opaque contrast agents. However, these can cause adverse reactions and, since they increase X-ray absorption, their use also inevitably leads to the undesired outcome of an increased dose.

X-ray phase contrast imaging (XPCi) techniques, on the other hand, have the potential to overcome this limitation since as the name suggests, the main mechanism which these rely on to generate image contrast is different to X-ray attenuation. Instead, XPCi techniques are sensitive to the phase shifts that an X-ray beam experiences as it passes through matter [6]. These phase effects manifest as interference patterns or as X-ray refraction, and are often considerably stronger than the associated attenuation effects, thereby leading to increased image contrast. Although the first XPCi technique was developed in the 1960's, it was only in the 1990's that extensive research in XPCi began, and different techniques emerged [7]. So far, these techniques have repeatedly demonstrated their capability to significantly improve image quality in comparison to attenuation-based images, however, specialized setups are required. These specialized setups are currently the main limitation of XPCi, preventing its widespread use in clinics and industrial environments. Therefore, while most techniques require the use of a synchrotron facility, there is a growing interest in developing XPCi methods compatible with laboratory X-ray sources [8]. In particular, such developments could have a significant impact on the biomedical field, by enabling the visualization of soft tissue details, previously unseen by conventional X-ray imaging, in a clinical setting.

The Edge Illumination (EI) method is currently one of the most promising XPCi techniques for translation to clinical and industrial environments. Although it was first developed at a synchrotron facility [9], the method is achromatic [10] and does not require coherent radiation [11], making its implementation with commercially available X-ray equipment possible. Since it was first invented in the late 1990's, different approaches to image acquisition and processing schemes

were developed, such that EI could be used for a vast range of applications. Indeed, experiments were performed in diverse fields including security scanning [12], paleontology [13], tissue engineering [14], materials science [15] and mammography [16]. In EI, by using the same simple setup and making modifications to the imaging parameters, it is possible to increase the spatial resolution above the one determined by the detector pixel size [17], and to retrieve up to three different contrast channels [3].

In 2014, the EI method has been adapted to a CT modality, and the first results of an EI CT scan acquired with synchrotron radiation have been published [18]. Shortly after, the laboratory EI system has been modified to enable CT imaging and further CT-related studies have been performed ever since. Although the EI method is capable of providing high-resolution, multi-modal images, these advancements involve acquiring multiple images per projection, leading to an increase in scan time and dose. While certain applications have less stringent dose and scan duration restrictions, when high-resolution, multi-modal scans are performed in CT mode, scans can last hours or even days, leaving the system exposed to environmental changes. When these are not accounted for, they can lead to severe artefacts in the reconstructed CT slices, compromising the accuracy of the retrieved values. On the other hand, in many applications in the biomedical field it is essential that the delivered dose is minimized and scan times are reduced, potentially at the expense of retrieving strictly quantitative information.

The work presented in this thesis aimed to optimize both the acquisition and processing of CT data acquired using the EI laboratory system, in particular for biomedical applications. First, the possibility of using EI CT as an alternative to perinatal autopsy has been considered as a new, potential application of the

method. To test this, a proof-of-principle scan was performed using a gold standard approach, involving the use of another XPCi technique and synchrotron radiation. Analysis of the data by radiologists confirmed that XPCi has the potential to provide diagnostically relevant results, and that further studies should be pursued in the future in a laboratory setting. The next study aimed to reduce artefacts arising from system instabilities during long, laboratory-based CT scans, by investigating and analyzing different sources of error. Following simulated and experimental studies, the main sources of error have been identified and a "local" retrieval algorithm was developed to account for them and reduce their associated image artefacts. In contrast to the local retrieval algorithm aimed at long CT scans, a different retrieval algorithm was developed in an additional study to enable the performance of fast CT scans. Thus continuous CT scans can be performed using this "single-image" retrieval algorithm which requires only one image per projection and can be applied to objects containing a range of materials.

The first chapter in this thesis will focus on conventional, attenuation-based X-ray imaging. An overview of the different interactions of X-rays and matter will be given, explaining the mechanisms by which X-rays are attenuated. The basic principles of X-ray imaging will then be presented, covering both planar and CT imaging. The second chapter focuses on XPCi, providing an overview of the most prominent current techniques, with a specific emphasis on EI. Results from the proof-of-principle experiment for using XPCi as an alternative to perinatal autopsy are reported and discussed in the third chapter. The fourth chapter presents work done on image artefacts in long, laboratory-based CT scans. The local retrieval algorithm is developed and the resultant improvement in image

quality of a biological sample is demonstrated. In the fifth chapter, the multi-material single-image retrieval algorithm is developed, and its quantitativeness and associated improvement in image quality are studied using both simulated and experimental data.

The work of chapters 3-5 each resulted in a peer-reviewed publication:

- A. Zamir, O.J. Arthurs, C.K. Hagen, P.C. Diemoz, T. Brochard, A. Bravin, N.J. Sebire, and A. Olivo, **X-ray phase contrast tomography; proof of principle for post-mortem imaging.** *Br. J. Radiol.,* **89**:20150565, 2016.

- A. Zamir, M. Endrizzi, C.K. Hagen, F.A. Vittoria, L. Urbani, P. De Coppi, and A. Olivo, **Robust phase retrieval for high resolution edge illumination X-ray phase-contrast computed tomography in non-ideal environments.** *Sci. Rep.,* **6**:31197, 2016.

- A. Zamir, P.C. Diemoz, F.A. Vittoria, C.K. Hagen, M. Endrizzi, and A. Olivo, **Edge illumination X-ray phase tomography of multi-material samples using a single-image phase retrieval algorithm.** *Opt. Exp.,* **25**:11984-11996, 2017.

1

Attenuation X-ray imaging

In this chapter, the background to conventional, attenuation-based X-ray imaging is provided. First, for completeness, a brief overview of the different interactions of X-rays with matter will be given, providing more information about the mechanisms by which X-rays are absorbed and scattered. The basic principles of X-ray imaging will then be presented, providing details of a typical imaging setup and key equations by which image formation can be described. In the last section, the adaptation of X-ray imaging into a 3-dimensional imaging modality, namely CT, will be discussed. The theoretical background will be presented, along with the associated adaptations of the system setup and image reconstruction procedures. For a more detailed description of these topics, readers are referred to several textbooks [1, 19, 20, 21].

1.1 X-ray interactions with matter

When X-rays transverse matter, apart from the possibility of being transmitted without any interaction, they can be absorbed or scattered [21]. The combination of the latter two results in X-ray attenuation which in this context is defined as the removal of photons from the primary beam. There are four main mechanisms by which these processes occur, namely (a) photoelectric absorption, (b) Compton scattering, (c) coherent scattering and (d) pair production. The former two are the main contributers to the attenuation contrast in an X-ray image, as pair production occurs at energies well beyond those used in diagnostic X-ray imaging, and the occurrence of coherent scattering is low with respect to the other interactions. In order to describe these interactions, it is useful to model an atom as consisting of a positively charged nucleus surrounded by negatively charged electrons. The electrons are bound in different shells with respective quantized binding energies, the latter determined by the strength of the electrostatic attraction between the electrons and the nucleus.

In photoelectric absorption, an X-ray photon is absorbed fully by an inner shell electron, which in turn is liberated from its shell. The kinetic energy of the ejected electron is then given by the difference between the photon's energy and the electron's binding energy. The vacant electron position is then filled by a higher shell electron, a transition that results in the emission of radiation with energy equal to the energy difference of the two shells, and is therefore characteristic to the atom. In some cases, the excess energy can be emitted by liberating an outer shell electron, which is then referred to as an Auger electron. The probability of photoelectric absorption is approximately proportional to Z^3/E^3, where Z is

the atomic number and E is the X-ray energy. This however is not valid when the energy is slightly higher than the binding energies of inner shell electrons, in which case there is an abrupt increase in the probability of this interaction. In general, the occurrence of photoelectric absorption is significantly higher for low energy photons and high Z materials.

Compton scattering is an inelastic process in which an X-ray photon interacts with an outer shell electron. Here, the X-ray's energy is considerably larger than the binding energy of the electron, which can therefore be considered as free. During the interaction, there is an energy and momentum transfer between the photon and the electron. As a result, the electron is ejected, and the photon is scattered with a reduced energy. The change in energy can be calculated by considering the conservation of both energy and momentum during the interaction. The probability of Compton scattering is independent of Z, and varies proportionally with ρ/E, where ρ is the density of the material.

Coherent scattering occurs at low X-ray energies, when the latter is typically below an electron's binding energy. Here, the photon interacts with the whole atom, causing the oscillation of the entire electron cloud. The latter then emits radiation with the same energy as that of the incident photon, the combination of which with the original wave results in a change in the X-ray propagation direction (predominantly forward scatter at small angles). Coherent scattering however is not significant in diagnostic X-ray imaging due to its relative low probability of occurrence, and the fact that the photon is emitted in the forward direction with no loss of energy, often causing negligible attenuation.

The last interaction, pair production, is mentioned here for sake of completeness, as it occurs only for photons with energies above 1.02 MeV and is hence irrelevant

in relation to X-ray imaging. In this case, the photon interacts with the nucleus' electrostatic field, causing the former to convert its energy into an electron and positron pair. Any energy in excess of the threshold required to satisfy the mass-energy equivalence (1.02 MeV being twice the electron's rest mass) is converted into kinetic energy with which the electron and positron travel through matter until they are fully absorbed or annihilate, respectively.

In general, the relative contributions of these interactions vary depending on the sample material and X-ray energy. However, at energies used for diagnostic radiology (5-150 keV), X-ray attenuation occurs mainly due to a combination of photoelectric absorption and Compton scattering. For soft tissues, the photoelectric effect is dominant at lower energies (up to about 30 keV), while Compton scattering becomes more significant and the dominant interaction at higher energies ($E >\sim 30$ keV). For denser materials, such as bones, the photoelectric effect is the dominant interaction over a wider range of energies (up to about 50 keV) [19]. In diagnostic radiology, these higher energies are therefore used for imaging thicker body sections, or ones containing bones [20].

1.2 Planar X-ray imaging

X-ray imaging was first performed shortly after the discovery of X-rays in 1895, and has been since vastly applied to medical investigations, material testing and security inspections [5]. A typical imaging setup is shown in Fig. 1.1. An X-ray source is used to generate an X-ray beam which is directed at the object under investigation. The transmitted X-rays are then detected by an X-ray detector, placed immediately after the object. Since the attenuation of X-rays varies with

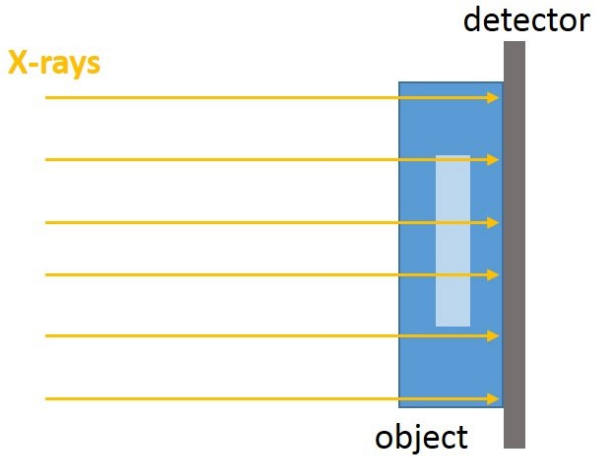

Figure 1.1: A schematic of a typical attenuation-based X-ray imaging system.

material type and density, the distribution of detected X-rays over the FOV contains information about the internal structure of the object. In general, the attenuation of the incident beam by the object can be expressed by the Beer-Lambert Law [22]:

$$I_1 = I_0 e^{-\mu t} \tag{1.1}$$

where I_0 and I_1 are the incident and transmitted beam intensities respectively, t is the material's thickness in the direction of X-ray propagation, and μ is the linear attenuation coefficient which varies with material type and density, and with X-ray energy. If the object is composed of more than one material, then the incident beam will be attenuated by different amounts as it traverses different materials along its path. For example, consider the case shown in Fig. 1.2, where a "target" detail with attenuation coefficient μ_2 and thickness t_2 is embedded within a slab of material with attenuation coefficient μ_1 and of total length t_1. X-rays which traverse material 1 only, will be transmitted with an intensity given by $I_1 = I_0 e^{-\mu_1 t_1}$, while rays which pass through the part containing the target

detail, will be transmitted with intensity $I_2 = I_0 e^{-\mu_1(t_1-t_2)} e^{-\mu_2 t_2}$. The image that is produced by the detector is therefore a 2-dimensional representation of the 3-dimensional distribution of the attenuating properties of the entire object, projected onto the plane orthogonal to the direction of X-ray propagation. In the absence of scatter, the contrast between the target detail and the material within which it is embedded, is defined as [20]:

$$C = \frac{I_1 - I_2}{I_1} = 1 - e^{(\mu_1 - \mu_2)t_2}, \tag{1.2}$$

where the expressions previously developed for I_1 and I_2 were used. It is therefore apparent that the contrast between a detail of interest and its background increases with the thickness of the detail and with the difference between the attenuation properties of the two materials. It should be noted that since the attenuation coefficient reduces with increasing energy, so does the contrast. For this reason, the energy used in conventional X-ray imaging is chosen as a trade-off between high image contrast and low deposited dose.

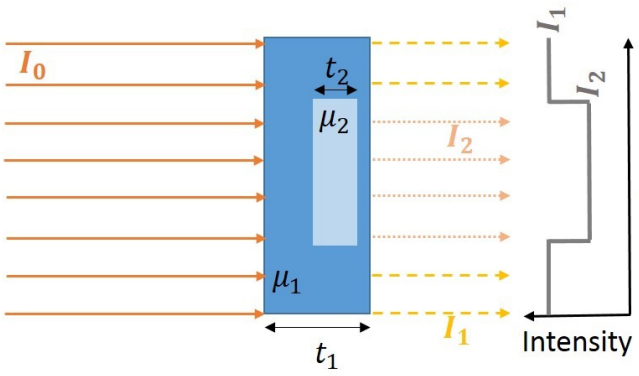

Figure 1.2: The transmitted intensity varies depending on the type of materials and their thicknesses that X-rays encounter along their path.

Planar X-ray imaging (also termed projection radiography) is currently the most

commonly used imaging modality in diagnostic medicine in the UK, with 22.6 million procedures performed in 2016 by the NHS (compared with 8.92 million ultrasound examinations, which are the following most common imaging modality) [23]. Radiologists are trained to observe the 2-dimensional projection image and deduce diagnostic information about the organs of interest, which might appear as overlapping with other organs. While this is possible and indeed useful for visualizing certain anatomical structures (e.g. bones, chest, breast etc.), the issue of overlapping structures often makes the detection of abnormalities in other organs (e.g. heart, abdomen etc.) quite challenging. This difficulty was overcome by the development of X-ray CT scanners, which is the topic of the following section.

1.3 Computed tomography

The invention of the first commercial CT scanner in 1971 is often regarded to as the greatest step forward in radiology since Rontgen's discovery [5]. The significant impact of this invention was further recognized by awarding Sir Godfrey Hounsfield and Allan Cormack the 1979 Nobel Prize for Physiology and Medicine. However, the mathematical background which CT reconstruction relies on was developed much earlier, in 1917, when Johann Radon first introduced the "Radon Transform" and its inverse transformation. Radon's work demonstrated the very core principle underpinning CT, i.e. that a volumetric function can be reconstructed from 2-dimensional projections of the function, taken over an angular range.

Today, different types of CT reconstruction algorithms exist, all of which manipu-

late the acquired projection data to reconstruct slices representing the distribution of the object's properties in space. While there is a growing interest in iterative algorithms which are based on algebraic or statistical approaches, these are beyond the scope of this thesis. Instead, here we will focus on the most commonly used reconstruction algorithm, namely filtered back-projection (FBP). There are

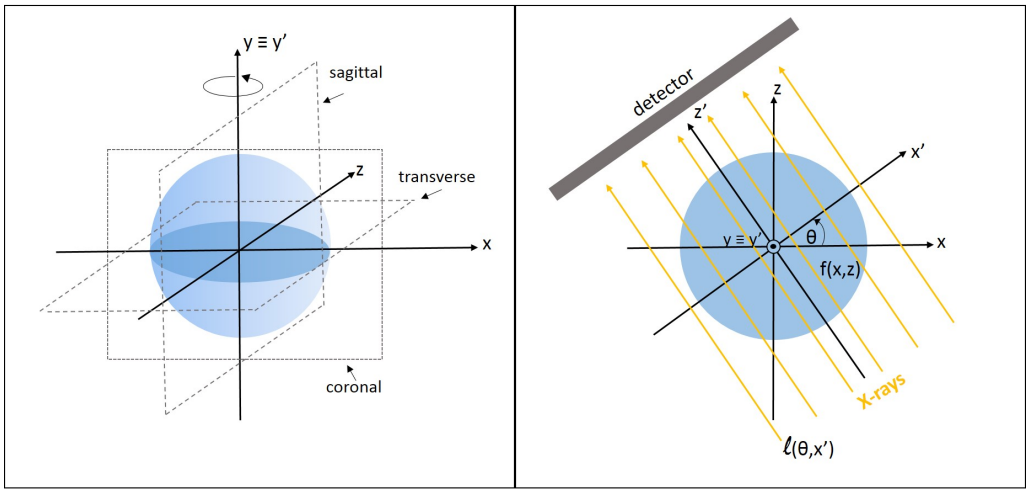

Figure 1.3: Frame of reference for a stationary object and a rotating imaging system.

two key mathematical relations which form the basis of the FBP reconstruction algorithm: the Radon transform and the Fourier Slice Theorem. Consider the schematic shown in Fig. 1.3 demonstrating a simplified CT setup in which a stationary object is illuminated by a parallel X-ray beam, with the X-ray source and detector rotating around the object. The function $f = f(x, z)$ represents the distribution of an unknown quantity in the transverse plane xz, which is to be reconstructed. Here, xyz describes the stationary frame of reference, and $x'y'z'$ is obtained by rotating the former by an angle θ and noting that $y \equiv y'$. At each

rotation angle θ, the path followed by an X-ray can be described by the line:

$$l(\theta, x') = x\cos\theta + z\sin\theta. \tag{1.3}$$

For any value of θ and assuming a constant $y = y'$, the Radon transform relates the function f to the value of its integral over any line l parallel to the z' axis, and is defined as [1]

$$\mathcal{R}[f(x,z)](\theta, x') := g(\theta, x') = \int_{l(\theta,x')} f(x,z)dz', \tag{1.4}$$

where $\mathcal{R}$ indicates the Radon transform operator, and $g(\theta, x')$ is the Radon transform (also called "sinogram") of f, and can be thought of as a forward projection. By using a delta function, this can be rewritten as

$$g(\theta, x') = \int_{-\infty}^{\infty}\int_{-\infty}^{\infty} f(x,z)\delta(x\cos\theta + z\sin\theta - x')dxdz, \tag{1.5}$$

and its Fourier transform (FT) is given by

$$\mathcal{F}[g(\theta, x')](\omega, \theta) = \int_{-\infty}^{\infty}\int_{-\infty}^{\infty} f(x,z)e^{-i\omega(x\cos\theta + z\sin\theta)}dxdz. \tag{1.6}$$

The right-hand side (RHS) of Eq. 1.6 is the same as the 2-dimensional FT of the function f at spatial frequencies ($u = \omega\cos\theta, v = \omega\sin\theta$). This equality is known as the Fourier Slice Theorem (FST) which states that the 1-dimensional FT of a projection of a function, taken at an angle θ, is equal to the 2-dimensional FT of the function itself, along a line [1]. More specifically, the particular line is the one passing through the origin at an angle θ. This is demonstrated in Fig. 1.4

and can be expressed mathematically as [1]

$$\mathcal{F}_1[Rf(x,z)](\omega,\theta) = \mathcal{F}_2[f(x,z)](\omega\cos\theta, \omega\sin\theta). \tag{1.7}$$

Therefore, according to the FST, it should be possible to reconstruct an unknown function f from projection data acquired over an angular range, by first performing a 1-dimensional FT on each projection, hence filling the corresponding lines in the Fourier domain, and then using a 2-dimensional inverse FT to retrieve the original function. In practice this is rarely the approach taken for reconstruction, since projections are acquired at finite angular steps and the Fourier space is filled radially. Most practical algorithms which perform the Fourier transformation require data sampled on a Cartesian grid, hence an interpolation in the Fourier domain is necessary. Furthermore, the sampling distribution of the Fourier domain is denser near the origin, meaning that high frequencies, which correspond to the fine details of an object, are under-represented, thus resulting in an unsharp reconstruction.

FBP is a reconstruction algorithm which overcomes these drawbacks. The idea here is that the original object function could be reconstructed by "smearing" each projection over the object domain in the direction in which is was originally acquired. However, this backprojection procedure alone results in an unsharp reconstruction due to the reasons mentioned previously. Therefore, prior to the backprojection step, each projection is filtered. The most commonly used filter is the "Ram-Lak" filter, which amplifies the high frequencies while suppressing the low ones. Furthermore, a cutoff frequency is usually defined in order to reduce noise levels in the reconstructed image. These two steps are combined in the FBP

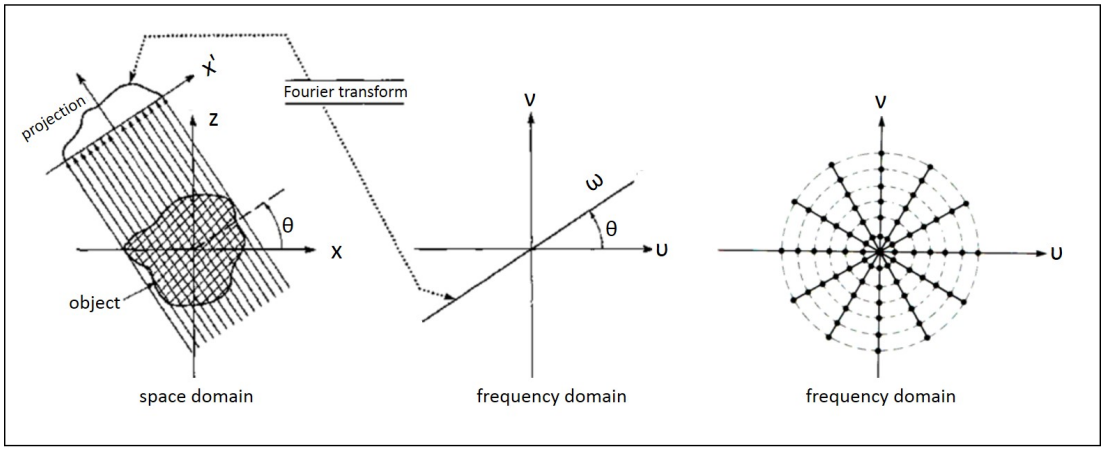

Figure 1.4: The Fourier Slice Theorem demonstrating the relationship between the object function in the space and frequency domains. Figure adapted from ref. [1].

formula with which the object function can be retrieved according to [1]:

$$\begin{aligned} f(x,z) &= FBP[g(x',\theta)](x,z) \\ &= \frac{1}{2\pi}\int_0^{\pi} \mathcal{F}^{-1}\big\{|k|\mathcal{F}[g(x',\theta)](k)\big\}(x\cos\theta + z\sin\theta)d\theta, \end{aligned} \tag{1.8}$$

where FBP represents the filtered-backprojection operator, $\mathcal{F}$ and $\mathcal{F}^{-1}$ indicate the forward and inverse Fourier transforms, respectively, and $|k|$ is the filter function applied in the Fourier domain.

In X-ray CT, it is the linear attenuation coefficient μ which is reconstructed using Eq. 1.8. This is possible since a line integral relationship exists between μ and the recorded projections, as is apparent when the Beer-Lambert law (now written in a general form for an inhomogeneous object) is rearranged:

$$g(\theta,x') = \int_{l(\theta,x')} \mu(x,z)dz' = -\ln\left(\frac{I_1(x')}{I_0(x')}\right). \tag{1.9}$$

Note that Eq. 1.8 is valid for a laminar, parallel beam. While this condition can be achieved by collimating the beam, it leads to reduced flux and increased scan times. Therefore, in practice, most laboratories use an uncollimated cone beam. The FBP formula can then be applied only in those cases where the cone angle is sufficiently small. Otherwise, data should be reconstructed using an extension of the FBP algorithm to cone beam geometries, which is however more computationally intensive. The Feldkamp-David-Kress algorithm [24] is the most commonly used cone-beam reconstruction algorithm, owing to its straightforward implementation and fast computation time; however, it is approximate by nature as it fails to satisfy Tuy's data sufficiency condition for exact cone beam reconstruction [25]. In addition, cone-beam artefacts become more prominent with an increasingly large cone angle [24, 26].

Furthermore, Eq. 1.9 assumes the use of monochromatic radiation. In reality, the linear attenuation coefficient varies with energy, hence when considering a polychromatic beam, the expression is obtained by summing the individual contributions of each energy in the spectrum. In this case, describing the recorded projections as line integrals of the object's attenuation is only approximately true, due to the object's self attenuation which leads to a change in the detected energy spectrum. When the FBP algorithm is used in situations where there is significant self-attenuation by the object, the reconstructed CT slices suffer from beam hardening artefacts [1].

Last, it should be noted that although the mathematical background presented in this chapter was derived for a frame of reference in which the X-ray source and detector rotate around a stationary object (as is the case for *in-vivo* scanners), equivalent expressions are obtained for a system in which the source and detector

are stationary, and the object is rotating. This latter configuration is the one most commonly used in prototype scanners and in micro-CT scanners, and is indeed the approach adopted in the experiments described in the following chapters.

Today, conventional X-ray imaging is an invaluable tool in a number of fields, including medicine where it is the most commonly used imaging modality, in both planar and 3-dimensional imaging. Although it causes a significant increase in scan time and dose, CT scans enable the reconstruction of an object's entire volume by stacking individually reconstructed CT slices. The rational for using CT scans for medical purposes, is that the associated increase in dose is outweighed by the gain in diagnostic information when compared to planar radiography. However, both planar and CT radiography suffer from the poor visualization of low-attenuating materials, an issue inherently related to their attenuation-based contrast. This is a problem particularly in the biomedical field, where many applications require the imaging of different soft tissue details. The next chapter describes alternative X-ray imaging methods in which image contrast is based on the refraction of X-rays instead of their attenuation, which often leads to an improved visualization of low-attenuating materials.

2

Phase contrast imaging

The previous chapter provided the background to conventional X-ray imaging, where image contrast is based on the attenuation of X-rays. However, apart from being attenuated, an X-ray beam traveling through matter also experiences phase shifts. The extent of these two effects is determined by the complex refractive index of the given material, which can be represented as [22]:

$$n(E) = 1 - \delta(E) + i\beta(E), \tag{2.1}$$

where E is the photon energy and the terms δ and β are linked to the phase and attenuation effects, respectively. The attenuation term β is related to the linear attenuation coefficient by $\mu = 2k\beta$, where $k = 2\pi/\lambda$ is the wavenumber and λ is the photon wavelength. The term δ, often referred to as the refractive index decrement (RID), is related to the material's electron density, ρ_e, via $\rho_e = k^2\delta/2\pi r_e$ where r_e denotes the classical electron radius.

Phase contrast imaging techniques are ones in which image contrast is based on

phase effects, the latter related to changes in the RID. While these phase effects are effectively ignored in a conventional, attenuation-based imaging system, the design of customized setups enables their detection. The motivation for constructing such systems lies in the fact that for many materials (in particular low attenuating materials, e.g. soft tissue) and in the energy range typically used for X-ray imaging, the RID is considerably larger than β, by up to three orders of magnitude. Therefore it follows that improved contrast can be achieved if the imaging system could be made sensitive to changes in the RID. Furthermore, it should be noted that δ and β do not depend on energy in the same way; in fact, $\delta \propto 1/E^2$ while $\beta \propto 1/E^4$ [6]. This suggests that the improvement due to phase contrast can be maintained at higher energies, hence leading to the possibility of low dose imaging.

By treating X-rays as electromagnetic waves and using the definition of the complex refractive index (Eq. 2.1) in the expression of a monochromatic plane wave propagating in the z direction, it can be shown that the total phase shift $\Phi(x, y)$ imparted on the wave as it traverses an object is given by [22]

$$\Phi(x, y) = -k \int_{object} \delta(x, y, z) dz. \tag{2.2}$$

Note that Eq. 2.2 is valid under the projection approximation, which amounts to assuming a thin object with scatterers sufficiently weak such that the ray paths are negligibly changed due to the presence of the object. Using this approximation, the total phase shift and attenuation immediately after the object (exit surface) can be expressed as the ones accumulated as the X-rays traverse a path corresponding to the one connecting the entrance and exit surfaces, in the ab-

sence of the object.

Detecting the phase shift directly however is not possible, since X-ray detectors are sensitive to changes in X-ray intensity. Therefore, in order to obtain a phase contrast image, the imaging system must be able to convert the phase shift caused by the object into intensity variations. This can be achieved by two different approaches on which XPCi methods are based. The first approach relies on the detection of interference patterns caused by the interaction of the unperturbed waves with the phase shifted wavefronts. In general, this can be achieved either by positioning the detector at an increased distance away from the object, thus allowing the beam to propagate and an interference pattern to emerge, or by means of an interferometer. The second approach involves the detection of X-ray refraction. Here, a ray-optics view is adopted, according to which the local distortion of a wavefront results in a change in the direction of X-ray propagation. The angle by which the X-ray is deviated (refraction angle) is proportional to the local variation in the phase shift, and is given by [27]

$$\alpha \cong k^{-1}|\nabla_{x,y}\Phi| = \left|\nabla_{x,y}\int_{object}\delta(x,y,z)dz\right|, \tag{2.3}$$

where $\nabla_{x,y}$ indicates the 2-dimensional gradient, resulting in the two transverse components of the refraction angle. It therefore follows that the refraction angle is greatest where the variation in phase is maximal, i.e. at the borders of an object or of details within it. Consequently, images in which the refraction angle is directly measured have an edge-enhanced appearance.

Three decades have passed between the development of the first phase contrast

technique, "Bonse-Hart interferomentry" [28], and subsequent methods such as "Analyzer-based imaging" (ABI) [29] and "Free-space propagation" (FSP, also referred to as "In-line holography") [30]. These advancements were largely facilitated by the advent of 3rd-generation synchrotrons, which produce X-radiation characterized by high coherence and high flux. Shortly after, two more methods were developed, namely "Grating interferometry" (GI) [31] and "Edge illumination" [9], both of which were first demonstrated using synchrotron radiation (SR). Today, as the performance of synchrotrons continues to improve, more scientific research based around the use of XPCi is being pursued. By harnessing the high brilliance of SR, high quality phase contrast images can be obtained in unparalleled scan times, featuring high spatial resolution and contrast. However, the limited availability of synchrotron facilities implies that there is a need to develop phase contrast methods which can be used with laboratory sources, in particular for medical applications. To a certain extent, all the above mentioned XPCi methods could be implemented with laboratory sources. However, the majority suffer from impractical scan times in a laboratory implementation (especially for CT) as a result of low available flux, due to the need for a microfocal source, or to the use of crystals or other optical elements. Today, GI and EI are the two methods which can produce phase contrast images within reasonable times with conventional, non-microfocal X-ray sources [32, 33], making them the prime candidates for translation into clinical and industrial environments.

The motivation for the work presented in this thesis was to further optimize the performance of EI CT, with a particular focus on biomedical applications carried out in a laboratory environment, thus forming a step towards the transformation of EI CT into a widely spread imaging tool. Furthermore, the following chapter

will discuss a new potential application of XPCi (perinatal post-mortem imaging) which has been investigated in a proof-of-principle experiment using the gold standard FSP technique.

The remainder of this chapter will provide an overview of the above mentioned XPCi methods. The physical principles that these rely on to generate contrast will be discussed along with descriptions of the experimental setups. The associated advantages and limitations of each method will be highlighted, and information about the most common algorithms used to retrieve phase information ("phase retrieval" algorithms) will be provided. Particular focus is given to the FSP and EI methods, as both methods were employed in the experiments described in chapters 3-5. For more information about the history and recent developments in the XPCi field, the reader is referred to several reviews [6, 7, 8].

2.1 Bonse-Hart interferometry

The first XPCi method was Bonse-Hart interferometry which was developed in 1965 [28]. In order to generate phase contrast images, the method makes use of a crystal interferometer, as shown in Fig. 2.1. The setup consists of three crystals and their alignment is as follows: first, a crystal ("splitter") is placed downstream the X-ray beam causing the beam to split into two mutually coherent beams when exiting it by means of a symmetrical Laue reflection. A second crystal ("mirror") is placed downstream which again splits both beams. At this point, if no object is present in the beams' path, two of these beams will be redirected towards each other and recombine, creating an interference pattern,

with fringes too finely spaced to be directly observed with a standard detector. This is solved by the addition of a third crystal ("analyzer") to the setup, such that the beams recombine at its surface. If an object is then placed in one of the branches of the interferometer, the corresponding beam will be attenuated and phase shifted. As a result, interference between the "reference" beam (i.e. the beam which did not traverse the object) and the shifted beam, when these combine at the analyzer crystal, will lead to a shift and a dampening of the pattern with respect to that observed in the absence of the object, which can be recorded by a detector.

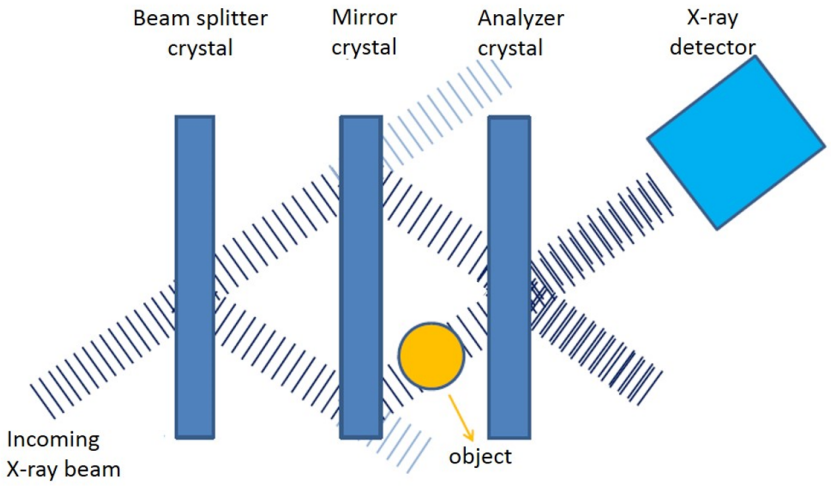

Figure 2.1: Schematic representation of a Bonse-Hart interferometer.

Quantitative phase contrast imaging was made possible by converting the recorded interference pattern into an image of the phase shift distribution by using a fringe scanning method [34]. This method entails the insertion of a wedge-shaped phase-shifting object into the reference beam, hence creating a controllable variation of the reference interference pattern of carrier fringes. The introduction of the

sample object shifts the observed fringes by an amount directly proportional to the RID, which could be quantified by means of a Fourier transform method, described in detail in [35].

Since the transmission of the analyzer crystal is dependent on the position of the standing wave impinging it, a direct link between measured intensity and phase shift can be made. While other XPCi methods are sensitive to the first or second derivative of the phase shift (as will be discussed shortly), Bonse-Hart interferometry is the only method sensitive directly to the phase shift, and is hence considered the most sensitive phase contrast method to date [36]. Practically, due to the restrictive requirement of sub-atomic alignment between the crystals, the interferometer is normally made by channel-cutting a single crystal block such that all crystals have a common base, and the analyzer and splitter crystals are at equidistant from the mirror crystal. This usually restricts the FOV to a few mm^2[34]. Furthermore, the crystals act as monochromators and lead to a substantial reduction in flux. As a result, practical use of Bonse-Hart interferometry is limited to high flux sources such as synchrotron radiation facilities.

2.2 Analyzer-based imaging

In Analyzer-based imaging, the rocking curve (RC) of an analyzer crystal is exploited to generate a phase contrast image [29, 37]. Typically, an incoming X-ray beam will be made monochromatic by passing it through a first monochromator crystal. A second, "analyzer" crystal is then placed downstream, directing the X-ray beam towards a detector (see Fig. 2.2). The analyzer crystal's RC is the result of a convolution between the reflectivity curves of the monochromator and

the analyzer crystals, plus the contribution of the beam divergence. For a given energy, the RC effectively determines the probability of X-rays being redirected towards the detector as a function of their incidence angle upon the analyzer. The analyzer can be positioned such that all incoming X-rays satisfy the condition of the Bragg angle, meaning that close to 100% will reach the detector. If an object is then placed in the beam's path, X-ray refraction will occur due to the object's complex refractive index, with the refraction angle determined from Eq. 2.3. As a result, the angle with which the X-rays hit the analyzer crystal will vary, and the portion of X-rays reaching the detector will change, in accordance with the RC. Hence, the crystal acts as an analyzer, in the sense that it performs an angular selection.

Increased sensitivity to refraction can be achieved by "rocking" the analyzer crystal to the steepest point on the RC, such that only 50% of the reference beam (i.e. without the object) reaches the detector [38]. In this configuration, small deviations in the X-ray direction caused by the object will lead to the maximum possible increase or decrease in detected intensity, depending on the angle of refraction. This increase/decrease in signal results in pairs of bright and dark fringes corresponding to edges of details in the object. This is a characteristic feature of XPCi methods which are sensitive to the refraction angle. These methods are often called "Differential Phase Imaging" techniques, since they are sensitive to the first derivative of the phase shift (see Eq. 2.3).

Phase retrieval methods have been proposed to separate the recorded intensity image into two images: one with the conventional, attenuation contrast, and one showing only the refraction signal. Chapman *et al.* developed a phase retrieval

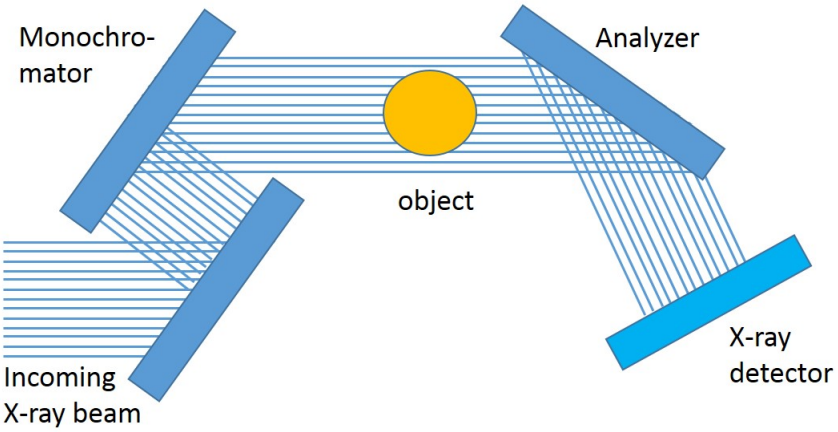

Figure 2.2: Schematic representation of a typical Analyzer-Based Imaging setup.

algorithm called "diffraction-enhanced imaging" which involves the acquisition of two images on opposite sides of the analyzer's RC [39]. The recorded intensity can then be expressed in terms of the reflectivity as a function of angle and the intensity affected by attenuation only. Using knowledge of the RC and both images, the attenuation intensity and refraction angle can be found on a pixel-by-pixel basis, resulting in separate attenuation and phase-contrast images. Four other phase retrieval methods for ABI are discussed and their validity is compared in [40].

Since the phase contrast in an ABI setup arises from sensitivity to refraction made possible by the analyzer crystal and its RC, it is therefore essential that the X-ray beam is monochromatic. While a conventional X-ray source can be made monochromatic (e.g. by the use of a mismatched, two-crystal monochromator [41, 42]), this would introduce a substantial reduction in flux. Furthermore, a highly precise alignment between the crystals is necessary in order to accurately detect the refraction signal, and hence a highly stable experimental setup is re-

quired. For these reasons, ABI is usually limited to synchrotron sources.

2.3 Grating interferometry

Grating interferometry is a phase contrast method which relies on the Talbot self-imaging effect and is hence also known as "Talbot Interferometry". According to the Talbot self-imaging effect, when a coherent X-ray beam is transmitted through a periodical object (grating), an image identical to the grating itself is formed at a set of distances away from the grating ("Talbot distances") [31, 43, 44, 45]. Figure 2.3 displays a typical setup of a GI system. A coherent X-ray beam traverses an object prior to encountering a phase grating. Being a phase grating, this is typically made of a low μ material as in principle it should introduce no attenuation. An absorption grating is then placed at a Talbot distance downstream, immediately in front of an X-ray detector. The presence of an object in the beam's path alters the Talbot self-image generated by the phase grating and leads to local displacements of the fringes. The absorption grating acts as an analyzer as it enables the conversion of phase effects into detectable intensity variations.

The phase effects can be separated from the object's attenuation by a method called "Phase Stepping" [46]. In this method, the phase grating is scanned laterally with respect to the absorption grating over one period, and an image is acquired at each grating position. The displacement in the intensity oscillation in each pixel over the scan, compared to the case where the object is absent, is related directly to the differential phase shift of the wavefront. Quantitative phase information can then be obtained by 1-dimensional integration. Phase-

Stepping simultaneously yields an attenuation image by considering the average intensity in each pixel over the one-period scan, in comparison to a reference scan performed while the object is absent.

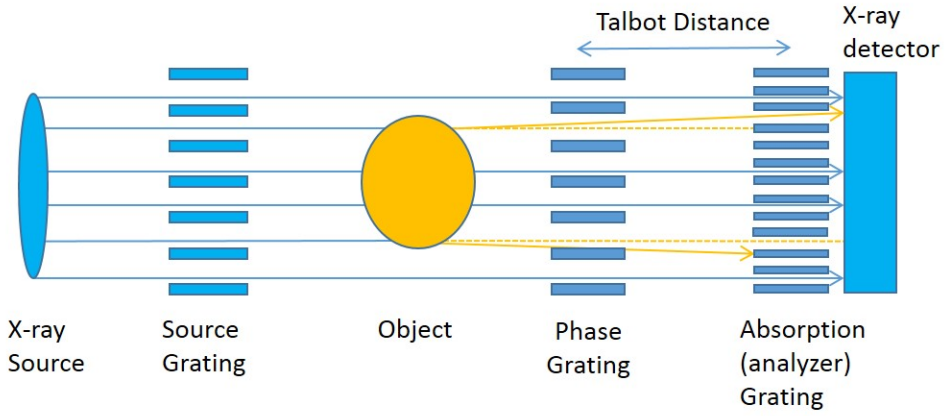

Figure 2.3: Schematic representation of a Grating Interferometry setup. The source grating is required only in the case of a laboratory implementation with an extended X-ray source.

While GI can be performed using some degree of polychromaticity [46], it relies on a spatially coherent beam. A laboratory implementation of the method (with an extended source) includes a third grating, placed shortly after the source. This corresponds to a Talbot-Lau configuration [32]. To achieve coherence, the source grating "divides" the beam into sets of individually coherent yet mutually incoherent sources [32]. The fine alignment between the gratings is essential for the method and so stability of about 100 nm is required [46], making it sensitive to environmental vibrations. Due to grating fabrication constraints, the FOV is normally limited to a few cm^2 [47]. Biomedical applications along with the issue of long scan times and relatively high dose, in particular when CT scans are

performed, are discussed in a review by Pfeiffer *et al.* [48].

2.4 Free-space propagation

Free-space propagation is an XPCi method which is sensitive to interference effects and has the simplest experimental setup of all XPCi methods. Just like in conventional attenuation radiography, the entire setup consists of an X-ray source and detector. However, two requirements transform it from an attenuation contrast method to one sensitive to phase effects; a spatially coherent source and a large object-to-detector distance [30]. As shown in Fig. 2.4, an object placed in the path of a coherent X-ray beam distorts the wavefront due to both refraction and attenuation. This leads to interference between the unperturbed parts of the beam (which did not encounter the object) and the ones perturbed by the object. when a detector is placed in contact with the object (as is done in conventional radiography), these interference effects are not visible. However, if the beam is allowed to propagate in free space (hence the name), sets of dark and bright fringes corresponding to the edges of object details are observed.

Although both wave- and ray-optics models can be used to provide a theoretical explanation of the phenomenon [27, 49, 50], a simplified ray-optics description can illustrate the creation of these fringes (see Fig. 2.4); one should notice that, at the edges of the object, the photons are redirected away from it. This means that photons which would have previously reached the detector's pixel are now impinging on the neighboring pixel, away from the object. This leads to decreased counts (dark fringe) immediately inside the object, and increased counts (bright fringe) immediately outside of it, as the refracted X-rays sum up with the

unperturbed ones traveling immediately outside the object.

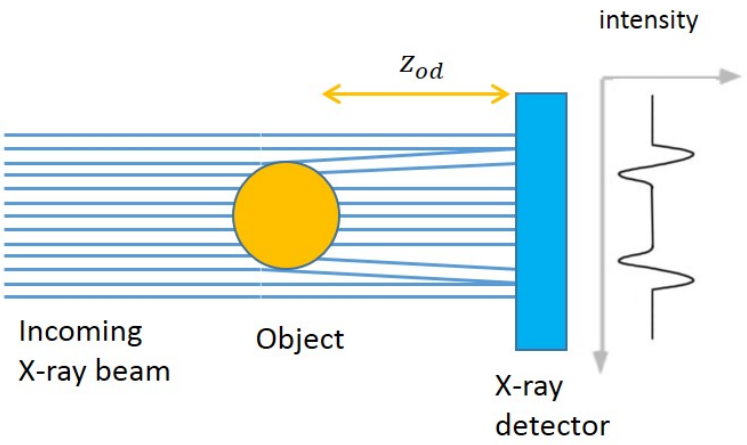

Figure 2.4: Schematic representation of a Free Space Propagation setup, demonstrating the ray-optics interpretation. The object-to-detector distance z_{od} is large compared to conventional radiography resulting in an intensity pattern sensitive to phase effects.

FSP is not limited to monochromatic sources and although synchrotron sources are ideal for its performance, laboratory implementations exist using microfocal X-ray sources [27]. However, as microfocal sources have reduced flux, scan times are long and may be impractical for many applications. This limitation can now be mitigated by the use of promising new technologies such as the liquid-metal-jet source which offers high coherence and flux [51, 52]. Another limitation of the method has to do with its spatial resolution. As no further optical elements are employed, the detector pixel size limits the spatial resolution and so high resolution detectors are required to resolve the interference fringes, which are typically characterised by very high spatial frequencies [30]. In practice, the FSP fringes diminish with an increasing pixel size, due to the convolution of the signal with

the detector's point-spread function [7].

In FSP, the contrast of a phase object is proportional to the second derivative of the phase function [27, 53]. This can be modeled by means of the "Transport-of-Intensity equation" (TIE), which describes the evolution of the intensity distribution of a monochromatic wave propagating in the z-direction, in the paraxial approximation [54]:

$$\nabla_{x,y} \cdot (I(x,y,z)\nabla_{x,y}\Phi(x,y,z)) = -k\frac{\partial}{\partial z}I(x,y,z). \tag{2.4}$$

Over the years, different phase retrieval methods were developed for FSP setups, however, the most commonly used ones are the ones developed by Cloetens [55] and Paganin [56]. Using the method presented by Cloetens, the phase map of an object can be quantitatively reconstructed by following a "holographic" reconstruction procedure which relies on the acquisition of multiple images at a set of object-to-detector distances [55]. On the other hand, the advantage of the method developed by Paganin is that it requires only a single image [56]. However, the use of a single image is made possible by making several assumptions, including object homogeneity. Since the experiment described in chapter 3 consisted of a FSP setup and a modification of Paganin's method for phase retrieval, a more detailed description of the latter is provided below.

Paganin's algorithm is derived starting from the TIE formulation (see Eq. 2.4). If a plane wave of uniform intensity I_0 transverses a homogeneous, thin object (such that it satisfies the projection approximation), Eqs. 1.1 and 2.2 for the beam's intensity and phase in the contact plane (i.e. immediately after the object) can

be used:

$$I(x, y, z = 0) = I_0 \exp\left(-\mu t(x, y)\right), \tag{2.5}$$

and

$$\Phi(x, y, z = 0) = -k\delta t(x, y), \tag{2.6}$$

where μ and δ are the object's linear attenuation coefficient and RID, respectively, and $t(x, y)$ is the projected thickness of the object onto the detection plane. By substituting Eqs. 2.5 and 2.6 into Eq. 2.4 and representing both the contact image and the phase contrast image as Fourier integrals, Eq. 2.4 can be rearranged and solved for $t(x, y)$:

$$t(x, y) = -\frac{1}{\mu} log\left(\mathcal{F}^{-1}\left\{\frac{1}{\left(\frac{z_{od}\delta}{\mu}\right)\kappa_\perp^2 + 1}\mathcal{F}\left[\frac{I(x, y, z = z_{od})}{I_0}\right]\right\}\right), \tag{2.7}$$

where $\mathcal{F}$ and $\mathcal{F}^{-1}$ are the forward and inverse Fourier transforms, and $\kappa_\perp^2 = (\kappa_x, \kappa_y)$ are the Fourier coordinates corresponding to x and y. Thus $t(x, y)$ can be obtained by considering a single projection ($I(x, y, z = z_{od})$) and a priori knowledge of δ and μ. If needed, $t(x, y)$ can then be substituted into Eqs. 2.5 and 2.6 to obtain separate attenuation and phase contrast projections.

Eq. 2.7 was derived assuming an infinite source-to-object distance, a condition which is approximately true at a synchrotron facility. However, the algorithm can be extended to include the magnification arising from a point source, if this is not negligible [56]. Although the algorithm is derived assuming a homogeneous object, it often provides good qualitative results also in cases when the object is not

strictly homogeneous, but can be approximated as quasi-homogeneous (i.e. has a constant δ/μ ratio throughout). This has been used in various cases when imaging biological samples [14, 57, 58]. Furthermore, as will be shown in chapter 3, a modification to Paganin's algorithm relaxes the assumption of a homogeneous (or quasi-homogeneous) object and yields good qualitative and quantitative results under certain conditions.

Paganin's algorithm is often used for FSP tomography, as all retrieved quantities (whether the projected thickness, phase or attenuation maps) satisfy line-integral relations, and so CT reconstruction can be performed by means of the FBP algorithm. However, there are many examples of different combinations of phase retrieval algorithms and CT reconstruction techniques for FSP, each making different assumptions on the object and the projection acquisition procedure. Various approaches can be found in publications such as [59, 60, 61, 62, 63, 64, 65, 66].

2.5 Edge illumination

2.5.1 Basic principles

The Edge Illumination method was first developed in the late 1990's using synchrotron radiation [9]. A simple schematic of the setup, demonstrating its underlying principles, is shown in Fig. 2.5(a). A narrow, collimated beam is aligned with the edge of a detector pixel row or column, such that only part of the beam reaches the pixels. When an object is placed in the beam's path, any refraction caused by the object will lead to a change in detected intensity, as it would de-

flect the beam towards or away from the pixel. In this example, upward refraction will lead to a decrease in measured intensity (see Fig. 2.5(b)), while refraction downwards will increase the detected intensity (see Fig. 2.5(c)). Practically, in a synchrotron, the incoming beam is collimated by a vertically narrow and horizontally long slit placed upstream of the object, while an absorbing edge is placed in contact with the detector row to create the edge illumination condition. Therefore, in this configuration, to obtain an image of the entire object, the latter must be scanned through the laminar beam.

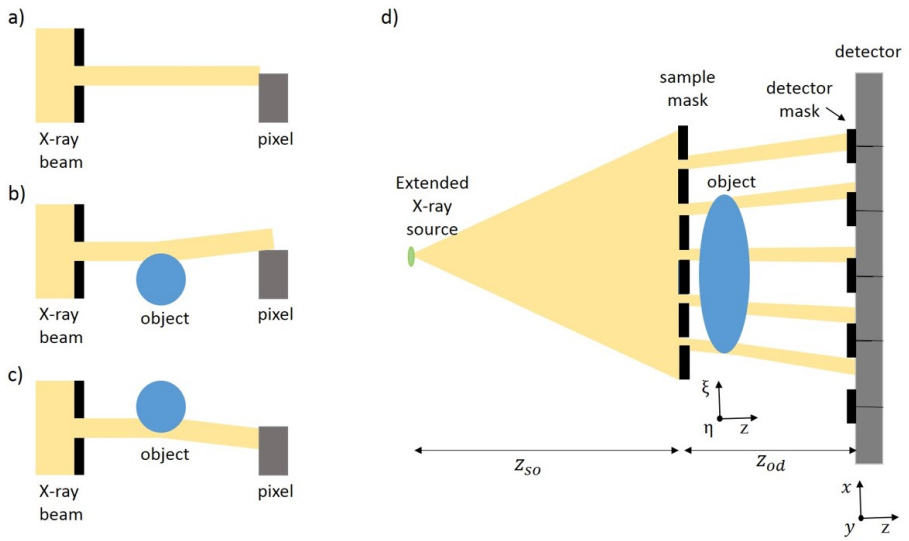

Figure 2.5: Schematic diagrams of the synchrotron (a-c) and laboratory (d) implementations of the edge illumination system. An X-ray beam aligned with the edge of a pixel (a) is refracted away (b) or towards (c) the pixel after passing through an object. In the laboratory, two masks are employed to replicate the edge illumination condition over the entire FOV (d).

Since the method does not rely on interference effects, nor does it require monochromatic radiation, it is well-suited for translation to a laboratory environment (using a polychromatic and extended source) [33]. To enable area imaging and avoid

scanning the object (which would lead to impractical scan times when using a laboratory source), the slit and edge are replaced with two masks which replicate the edge illumination condition for all detector rows (or columns), as is shown in Fig. 2.5(d). The first mask (sample-mask) is placed upstream of the object and divides the incoming beam into physically separated beamlets. The second mask (detector-mask) is placed in contact with the detector and creates insensitive regions between pixels. The detector-mask is fabricated with a period matching the detector pixel size, while the sample-mask period is scaled down to account for the beam's divergence. In this implementation, the entire object is captured in a single image with a spatial sampling rate given by the sample-mask period (de-magnified pixel size). However, unlike most other XPCi methods, in EI the intrinsic spatial resolution is not limited by the pixel size, and its upper limit is determined by the smaller of the sample-mask aperture and the projected source size, down scaled to the sample plane [17]. To achieve this higher resolution, a process called "dithering" can be used, where multiple projections are acquired at different sub-pixel positions of the object, and are later recombined to form a high-resolution projection image.

Although the laboratory setup of EI can seem similar to GI, the methods are inherently different. While GI is an interferometric approach, interference does not occur in EI as the masks' pitch is considerably larger, usually by an order of magnitude. Furthermore, the larger aspect ratio of the masks lowers their fabrication costs while also allowing a considerably larger FOV to be employed [67, 68]. Furthermore, the EI method is robust against environmental vibrations [69], achromatic [10], and can be used with sources with focal spots up to 100 μm [11]. Moreover, while the conventional EI setup is sensitive to refraction only

in the direction perpendicular to the masks' apertures, the system can be made sensitive to refraction in two directions if suitable masks are employed [70].

2.5.2 Experimental Methodology

The simple principles which the EI method relies on enable its implementation with different X-ray sources and detectors. Furthermore, the distances between the source and the sample, and between the sample and detector can be varied, as can the sample-mask aperture size, which to first approximation determines the spatial resolution. In the experiments described in chapters 4-5, the laboratory implementation of EI was used. Figure 2.6 depicts the experimental setup, demonstrating how the different elements are arranged on the optical table.

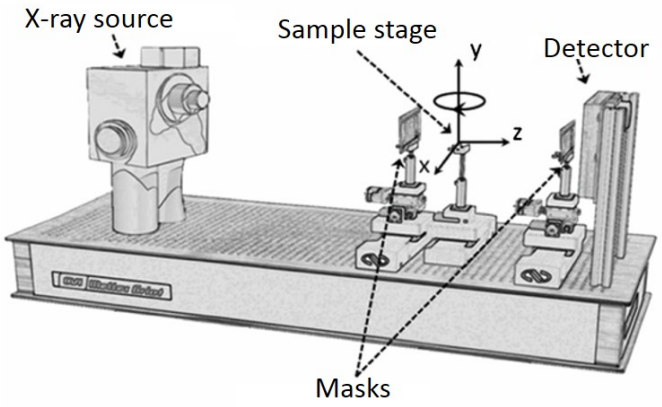

Figure 2.6: Pictorial representation of the lab-based EI setup, consisting of (from left to right) source, sample-mask, sample stage, detector-mask and detector. Adapted with permission from IOP Publishing: Physics in Medicine & Biology, Ref [2], Copyright 2014.

The X-ray source used in the experiments was a Rigaku MicroMax 007 HF rotating anode (molybdenum) X-ray tube (Rigaku Corporation, Japan) with a focal

spot of approximately 70 μm.

Throughout the experiments, two different detectors were used. The first was a Hamamatsu C9732DK flat panel detector with a passive-pixel CMOS sensor (Hamamatsu, Japan), and a pixel size of 50×50 μm^2. The second was a Pixirad single-photon counting, energy-resolving detector [71, 72], with a pixel size of 62×62 μm^2.

Both masks were fabricated by electroplating gold strips onto a graphite substrate (Creatv Microtech Inc., Potomac, MD, USA). For each detector, a different set of masks was required, such that their period matched that of the detector pixel (while taking beam divergence into account). However, in order to reduce the negative effect of pixel cross-talk on the EI signal, when the Hamamatsu detector was used, the masks period was doubled with respect to the pixel size. In this situation, every second detector pixel column is fully covered and is therefore discarded during data processing.

The sample of interest is placed on the sample stage, upstream from the sample-mask. During the imaging sequence, the sample is translated along the x-axis for dithering, and rotated around the y-axis for CT scans.

2.5.3 Phase retrieval approaches

Projection images acquired with an EI system contain mixed information related to both the object's attenuation and refraction properties. The first retrieval algorithms for EI, capable of separating the mixed projections into independent attenuation and refraction images, were developed by Munro [73] and Diemoz [74], and were inspired by Chapman's diffraction-enhanced imaging algorithm for

ABI [39]. These relied on the observation that when two images are acquired at different positions of the sample-mask (such that opposite edges are illuminated), the signal due to attenuation remains the same, while the refraction signal reverses. For quantitative retrieval, the algorithm requires a measurement of the Illumination Curve (IC), which describes the detected intensity as a function of the sample-mask displacement in the absence of an object. The form of the IC and the equations used in the algorithm are slightly different depending on the chosen EI setup (i.e synchrotron or laboratory implementation) [73, 75]. Here, the key retrieval equations relevant to the laboratory implementation are presented.

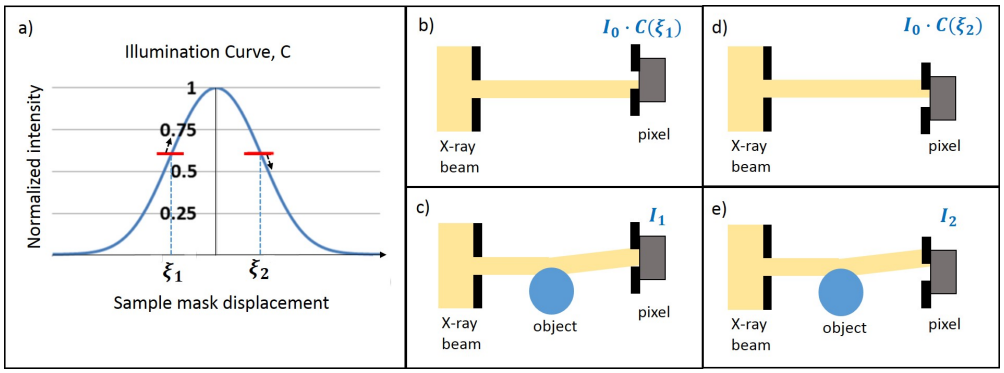

Figure 2.7: The object's refraction can be related to a shift on the IC. The IC is a measure of the detected intensity as a function of the sample-mask position, with no object present (a). In this example, for sample-mask position ξ_1, the presence of the object will increase the detected intensity (b-c), while the effect is reversed when the mask is positioned at ξ_2 (d-e). The red marks on the IC in (a) correspond to ξ_1 and ξ_2, while the black arrows represent the effect of the object's refraction on the intensity.

Since the beam's divergence is not negligible, a frame of reference is adopted in which the magnification, M, between the object (ξ, η, z) and detector (x, y, z) planes is taken into account. Hence, $x = M\xi$ and $y = M\eta$, where the magnifica-

tion depends on the source-to-object distance z_{so} and object-to-detector distance z_{od} according to $M = (z_{so} + z_{od})/z_{so}$ (see Fig. 2.5(d)). Fig. 2.7(a) shows a typical IC, here indicated by C, obtained by scanning the sample-mask laterally over one period, in the absence of the object. Two positions of the sample-mask ($\xi = \xi_1, \xi_2$) are chosen as the working points for the two images acquired with the object in the beam (I_1 and I_2), where it is assumed that ξ_1 and ξ_2 are symmetric around the origin, and that they correspond to the parts of the IC which are approximately linear [75]. Consider the cases shown in Fig. 2.7(b-e). It is apparent that, in a similar way to the effect of object refraction on the RC in ABI, in EI, the beam's refraction caused by an object is equivalent to a displacement on the IC. Using the algorithm, the two images can be processed together to retrieve the projected attenuation and the refraction angle, according to:

$$\int \hat{\mu}(\xi, z)dz = 2\int \hat{k}\hat{\beta}(\xi, z)dz = -\ln\left(\frac{(I_1 + I_2)/I_0}{C(\xi_1) + C(\xi_2)}\right), \tag{2.8}$$

$$\alpha = \frac{\partial}{\partial \xi}\int \hat{\delta}(\xi, z)dz = f^{-1}\left(\frac{I_1 - I_2}{I_1 + I_2}\right) \cdot \frac{M}{z_{od}}, \tag{2.9}$$

where I_0 is the maximum intensity measured by the detector when the masks apertures are aligned, and f^{-1} indicates the inverse of a function f which maps the displacement caused by the object refraction onto the difference between the corresponding values on the IC [75]. The quantities indicated by a hat in Eqs. 2.8-2.9 refer to an effective energy (e.g. $\hat{k} = k(E_{eff})$ etc.). It was shown that the effective energies for the phase and attenuation are in general different, and depend on both the imaging system and object parameters [76].

The algorithm described above has been derived under the assumption that an object placed in the beam's path affects it by means of attenuation and refraction only. However, according to recent algorithms developed by Endrizzi *et al.*, if three images are acquired and processed together, a third contrast channel can be retrieved [3, 77, 78]. This additional channel is a scatter image, the intensity of which depends on the object's microscopic structure on a sub-pixel scale, which has the effect of broadening the beamlet. By defining $\hat{\sigma}_{\Phi}^{2}(\xi, \eta, z)dz$ as the localized broadening of the beamlet by an infinitesimal volume of the object of width dz, the retrieved scattering signal representing the total broadening of the beamlet is equal to [79, 80, 81]:

$$\hat{\sigma}_{f}^{2} = \int \hat{\sigma}_{\Phi}^{2}(\xi, \eta, z)dz \ . \tag{2.10}$$

These approaches therefore provide quantitative, complementary information, which is essential for some applications. However, they typically require displacing the sample-mask multiple times, therefore making scans slower, especially in CT. To tackle cases where a single, high quality image with high contrast is needed and speed is more important than multi-modality, a retrieval algorithm requiring only a single image was developed for the case of homogeneous (or quasi-homogeneous) objects [82]. In fact, the three-image and single-image retrieval algorithms formed the basis for the work presented in chapters 4-5, respectively, in which these were extended for use in EI lab-based CT scans under different conditions. A more detailed description of these algorithms will be provided in the relevant chapters.

2.5.4 Extension to CT

The EI technique was first adapted to perform CT scans in 2014 by Hagen *et al.* [18]. In contrast to the conventional method, so far CT scans in EI have been realized by rotation of the object while the source and detector are kept stationary, in line with most micro-tomography applications [83]. The mathematical formulation for CT reconstruction from projection data was provided in the previous chapter (see 1.3) using the frame of reference shown in Fig. 1.3. Equivalent expressions are obtained when considering an object described by a frame of reference $(x'y'z')$ which is rotated by an angle θ with respect to the stationary source and detector (xyz). Sinograms can then be constructed from the retrieved projection data:

$$S_\delta(x, y; \theta) = \frac{\partial}{\partial x} \int_{l(x,y;\theta)} \delta(x', y', z') dz, \tag{2.11}$$

$$S_\beta(x, y; \theta) = 2k \int_{l(x,y;\theta)} \beta(x', y', z') dz. \tag{2.12}$$

Using Eqs. 2.11 and 2.12, tomographic maps of δ and β can be obtained with standard CT reconstruction algorithms such as FBP. However, the derivative appearing in Eq. 2.11 implies that a special filter function $\mathcal{H}$, the Hilbert filter, must be used in the FBP formula [84]:

$$\mathcal{H}(k) = -i \cdot sign(k), \tag{2.13}$$

where here k is the Fourier domain frequency term, in accordance with Eq. 1.8. Therefore, by employing the Hilbert filter in the FBP formula, δ can be recov-

ered using a 1-step algorithm, as the filter effectively performs the integration of the differential projection in the frequency domain [84]. Alternatively, a simple 1-dimensional integration can be applied to the sinogram S_δ, prior to FBP reconstruction with the Ram-Lak filter.

It should be noted however that the integration step, whether performed prior to or during the CT reconstruction, can lead to image artefacts. In an integrated sinogram these can appear as unidirectional stripes, as local errors are smeared along the direction of integration. In RID tomograms reconstructed with the Hilbert filter, these can appear as gradually changing shades (i.e "gradient" artefacts). These artefacts however can be reduced by the use of the retrieval algorithms developed in chapters 4-5.

Furthermore, when EI CT is performed using an extended source with an associated magnification, the latter should be taken into account when quantitative reconstruction is sought (i.e. sinograms measured at the detector plane should be demagnified onto the object plane). In order to use the FBP formula for parallel beam geometries, this entails assuming constant magnification across the object. This assumption is often made when employing the conventional, lab-based EI configuration, as the resulting error on the magnification is negligible. For example, when considering an object with a 4 cm diameter, and the typical distances employed (z_{so}=1.6 m, z_{od}=0.4 m), this assumption implies a maximum error of 2.5% on the magnification, and its effect on the CT-retrieved quantities is further reduced by the averaging occurring during the backprojection step.

Unlike refraction images which are proportional to the first derivative of the phase function and hence have an "edge-enhanced" appearance, the integration

step means that maps of the RID (from now on referred to as "phase maps") have the conventional appearance in which an area contrast is displayed. Although both attenuation and phase maps have similar appearance and can aid in the quantitative identification of different materials, the phase maps are often advantageous as they inherently present a higher contrast.

The optimization of EI CT for different imaging environments and applications has been the focus of extensive research since the method was first adapted to CT. It was shown that quantitative CT reconstruction of δ and β maps is possible by employing the two-image retrieval algorithm described in 2.5.3, using both SR [18] and laboratory sources (within the limits of polychromaticity) [85]. It was demonstrated that "mixed" tomograms (i.e. ones formed as a linear combination of the phase and attenuation signals) can be reconstructed using one image per view, if the axis-of-rotation is parallel to the direction of phase sensitivity [18]. Furthermore, the low dose capabilities of lab-based EI CT were discussed in another experiment which demonstrated that the phase signal strength is independent of the sampling rate [85]. This observation was further confirmed in an additional publication in which the relationship between the sampling rate and the retrieved phase values was investigated. The study demonstrated that while a high sampling rate is required for the retrieval of unambiguous values of the phase shift in a planar image, a much reduced sampling rate can be used to retrieve quantitative tomograms of the RID [86].

With the aim of reducing CT scan times, three additional phase retrieval algorithms were developed. The first is based on the two-image algorithm presented previously 2.5.3, however, it exploits the "reverse projection" relation, according

to which, for a fixed position of the sample-mask, projections separated by 180 degrees can be processed together (as they are effectively equivalent to projections acquired at opposite slopes of the IC for a given view). Therefore, the sample-mask can be kept at a fixed position throughout the scan, and the object can rotate continuously over 360 degrees [87]. In the second algorithm, the retrieval of both δ and β is combined with the CT reconstruction step by using a gradient-based optimization method [88]. Using this method, only a single image per view is required. Initial results demonstrated that it is possible to retrieve δ and β from a data set acquired over 180 degrees, however, this requires altering the position of the sample-mask between successive views. Nevertheless, if projections are acquired over 360 degrees, the object can be rotated continuously. The third algorithm was developed by Diemoz *et al.* and can be viewed as an adaptation of Paganin's algorithm to the case of EI [82, 89]. By making the assumption of a homogeneous object with known refractive index values, the object's 3-dimensional phase map can be retrieved using a single image per view. Here, the object can be rotated continuously and an angular range of 180 degrees is sufficient, leading to unprecedented exposure times in XPCi CT with laboratory sources [89].

Recently, a new possible application of EI CT was identified in the field of tissue engineering [14]. In this study, acellular scaffolds were scanned using different XPCi methods, with the aim of evaluating their decellularization techniques through the visualization of the scaffolds' microstructure. A key finding was the observation that, at least for some samples, images obtained with the lab-based EI system were of comparable quality to the "gold-standard" ones obtained with a FSP setup and SR [14].

Ultimately, the advances in EI research have enabled it to be used for a vast range of applications, thus maximizing its potential for widespread use. Different factors that can be varied include source technology, spatial resolution, the retrieval of various contrast channels and a choice between projection and CT imaging. The work presented in the following chapters was primarily focused on the advancement of lab-based EI CT for biomedical applications, and was undertaken in parallel with some of the CT-studies mentioned above. In particular, two retrieval methods were developed in this thesis work: one suitable for multi-modal retrieval in long, high-resolution CT scans, and a second approach targeting fast CT scans, in which only a single image per view is acquired. The latter was developed as an extension to Diemoz's algorithm and overcomes its main limitation, i.e. the assumption of a homogeneous object. In addition, the range of applications which could benefit from EI CT was expanded by performing a first proof-of-principle experiment in a new area with SR, as will be discussed in the following chapter.

3

Post-mortem imaging using XPCi: a proof-of-principle study

3.1 Background and motivation

Perinatal autopsy is important for future pregnancy management, medical research and mortality statistics [90]. However, perinatal autopsy rates continue to fall, for a variety of reasons, including parental reluctance on moral or religious grounds, fear of cosmetic effects and a lack of understanding of the potential benefits [91]. This has led to the development of less-invasive post-mortem imaging techniques, such as Magnetic Resonance Imaging (MRI), being developed both as adjuncts and alternatives for conventional autopsy [92, 93]. It has been shown that in the majority of cases, images acquired using a 9.4 T MRI scanner provided a high enough level of detail to rule out the necessity of an autopsy. However, these scanners are not licensed for clinical use and require extremely long acquisition times, which prevents them from being used in routine clinical practice for

the purpose of post-mortem imaging. Clinical MRI scanners, usually featuring a 1.5 T field, do not provide adequate image quality of small fetuses, primarily due to insufficient spatial resolution [92, 93]. Conventional X-ray CT is faster, easier to use and more widely available; however, it suffers from poor soft-tissue differentiation, especially in foetuses and children, in the absence of exogenous contrast media [94].

XPCi methods on the the other hand have the potential to overcome some of these problems, as they are capable of differentiating between different soft-tissues without the use of contrast media, while maintaining high spatial resolution. Although XPCi techniques are currently limited to synchrotron facilities and specialized laboratories, the optimization of these methods such that they could be used in a clinical setting is the primary research interest of many groups.

The aim of the study presented in this chapter was to provide a first proof-of-principle of the feasibility of using XPCi for post-mortem imaging. To do so, an experiment was carried out which involved two simplifications. First, the simplest XPCi method, FSP, was used under ideal conditions, i.e. at a synchrotron facility. Second, rather than human tissue, a newborn piglet was used as an animal model owing to its anatomical similarity to a human foetus in shape, size and general anatomy.

3.2 Materials and methods

3.2.1 Sample preparation

A deceased new-born piglet, acquired from a local farm near the imaging site which supplies the food industry, was used as a test sample. Ethical approval was not required, and no animals were sacrificed for the purpose of this experiment, since the animal died naturally at birth. For ease of prolonged handling, and since it has been reported to have no effect on the resulting image contrast [95], the piglet was fixed using a 4% formalin solution. It was then placed in a custom-made plexiglass cylinder (10 cm diameter, 25 cm height) which maintained it in a fixed (vertical, head up) position during the CT scan.

3.2.2 Experimental setup

The experiment was conducted at the ID17 biomedical beamline of the European Synchrotron Radiation Facility (ESRF, Grenoble, France) with a FSP arrangement. The working principles of FSP were described previously (see 2.4), and a schematic of the setup is shown in Fig. 3.1. The source size was approximately 132 μm (horizontal)$\times$24 μm (vertical) (full width at half maximum) and was located approximately 143 m from the end of the optics hutch where the sample was placed. A double-crystal Si (111) monochromator provided X-rays with an energy of 52 keV. The beam's vertical dimension was approximately 5 mm. The sample was placed downstream of the monochromator, on translation and rotation stages. The object-to-detector distance (z_{od}) was approximately 10 m. Images were acquired using a FReLoN CCD camera, custom-developed in-house

at the ESRF, with an effective pixel size of 46×46 μm^2. The recorded FOV was 2048×110 pixels, corresponding to approximately 5 mm vertically, and thus required vertical scanning of the sample to cover its full length (approximately 25 cm). This was achieved by acquiring a 5 mm thick, full CT data set ("sub-scan") of the sample at a given vertical position, then shifting the sample vertically by slightly less than 5 mm (to create an "overlap" and avoid missing information) and repeating the procedure until the full volume was covered. As the sample was also larger than the horizontal FOV, projections were acquired using the half-acquisition method, i.e. the sample was rotated over 360 degrees while its centre was aligned with the edge of the FOV [96]. This is equivalent to acquiring projections of both halves of the sample, each over 180 degrees. Each CT scan consisted of 8000 equally spaced projections, each of which was acquired with a 15 ms exposure time. Furthermore, for each scan a total of 40 images without a sample (i.e. "flat fields") were taken: 20 images immediately before the scan and 20 images immediately after. These were averaged and used to correct the FSP projections for beam and detector non-uniformities.

3.2.3 Image processing

Each of the raw FSP projections was normalized by division by the flat-field image, and composite projections of the full sample were created to account for the use of the half-acquisition method. This was done by adding pairs of projections separated by 180 degrees, at their overlap position (i.e. centre-of-rotation (COR)), after horizontally inverting the second projection of the pair. It should be noted that although attempts were made during the experiment to align the

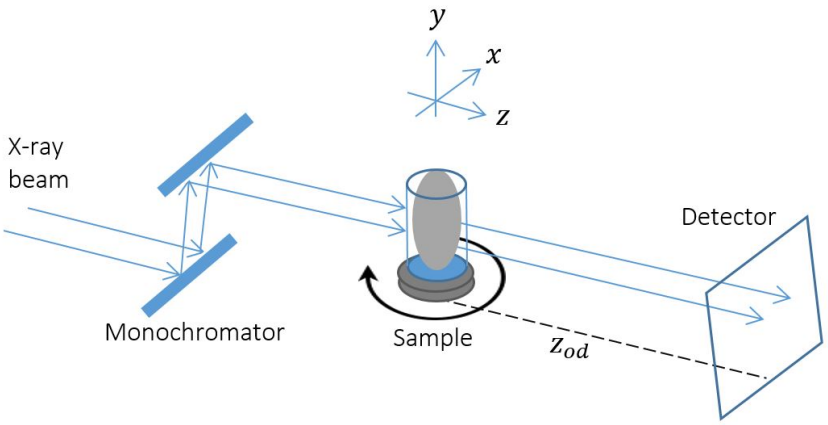

Figure 3.1: Schematic representation of the FSP setup at the ESRF. The X-ray beam is wide in the horizontal (x) direction and narrow in the vertical (y) direction. The large object-to-detector distance (z_{od}), jointly with the beam coherence, gives rise to the phase signal. The sample was rotated around the y-axis.

axis-of-rotation with the vertical axis, it is apparent that these were slightly misaligned, as the COR position varied between subsequent scans, and even within a sub-scan (consisting of about 100 pixel rows). As can be seen in Fig. 3.2, misalignments which were not corrected led to artefacts in the reconstructed CT slices. This manifested in the form of a bright/dark dot at the COR for misalignments of 1-2 pixels, with additional streaks if the misalignment was more substantial. To avoid these, the overlap position was adjusted manually for each sub-scan until the artefacts were minimized.

In order to extract the phase information, a phase-retrieval algorithm was applied to each projection. As previously discussed in 2.4, a common FSP phase retrieval method was developed by Paganin [56]. Using Paganin's algorithm, the projected thickness of a homogeneous sample with known δ and β values can be

Figure 3.2: Reconstructed CT slices from unprocessed projections showing how image artefacts increase if the overlap position is not chosen accurately during the half-tomography correction. Resulting streaks due to shifting the overlap position by 0.5 (b) and 2.5 (c) pixels with respect to (a).

retrieved from a single image. However, if the sample contains additional materials with significantly different refractive index values, Paganin's algorithm will reconstruct these wrongly; primarily affecting their interfaces with other materials, either by over-blurring or by leaving the characteristic FSP double-fringes under-compensated.

Typical refractive index values of different tissue types can be seen in table 3.1. It is apparent that while most soft tissue organs have small differences in their values, the refractive index values of bone are significantly different. Therefore, when attempted to use Paganin's retrieval algorithm with input values of either bone or soft tissue, the resulting CT slices suffered from the above mentioned artefacts. To overcome this, a phase retrieval algorithm introduced by Beltran [97] was implemented in the reconstruction. Beltran's algorithm is based on the TIE and can be viewed as an extension of Paganin's algorithm. Beltran's method enables the retrieval of 3-dimensional maps of the complex refractive index of a multi-material object [97, 98]. For quantitative retrieval, the algorithm requires a priori knowledge of the complex refractive index of each material in the sample,

Table 3.1: Refraction and attenuation values of different tissue types at 52 keV [4].

Tissue/Organ	$\boldsymbol{\delta}$	$\boldsymbol{\beta}$
Blood	0.895E-7	4.486E-11
Bone (cortical)	1.518E-7	1.428E-10
Brain	0.882E-7	4.398E-11
Fat	0.788E-7	3.605E-11
Lung	0.887E-7	4.431E-11
Muscle (skeletal)	0.887E-7	4.418E-11
Skin	0.917E-7	4.535E-11

along with the total projected thickness of the object. The algorithm is derived by considering a ternary object composed of material j embedded in material 1, with the latter slowly varying in thickness along the transverse direction. The projected thickness of material j can then be calculated according to:

$$t_j(x,y) = -\frac{1}{\Delta\mu}\log\left(\mathcal{F}^{-1}\left\{\frac{1}{z_{od}\gamma\kappa_\perp^2+1}\mathcal{F}\left[\frac{I(x,y,z=z_{od})}{I_0 exp\left[-\mu_1 A(x,y)\right]}\right]\right\}\right), \tag{3.1}$$

where $\Delta\mu = \mu_j - \mu_1$, $\gamma = \frac{\delta_j-\delta_1}{\mu_j-\mu_1}$, and μ_1, δ_1, μ_j, δ_j are the attenuation and refraction terms of materials 1 and j, respectively. The total projected thickness is given by $A(x,y) = t_1(x,y) + t_j(x,y)$. The meaning of the other terms is the same as that given in 2.4, where Paganin's algorithm was first discussed.

In practice, $A(x,y)$ was obtained in the following way: Eq. 2.7 was used to reconstruct for each angular view the projected thickness of the "encasing material", $t_1(x,y)$ (in this case - soft tissue), i.e. making the assumption that the entire sample is homogeneous. For each of these projections, $A(x,y)$ was calculated for each detector pixel row, by locating the edges of the cylinder containing the sample, calculating its radius and using these values in an equation calculating

the projection of a circle. Eq. 3.1 was then used to calculate $t_j(x, y)$, using δ and μ values of soft tissue (encasing material; 1) and bone (embedded material; j), and the total projected thickness $A(x, y)$, calculated as just described.

CT slices of t_j can then be reconstructed by using the FBP formula with the Ram-Lak filter. However, in practice, prior to the phase retrieval and CT reconstruction steps, projections from consecutive sub-scans were vertically joined. This was done at their overlap position, and included the averaging of the overlapping areas, to account for minor differences in background intensity. The reason for joining the projections prior to the retrieval step, was that as the retrieval algorithm operates in 2-dimensions, it fails to perform adequately at the top and bottom of a projection. This lead to about 20 detector rows (10 at the top, 10 at the bottom) with non-physical retrieved values, resulting in non-physical reconstructed CT slices. Hence, by joining projections from sub-scans, these artefacts are confined to the top and bottom 10 rows of the full dataset, and the entire volume of the sample can be reconstructed.

Following CT reconstruction, the Amira platform (Mercury Computer Systems, Germany) was used for 3-dimensional volume visualization and manipulation. Volume rendering was performed to assist with organ identification, and slice orientation was varied to allow for best organ visualization, similar to the procedure followed in standard clinical practice.

3.2.4 Image analysis

The entire data set was assessed by an experienced paediatric radiologist (Owen J Arthurs, with 8 years' experience in clinical imaging), to identify internal organs

and other structures, assess tissue contrast and optimize 3-dimensional organ visualization, analogous to a clinical setting. Seven organ or body systems were assessed, including the heart, lungs, kidneys, liver, small and large bowels (intestines), brain and spinal cord, and bones (vertebrae), as these are typically the most important organs to assess in human post-mortem imaging.

Unfortunately, as we had no access to a standard CT scanner, the phase images have not been directly compared with conventional CT scans of the same sample. However, to provide quantitative evidence to support the findings of the radiologist, it is possible to exploit the fact that, in an unprocessed FSP slice (i.e. where phase retrieval was not applied), the area contrast (i.e. away from edges of a detail which will exhibit the typical phase-induced fringes) is caused merely by sample attenuation. Therefore, the contrast-to-noise ratio (CNR) was assessed and compared in multiple organs for both unprocessed FSP slices and phase-retrieved slices. The CNR was defined as the difference in mean values of two closely spaced tissues (each calculated from a homogeneous area away from edges), divided by the standard deviation of the background noise (measured in the air gaps in the cylinder). More generally, it should also be noted that the superiority of phase-contrast images over attenuation contrast images - mainly in terms of signal-to-noise ratio and CNR - has been previously reported in samples of similar size and complexity [99].

3.3 Results

Table 3.2 provides a quantitative comparison by reporting the measured CNR values for different organs for both unprocessed and phase-retrieved FSP slices.

Table 3.2: Contrast-to-noise ratio (CNR) values for different organs in unprocessed and phase-retrieved FSP slices.

Tissues compared	Unprocessed FSP CNR	Phase-retrieved FSP CNR
Small intestine - free peritoneal fluid	1.0	4.6
Kidney - intestine	1.6	7.1
Heart - artery	1.1	5.5
Kidney - liver	1.6	5.9
Muscle - stomach	1.2	9.5

In all cases, CNR values were higher in phase-retrieved slices, with an increase factor ranging from 3.7 to 7.9. This can be visually appreciated in Fig. 3.3, which presents both an unprocessed FSP (Fig. 3.3(a)) and phase-retrieved slice (Fig. 3.3(b)), each windowed to optimize the visualization of the same region in the heart. The heart's structure was clearly visible in the phase-retrieved slice, owing to the increased soft-tissue contrast arising from sensitivity to phase shifts induced by the sample.

All seven organ or body systems were visualized with sufficient contrast and adequate resolution, using the described FSP setup. Fig. 3.4 displays images of key organs for the purpose of a post-mortem examination. The anatomy of the heart is depicted with a high level of detail (Fig. 3.4(a,b)); all four cardiac chambers with the great vessels were identified, including high-quality visualization of the cardiac valves (such as the pulmonary valve, Fig. 3.4(b)). Although attempts were made to minimize the effect of variation in background intensity between sub-scans which were joined, a remnant of these intensity differences can be seen in the form of the striations in Fig. 3.4(a). Lung structure is also shown

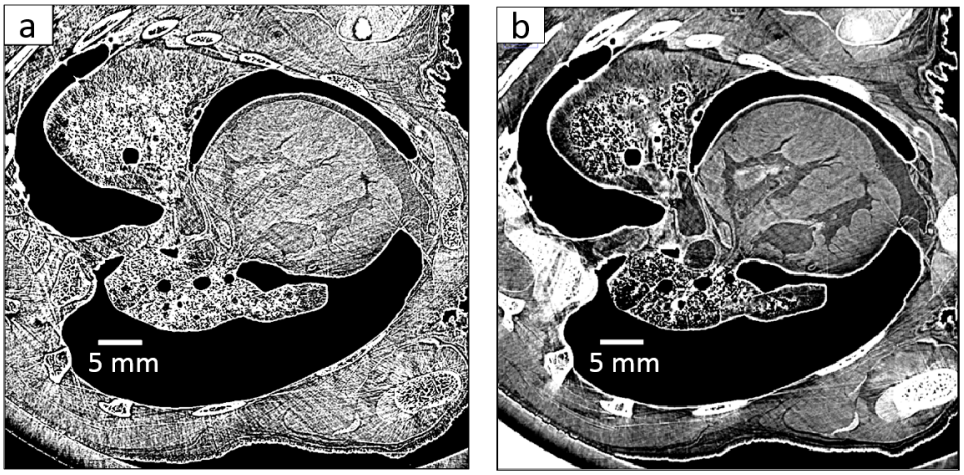

Figure 3.3: Phase retrieval (b) provides higher soft-tissue contrast compared with an unprocessed FSP (a) image of the same axial slice through the thorax, showing normal heart and lungs. Large bilateral post-mortem pneumothoraces are demonstrated (non-pathological).

clearly (Fig. 3.4(c,d)); the architecture shown in Fig. 3.4(d) was visualized by magnifying and reconstructing the minimum intensity projection over 24 slices. The anatomy of the right kidney is shown in two orthogonal views (Fig. 3.4(e,f)) and in a false-colour maximum intensity projection image obtained by using 31 slices (Fig. 3.4(g)). The renal pelvis emerging into the proximal ureter is clearly shown in Fig. 3.4(e), and the vascular system is depicted in detail in Fig. 3.4(g); no intravascular contrast agent was required.

A coronal slice of the head is shown in Fig. 3.5(a); the contrast was optimized for soft-tissue, causing the nasal canals and skull to appear over-exposed, while the observed striations are again related to the normalization process between sub-scans. The high soft-tissue contrast in the eyes and olfactory bulb can be easily appreciated. Figure 3.5(b) shows a magnified slice of the brain (maximum intensity projection using 28 slices), in which white and grey matter in the cerebellum

can be clearly differentiated, despite very similar δ values and the comparably strong signal from the adjacent skull.

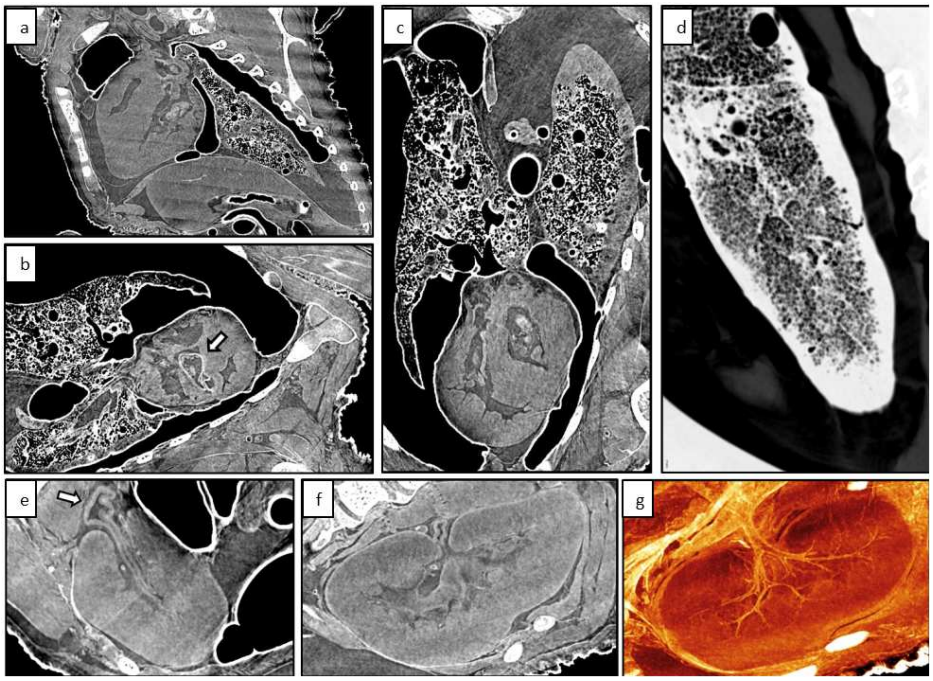

Figure 3.4: Excellent soft-tissue contrast allows for a high level of detail of the organs typically identified and examined at autopsy. Internal cardiac structures are clearly demonstrated, including ventricular chambers in sagittal (a) and oblique axial orientations ((b), FOV: ∼4×7 cm for both) and the outflow tract valves [e.g. pulmonary valve; arrow in (b)]. Lung windowing permits detailed examination of the lung parenchyma (coronal; (c), FOV: ∼5×3 cm) which may be further enhanced using magnified minimum intensity projection images for structural detail ((d), FOV: ∼1.5×2.5 cm). Axial and coronal images of the kidney ((e) and (f), respectively (FOV ∼2×3 cm for both)) allow the normal collecting system and ureter (e; arrow) to be identified, and the internal vascular anatomy can be assessed on false-coloured reconstructed maximum intensity projection images ((g): FOV ∼2×3 cm).

Figure 3.6 demonstrates the high dynamic range of this imaging technique. In this figure, good soft-tissue contrast is evident when visualizing the small intestine (Fig. 3.6(a)), liver (Fig. 3.6(b)) and eye, down to the cranial nerves (Fig.

3.6(c)). However, although the protocol was designed to optimize visualization of soft-tissue, this does not compromise the quality of bone imaging, as effective windowing allows the visualization of both soft- and hard-tissue details. Indeed, Fig. 3.6(d) demonstrates the high resolution and contrast of a vertebral body obtained with the FSP setup. Therefore, XPCi allows all different components of of a complex biological sample to be adequately resolved through the acquisition of a single data set.

Figure 3.5: Brain imaging. A coronal slice through the brain, showing normal globes and olfactory structures ((a), FOV ∼10×15 cm). A sagittal maximum intensity projection image of the cerebellum showing white/grey matter differentiation ((b), FOV ∼1.8×2.2 cm).

3.4 Discussion and conclusion

This study confirmed that XPCi holds great promise as a tool for whole body post-mortem imaging. The results demonstrate that XPCi can simultaneously provide high quality images of both bone and soft tissue for this clinical application. With further optimization for use with commercially available X-ray sources, XPCi CT has the potential to become a clinically useful post-mortem

imaging modality.

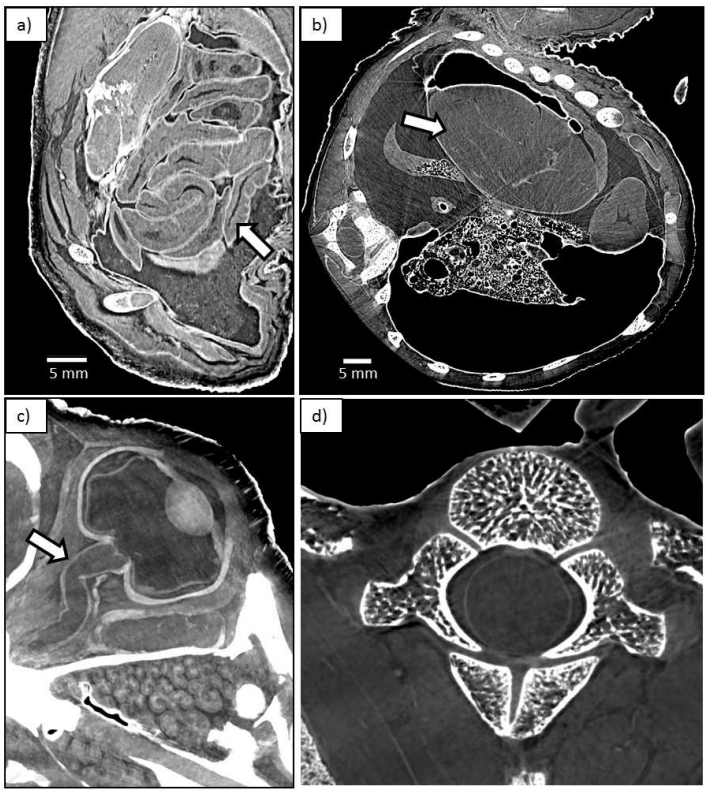

Figure 3.6: High soft-tissue contrast allows detailed examination of several anatomical structures. Examples include oblique axial slices of the abdomen demonstrating normal intestinal wall and lumen (a; arrow) and hepatic architecture (b; arrow). Magnified oblique sagittal views through the orbits and globe allow the optic nerve to be assessed ((c), FOV ∼6×4 cm; arrow). Using different windowing provides high bone detail, such as seen in this axial slice through a single vertebral body ((d), FOV ∼4×4 cm).

In this proof-of-principle study, a FSP setup was used with SR. While FSP does not require the use of any optical elements and is therefore easy to implement, it requires highly coherent radiation, which limits its use outside specialized facilities. Nevertheless, as mentioned previously, several XPCi methods can now be implemented with laboratory sources [27, 32, 33, 100]. Indeed, it is the possibility of translating these results to a laboratory setting by using either EI or another

lab-based XPCi method which supports the relevance of the work presented here. In particular, it has been recently shown that for certain samples, images obtained with the lab-based EI setup were of similar quality to those obtained with a FSP setup at a synchrotron [14].

The results shown in table 3.2 provide some form of comparison between XPCi and conventional attenuation-based imaging; however, these are drawn from the same data set, which was optimized for phase imaging. In the future, a direct comparison with conventional CT could be made. Where no access to a standard CT scanner exists, a comparison can be made with an additional data set obtained with a short propagation distance, such that it approximates to a conventional CT setup.

The sample used in this experiment was fixed using formalin solution. This procedure is currently common for XPCi CT [99, 101, 102, 103, 104, 105] since it simplifies specimen-handling, and has been reported to have no effect on the resulting image contrast [95]. Although formalin fixation is routinely used in diagnostic histopathology practice, in the future, when an optimized laboratory-based XPCi system will become available, it should be possible to image both fixed and non-fixed samples. This advancement however is dependent on the possibility of performing fast CT scans in the laboratory, which is indeed the aim of many recent studies. With regards to the EI method, such work includes the single-image retrieval algorithm developed by Diemoz *et al.* [82] and its extension to a multi-material object, which will be introduced in chapter 5. Generally speaking, lab-based EI XPCi CT seems to possess ideal characteristics for

the imaging of small fetuses (<24 weeks' gestation), which is an application for which conventional methods currently struggle to produce images with sufficient diagnostic quality [94]; other lab-based implementations of XPCI could present similar advantages. Furthermore, although not shown here, it should be noted that software like Amira allows segmenting specific organs and measuring their size (width, length, volume etc.), which can further assist in the identification of anatomical abnormalities.

As a final note, it should be pointed out that although a newborn piglet was used in this study, the results are likely to be generalizable to other animal models and human foetal tissue. This animal model was specifically chosen owing its similarity to a human foetus in terms of size and body components. All of the shown structures would be of potential significance during a conventional human perinatal autopsy. A variety of techniques are currently required for human post-mortem imaging in order to cover a range of body sizes, with different technical attributes for soft-tissue and bone imaging. Were XPCi to be available and optimized for human use, particularly for smaller foetuses, then XPCi CT would have the potential to become a clinically useful post-mortem imaging modality, alongside other existing techniques including conventional CT and MRI.

In conclusion, the results of this study demonstrate that XPCi CT is applicable to relatively large, unstained biological samples, and that major organs can be visualized with the required contrast and resolution for the purpose of clinical diagnostic use. This experiment was conducted as a first proof-of-principle study using SR and an animal model, and successfully demonstrated the feasibil-

ity of using XPCi methods for such applications. Future studies should focus on translating this application to a clinical environment, such that XPCi CT could become a practical alternative to perinatal autopsy. The work presented in the following chapters was aimed at advancing the current lab-based EI CT system such that it could be used in a robust way, for a range of applications, perinatal autopsy being one of them. With further successful developments of EI CT, it could be possible to perform post-mortem imaging of human foetuses in a laboratory, thus providing a method with the potential for accessible, inexpensive imaging with high throughput.

4

Robust multi-modal retrieval strategies for EI CT

The most commonly used phase retrieval algorithm in EI is the one which was described in chapter 2 (section 2.5.3), which requires two images per view (acquired at two different positions of the sample-mask, such that opposite edges of the pixel are illuminated) [73, 74]. By using this algorithm, separate images of the refraction and attenuation properties of the object can be obtained.

So far, quantitative and high-contrast images of a range of samples were obtained by using the 2-image algorithm, on datasets acquired both at synchrotrons and laboratories, in planar and CT modes [14, 18, 74]. Nevertheless, this was not the case for all samples, and indeed for some (specifically a subset of thick, low-contrast samples, see Fig. 4.1), CT reconstructions of lab-based scans were of poor quality, often suffering from excessive noise and severe artefacts.

The work presented in this chapter aimed to provide a better understanding of the origin of these artefacts, and to develop new strategies for removing (or reducing)

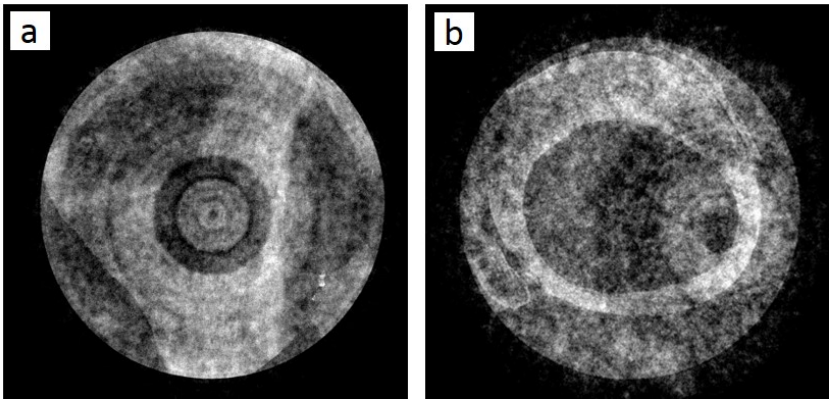

Figure 4.1: Examples of lab-based EI CT reconstructions suffering from high noise levels and ring artefacts. Retrieved phase slices of (a) a human kidney sample, and (b) a human atherosclerotic plaque specimen. Both samples were placed in a plastic cylinder (diameter=7 mm) for imaging.

them such that quantitative CT scans can be performed in the laboratory on a wider range of samples.

In the first part, the results of a simulation study aimed to characterize different sources of noise and artefacts in experimental CT scans are presented. Four different sources of error were considered and modelled, and their effect on CT reconstructions was investigated via simulated data.

In the second part, a new retrieval algorithm specifically aimed at multi-modal, high-resolution lab-based CT scans is developed, to overcome the main sources of error affecting EI CT. The algorithm is first validated using simulated data, and its ability to remove severe image artefacts is demonstrated by applying it to an experimental dataset of a complex biological sample.

4.1 Characterizing and modelling artefcats

4.1.1 Background and motivation

When trying to identify sources of error in EI CT imaging, it is important to consider all the different steps which occur during and after the scan. For example, a typical EI CT imaging sequence is as follows: first, an IC scan is performed, where multiple images are acquired in the absence of a sample, as the sample-mask is translated over one period. The CT scan then begins: for each view, flat-field images are acquired (i.e. without a sample in the FOV), at the sample-mask positions chosen for imaging. The sample is then moved into the FOV, and images are acquired again at the chosen positions of the sample-mask. When dithering is performed, for each position of the sample-mask, multiple images are acquired as the sample is translated by sub-pixel steps ("dithering steps images"). The sample is then rotated, and the same process is repeated for the next view.

To process the data, images containing the sample are first normalized by the flat-field images, to correct for beam and detector non-uniformities. Then, a high-resolution ("dithered") image is obtained by combining the images corresponding to the different dithering positions of the sample. To obtain separate attenuation and refraction images, the phase retrieval algorithm is then applied to the dithered images (which were acquired at different positions of the sample-mask). From the retrieved images, separate sinograms of the sample's attenuation and refraction are created, and are used as input for CT reconstruction using FBP (with the Ram-Lak and Hilbert filters, respectively).

Therefore, any error related to the movement of the sample (translation, rotation) or sample-mask (translation) during the scan, or errors arising from beam

instability, detector defects and masks misalignment or defects, could propagate in a non-intuitive way during the post-processing steps and affect the appearance of CT reconstructed images.

Wave-optics simulation

In order to identify the main sources of error which lead to common artefacts in EI CT, a simulation study was performed. The simulation is described in detail in a publication by Vittoria [106], in which it is shown that by using the wave-theory of optics in the Fresnel approximation, a Fourier formulation of EI imaging can be derived. The simulation algorithm has been implemented in Matlab (Mathworks, USA) and is computationally efficient. Vittoria's algorithm enables varying different parameters of the EI setup to retrieve the 1-dimensional signal which would be detected by a detector row for a given sample.

This is done by realizing that the EI system can be described as a series of free-space propagations and transmissions through objects (here, objects refer to both the sample and the masks). The evolution of the beam's intensity as it propagates in free-space between the source and the sample-mask (assumed to be at the same plane as the sample), and between the two masks, can be described by the Fresnel-Kirchhoff integral in the Fresnel approximation. For a thin object (sample or masks) satisfying the projection approximation, the effect of its presence on the beam can be taken into account by the complex transfer function, $T_{obj}(x) = \exp[-i\Phi(x) - M(x)]$, where $\Phi(x) = k\int \delta(x,z)dz$ and $M(x) = \int \mu(x,z)dz$. The simulation therefore predicts the beam's intensity evolution as it is radiated from a source, propagates a certain distance until it is transmitted through the sample-mask and sample, then propagated in free-

space again until it is transmitted through the detector-mask, and sampled by the detector pixel. The simulation enables the variation of all components: i.e., the spatial distribution of the source can be chosen, along with a given spectrum if a polychromatic beam is considered. The masks' material and thickness can be varied, as can their aperture size and period. The sample's composition and geometry can be modified to examine different cases, and the distances between the source and the masks can be varied. If necessary, the detector's point-spread function can be included by convolving the signal with a Gaussian curve of a given width, while the detector energy response can be incorporated by modifying the employed X-ray spectrum. When simulating a polychromatic beam, the detected signal is evaluated for each energy in the spectrum, and the polychromatic signal is calculated as a weighted sum. Furthermore, sample dithering can be simulated by evaluating the detected signal at different positions of the sample, the latter determined by the number of dithering steps and the masks' period.

To adapt the simulation code to a CT scan, the above algorithm was looped over a specified angular range, with the sample rotated for each angular view. The rotation of the sample (numerical phantom) was implemented by calculating the projected thickness of the sample as a function of the rotation angle, prior to computing the sample's complex transmission function, $T_{obj}(x)$.

4.1.2 Methods and results

For this initial study, the simplest phantom was chosen - a homogeneous rod. This choice was motivated by the realization that an ideal reconstructed CT slice would display a uniform, flat disk, and any other features could be regarded as

image artefacts. For comparison with experimental data, the phantom and EI parameters were chosen to match those used in the laboratory. The phantom was modelled as a polymethyl methacrylate (PMMA) rod with a 5 mm diameter, and its refractive index values were taken from the ICRU 44 database [4]. The source-to-object and object-to-detector distances were set as $z_{so} = 1.6\ m$ and $z_{od} = 0.4\ m$, and a total of 80 detector pixels of size 100 μm were simulated. The sample-mask period and aperture size were 79 μm and 10 μm, respectively. The detector-mask period was 100 μm with an aperture size of 17 μm.

First, an IC scan was simulated (as is necessary for the phase retrieval step), for 30 positions of the sample-mask over one period. Then, for the simulated CT data, the sample was rotated over 180 degrees, with a 0.5 degree step. At each view, images were acquired at two positions of the sample-mask, $x_e = \pm 8 \mu m$ with respect to the position at which they are fully aligned with the detector-mask apertures (i.e. maximum of the IC). Images acquired at these positions will be referred to as I_L and I_R indicating these were acquired on the "left" and "right" slopes of the IC. To avoid under-sampling, at each position of the sample-mask, the sample was dithered using 16 dithering steps, which were then recombined to create high-resolution projections. From these, two sinograms (S_L, S_R) were created, corresponding to the signal detected at the two sample-mask positions. It should be noted that the output of the simulation is an ideal, noise-free signal. Therefore, to test the effect of different sources of error, these were added to S_L and S_R directly, prior to the phase retrieval and CT reconstruction steps.

In this study, 4 different possible sources of error were considered, all of which could be present during experimental CT scans and affect the final reconstruction. The following provides a description of the way these can arise, how they

were modelled and implemented via simulation, and their observed effect on reconstructed CT slices.

1. **Masks/detector imperfections -** This refers to the case when the detected intensity in specific pixels in the detector row is considerably and consistently higher/lower than the intensity measured by other pixels (in the absence of the sample). This situation can occur due to major defects in the masks (e.g. if the size of an aperture is significantly reduced) or if the detector pixel itself is faulty. This was modelled as a pixel-specific systematic error, present for the same pixel at all views, and in all dithering steps images. However, the value of the added error could be different between the images acquired at the two different sample-mask positions (e.g. a reduced aperture size can have a different effect on the measured intensity, depending on its alignment with the detector-mask aperture).

   To study the effect of such an error, different "error vectors" were created (with dimensions equal to that of the simulated detector row), and were added to the simulated signal of each dithering step image. From these, dithered images were created, which were then used to form corresponding sinograms. The 2-image phase retrieval algorithm was applied to the sinograms, and CT reconstruction followed. This procedure was repeated multiple times, for different error vectors, corresponding to different positions of the defective pixels, and different error values.

   The addition of such a systematic error had the effect of creating thick rings in the reconstructed phase slice. This is similar to conventional, attenuation-based CT, where ring artefacts are common, and originate from defective pixels. However, unlike in attenuation-based CT, the rings in the

EI phase slice are thick and smeared. This is due to two reasons: the fact that dithering is used, hence rings are as wide as the number of dithering steps used (instead of having a 1 pixel width), and the fact that the differential phase sinogram is integrated during the CT reconstruction step with the Hilbert filter (causing the smearing of the rings).

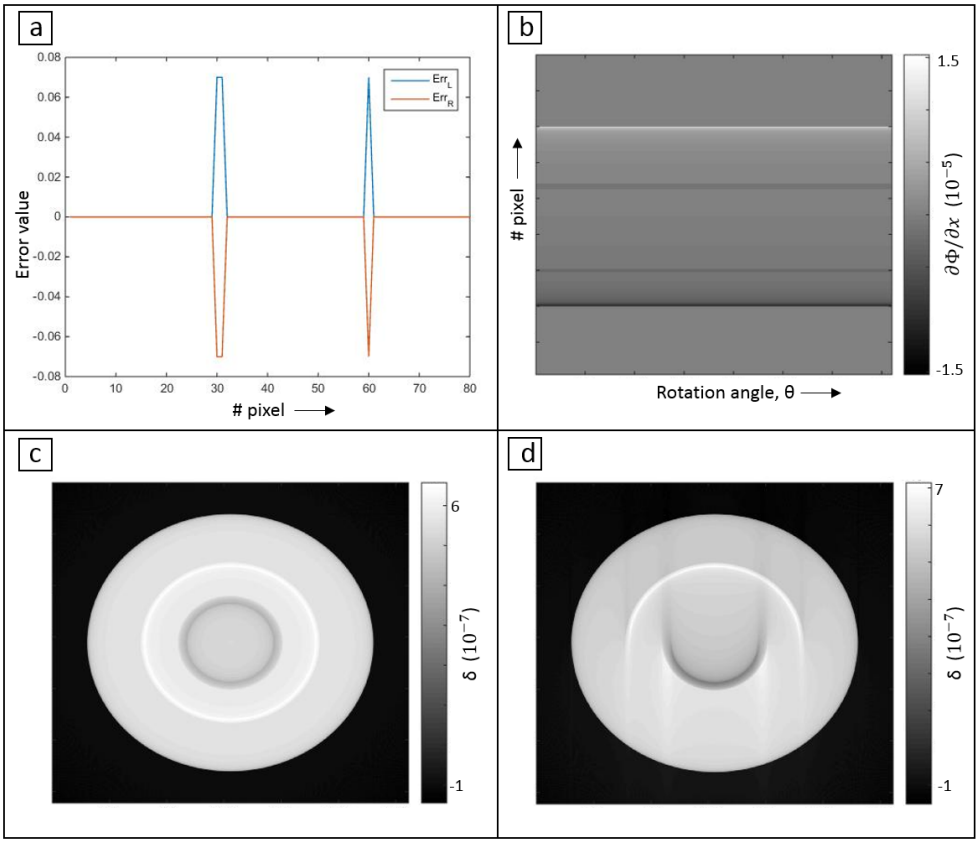

Figure 4.2: The effect of 3 defective pixels on a CT slice. (a) The error vectors which were added to the left (blue) and right (orange) images. (b) The added error appears as horizontal lines in the retrieved differential phase sinogram. Reconstructed phase CT slices from a 360 (c) and 180 (d) degrees sample rotation showing full and partial ring artefacts, respectively.

Furthermore, the rings' intensity and position changed according to the chosen error values (and their difference between the right and left images),

and their position on the detector row. Similar to the case of conventional CT, a 180 degrees rotation results in partial rings, while full rings are observed if the sample is rotated over 360 degrees.

An example for the effect of this systematic error can be seen in Fig. 4.2, where the used error vectors are shown in panel (a), the retrieved differential phase sinogram is shown in panel (b), and panels (c) and (d) show the reconstructed CT slices, for rotations of 360 and 180 degrees, respectively.

In addition, by keeping the error value constant while varying the defective pixel position on the detector, it was found that the ring's intensity is inversely proportional to the ring's radius (i.e. pixel distance from COR). This is demonstrated in Fig. 4.3 which shows the ring intensity as a function of its radius.

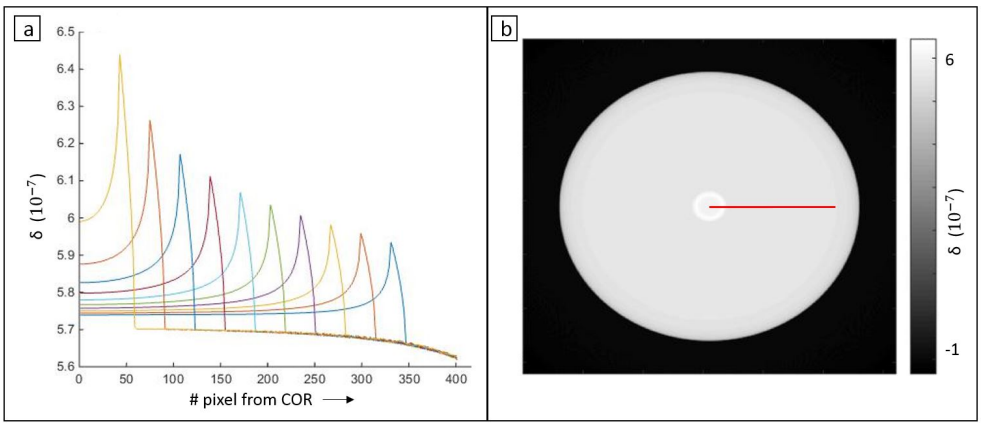

Figure 4.3: The ring intensity is inversely proportional to its radius, as demonstrated by plotting profiles (corresponding to the red line in (b)) across multiple CT slices, each reconstructed after adding the same error value to a single detector pixel, at different positions on the detector row. The CT slice in (b) is showing the case of the defective pixel closest to the COR, corresponding to the plot with the highest peak in (a).

2. **Flat-field normalization error -** Here, the assumption is that errors or noise can be introduced when sample images are normalized by flat-field images. As previously mentioned, for each angular view, the imaging sequence entails first acquiring two flat-field images, one at the left position of the sample-mask (F_L) and another at the right position (F_R). The sample is then moved into the FOV, and the sample-mask is returned to the left position, where images are acquired for each dithering step of the sample ($I_{L,ds}$). The sample-mask is then moved to the right position, where the complementary images are acquired ($I_{R,ds}$). For the normalization, sample images from each dithering step are divided by the flat-field images, i.e. $I_{LN,ds} = I_{L,ds}/F_L$ and $I_{RN,ds} = I_{R,ds}/F_R$, and are then recombined to create highly-sampled images.

   Therefore, any discrepancy between the flat-field and sample images can introduce correlated errors, since the same flat-field image is used for all dithering steps images in a single view. Discrepancies between the flat-field and sample images can be either due to random noise, or due to slight differences in the alignment of the masks caused by the movement of the sample-mask between their acquisition.

   To model this type of error, error vectors were added to the ideal signals (prior to the phase retrieval and CT reconstruction steps), where the value added to each pixel was drawn randomly from a uniform distribution with mean 0. The same error vector was used for all dithering steps images of a given sample-mask position and view.

   An example of the effect of such an error on EI data is shown in fig. 4.4. The employed error vectors for a particular view are plotted in panel (a), where

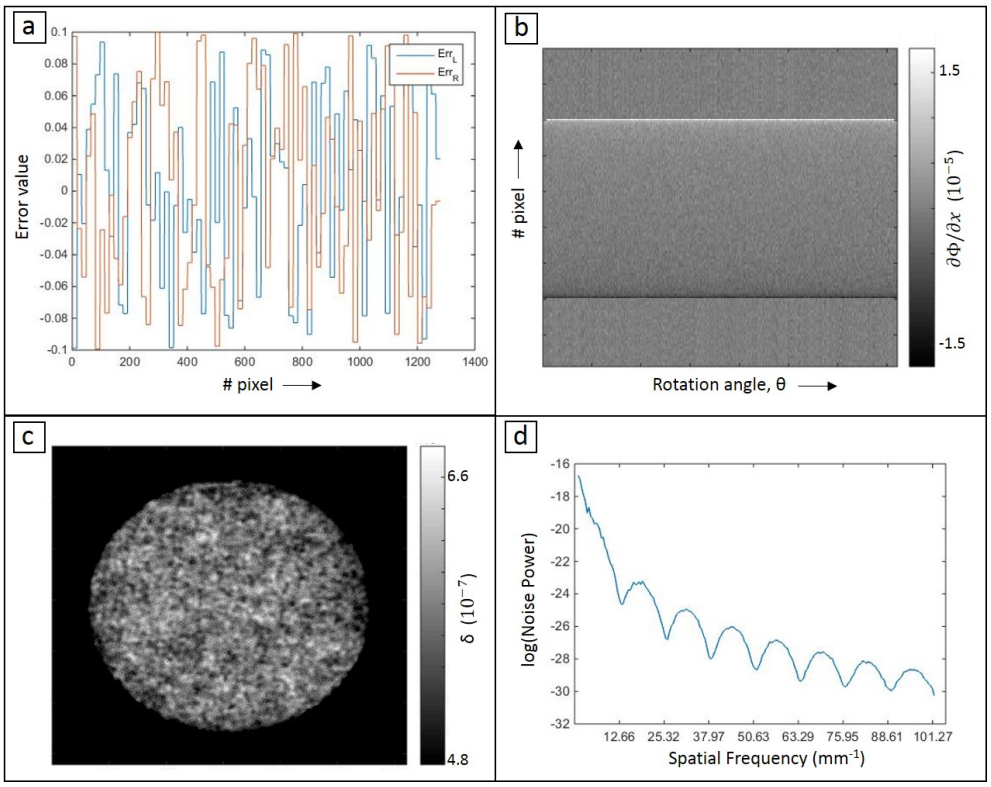

Figure 4.4: The effect of an error in the flat-field normalization on CT slices. (a) The error vectors which were added to the left (blue) and right (orange) dithered images of the first angular view. (b) The retrieved differential phase sinogram. (c) Reconstructed phase slice, windowed to optimize the visualization of the resulting clumpy noise structure. (d) The NPS of the noise present in the object, shown using a logarithmic scale.

the reader can notice that although the values were randomly drawn from a uniform distribution for each dithering step image, when these images are recombined to form the dithered image, the resulting error vectors have a "stepped" appearance (since the error values are constant for all dithering steps of the same pixel). The resulting differential phase sinogram is shown in panel (b), which displays what seems at first as random noise. However, the CT reconstruction shown in panel (c) reveals that the noise is correlated, leading to a "clumpy" noise texture. To provide complementary informa-

tion, a plot of the noise-power-spectrum (NPS) of the noise present in the imaged object, is shown in panel (d) using a logarithmic scale. The NPS has become a common tool for the characterization of the noise behaviour of CT systems, by presenting the distribution of noise power over different spatial frequencies [107, 108, 109]. It therefore provides information about the texture of the noise in addition to its magnitude; white noise has constant magnitude over all frequencies, while increased noise power concentration at low or high spatial frequencies implies coarse ("clumpy") or finer graininess of the noise pattern, respectively [110]. The NPS was calculated by selecting a region within the (homogenous) object in the reconstructed CT slice, subtracting its mean, taking its 2-dimensional FT and calculating the latter's square modulus at each spatial frequency, which were then radially averaged.

As expected from the appearance of the CT slice, which featured a clumpy noise structure, the NPS associated with this type of error presents a higher noise power concentration at low spatial frequencies, and its shape resembles that of a FT of a rectangular function, consistent with the "stepped" appearance of the noise in dithered images. In this case, the width of the rectangular function is given by the sample-mask period, i.e. 79 μm, which is in agreement with the locations of the NPS minima, at integers of the corresponding spatial frequency $1/79\ \mu m^{-1} = 12.66\ mm^{-1}$.

3. **Intensity changes between dithering steps -** This type of error considers the situation where the beam intensity varies randomly between acquired projections between angles, but also between dithering steps at the same

angle. To minimize this effect, in practice, before the pixel-by-pixel normalization of the sample image by the flat-field image, an intensity correction factor is calculated by comparing the average intensity in a background region in the sample image, to the same region in the flat-field image. The entire sample image is then divided by the correction factor, and only then does the pixel-by-pixel normalization step occurs. However, this process has the potential to introduce errors, which would be characterized by the same magnitude for all pixels in a given dithering step image.

To model this, different error vectors were created for each dithering step image, each sample-mask position and each view. However, for each unique image, the same error value, randomly drawn from a uniform distribution of mean 0, was added to all pixels in the image.

Fig. 4.5(a) shows an example of error vectors added to the ideal, dithered (left and right) images. These error vectors are shown for 5 detector pixels (=80 image pixels after dithering recombination) to emphasize that although the values are drawn randomly for each dithering step image, their pattern repeats with the number of dithering steps (=16). In this particular example the error values are relatively small (maximum 2% of the signal strength), resulting in a differential phase sinogram (panel (b)) which seems to be artefact free. However, when the contrast in the reconstructed phase slice is stretched (panel (c)), it is apparent that this type of error creates a fine noise pattern which repeats itself on a small scale.

This can be better appreciated by considering the corresponding NPS (panel (d)), which presents low noise power at all frequencies, apart from the ones corresponding to multiples of the sample-mask period (i.e. the distance

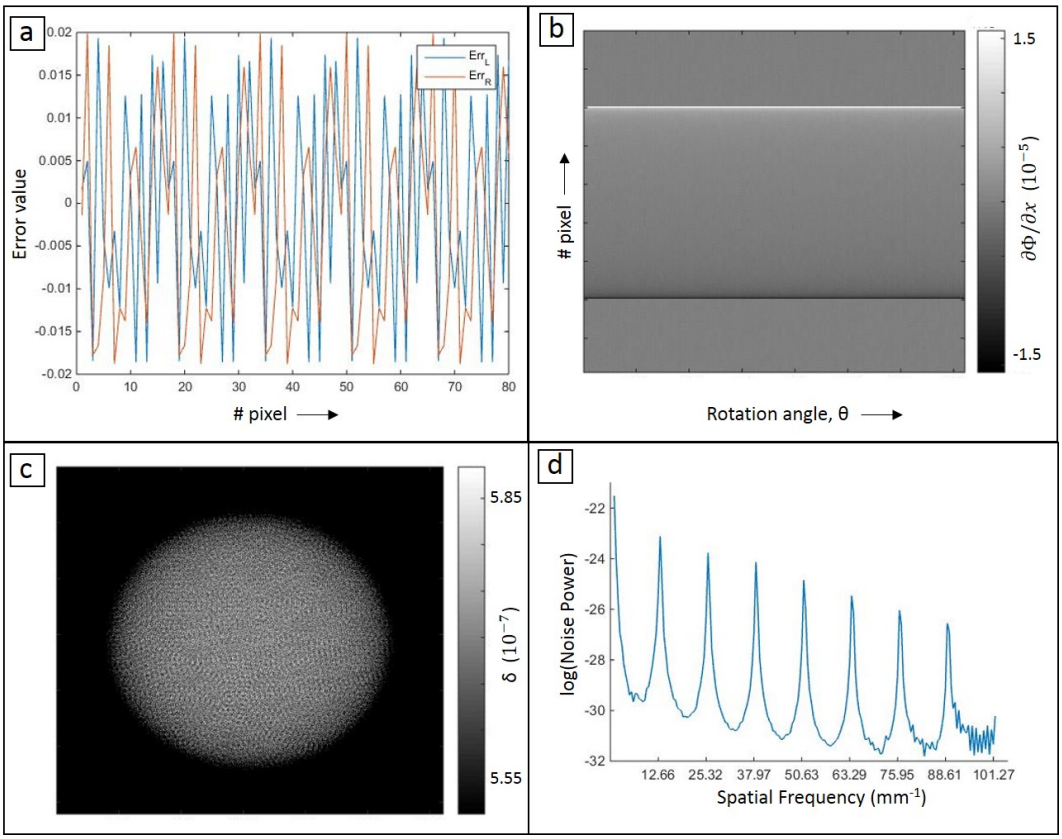

Figure 4.5: The effect of errors arising from intensity variations between acquired projections. (a) Error vectors added to (5 detector pixels of) the left (blue) and right (orange) dithered images of a single view. (b) The retrieved differential phase sinogram. (c) The reconstructed phase slice, containing a fine noise structure revealed by appropriate windowing. (d) The NPS of the noise present in the object, shown using a logarithmic scale.

separating adjacent detector pixels, after dithering recombination). This indicates an underlying periodicity in the noise structure, which manifests as the fine structure seen in the phase slice.

4. **Spatially correlated shot noise -** In this part, the aim was to study the effect of statistical noise, associated with the production of X-rays, which can potentially have a certain spatial correlation between neighbouring detector pixels, due to either detector cross-talk, or slow variations in the

masks. To model this, unique error vectors were created and added to each dithering step image, before the creation of dithered images. To create each error vector, error values (for each detector pixel) were first randomly drawn from a normal distribution (to simulate shot noise), and the entire sequence was then convolved with a Gaussian kernel. Depending on the chosen value for the standard deviation of the Gaussian kernel, the noise structure in the reconstructed phase slice changed. In general, as the standard deviation was increased, the noise in the phase slice changed from random, almost white-noise, to one containing both a fine, periodic structure on small length-scales, and a larger, "clumpy" noise structure on larger length-scales.

As an example, consider the case shown in Fig. 4.6. Panel (a) presents the error vectors generated for a particular view and dithering step, for the left (blue) and right (orange) images, using a 1-dimensional Gaussian kernel with a 0.7 pixels standard deviation. While a certain degree of spatial correlation can be observed in these error vectors, this is more difficult to detect in the error vectors created when the dithering steps images are recombined (see panel (b)). The resulting phase slice is shown in panel (c), in which noise patterns on both small and larger length-scales can be observed. On the other hand, when the standard deviation of the Gaussian kernel is reduced to 0.2 pixels, the noise in the resulting phase slice does not seem to present any spatial correlation (panel (d)). This can be better appreciated by considering the NPS plots corresponding to both slices (blue and orange lines corresponding to reconstructions in panels (c,d), respectively), shown in panel (e). The orange curve is simply the result of adding random noise

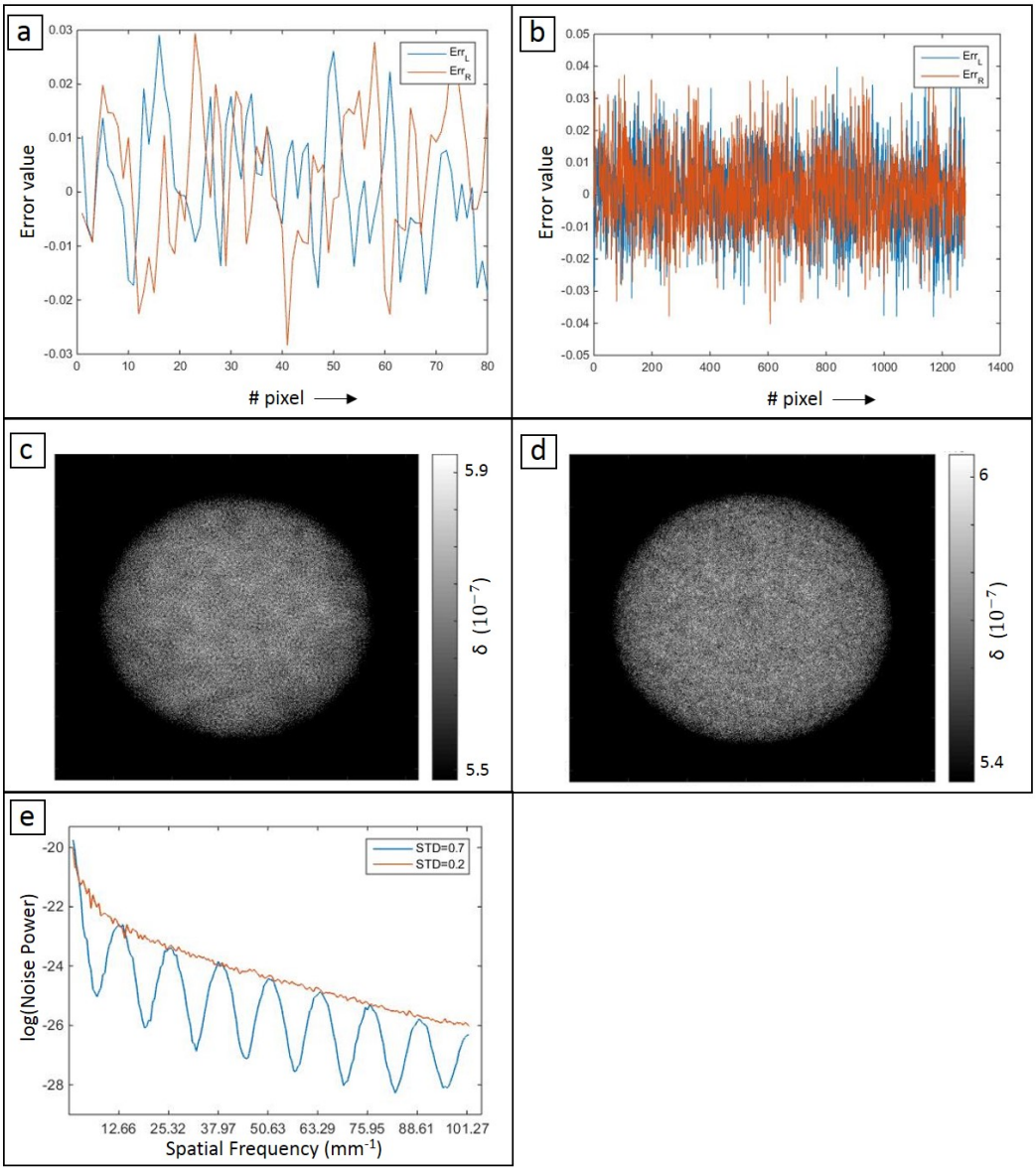

Figure 4.6: Noise patterns arising from correlated shot noise. (a) Error vectors generated for the left (blue) and right (orange) dithering step images of a particular view, and the error vectors obtained for the corresponding dithered images (b). Phase slices (c,d) and corresponding NPS plots on a logarithmic scale (e). A Gaussian kernel with standard deviation of 0.7 pixels was used to generate (a-c), while (d) was generated using a Gaussian kernel with a 0.2 pixels standard deviation.

to the signal. The blue curve, on the other hand, shows interesting features: similarly to the previously considered noise (arising from intensity changes between dithering steps), the NPS plot here is periodic, and features peaks at frequencies determined by the sample-mask period, which gives rise to the fine noise pattern seen in the slice in panel (c). However, here the peaks are not narrow, and instead their width indicates that there is a spatial correlation between different pixels, giving rise to the "clumpy" noise structure observed in panel (c).

For comparison with experimental data, a CT scan of a PMMA rod (5 mm diameter) was performed in the laboratory using the EI set up. As a source, the Rigaku MicroMax 007 HF rotating anode (molybdenum) X-ray tube (Rigaku Corporation, Japan) with a focal spot of approximately 70 μm was used, and was operated at 25 mA and 35 kVp, with a 30 μm molybdenum filter. The detector was a CMOS image sensor C9732DK-11 (Hamamatsu, Japan) with a pixel size of 50×50 μm^2. However, the effective pixel size in the x-direction was 100 μm due to the line-skipping design of the detector-mask, where every second detector pixel column is completely covered [111], and was therefore discarded during data processing. Both masks were fabricated by electroplating gold strips onto a graphite substrate (Creatv Microtech Inc., Potomac, MD, USA), and their dimensions and relative distances matched those implemented in the simulation study (apart from the fact that the detector-mask period was 98 μm, since in reality there is a 4 cm gap between the mask and the detector). The CT scan consisted of 360 equally spaced views, acquired over 180 degrees. At

each view, flat-field and sample images were acquired at the left and right positions of the sample-mask ($x_e = \pm 8\mu m$). For sample images, 16 dithering steps were employed. The exposure time per projection was 4 s. Data processing and CT reconstruction followed the same procedure described above.

The reconstructed experimental phase slices presented a "clumpy" noise structure in addition to ring artefacts. Their NPS was evaluated (an example is provided in Fig. 4.7(a,c)): it can be seen that the noise power of the experimental slice (blue line in panel (c)) has high concentration at low frequencies, and presents small peaks at regular intervals, which correspond in real space to the sample-mask periodicity.

In an attempt to recreate the appearance of the phase slice (and hence its corresponding NPS) using simulated data, different combinations of the above mentioned error/noise types were added to the simulated signal. However, the first type of error described (related to ring artefacts) was omitted in the simulation, owing to its strong dependency on both the chosen error values and their position on the detector row. Figure 4.7(b) shows a simulated phase slice which was reconstructed using a combination of the errors described above, and its corresponding NPS is plotted in panel (c, red line) and shows good agreement with the experimental NPS.

In addition, the phase slice shown in Fig. 4.8 was reconstructed from the same experimental data, however with the correction for intensity variations between dithering steps images removed. This is a good example for an extreme case of the 3rd type of noise modelled by the simulation, and similar features in the noise structure are seen both in the reconstructed

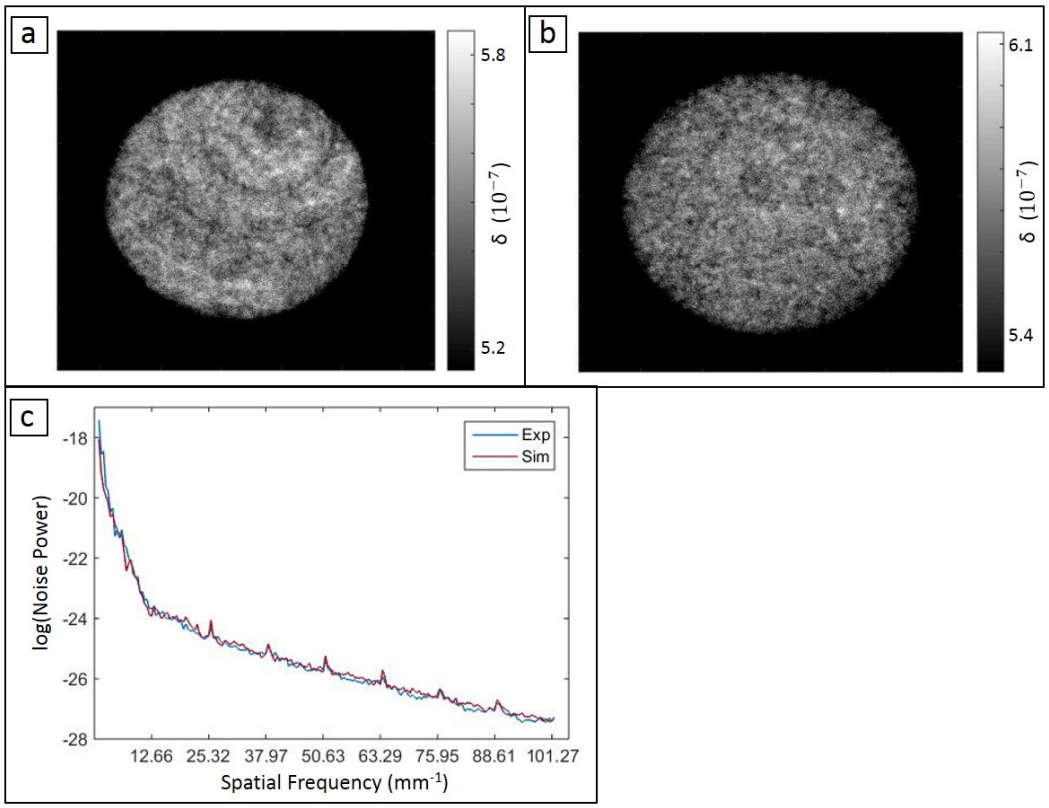

Figure 4.7: Experimental (a) and simulated (b) phase slices, and a comparison between their NPS (c).

slice and in its NPS (panel (b)). As previously mentioned, this error is routinely corrected for in the processing of the data by rescaling the dithering steps images appropriately prior to phase retrieval.

4.1.3 Conclusion

A simulation study was performed to investigate the different types of noise and errors which can be present in EI CT scans performed in the laboratory, and their effect on the reconstructed phase slices. This was motivated by inconsistencies in image quality of CT datasets acquired for different samples.

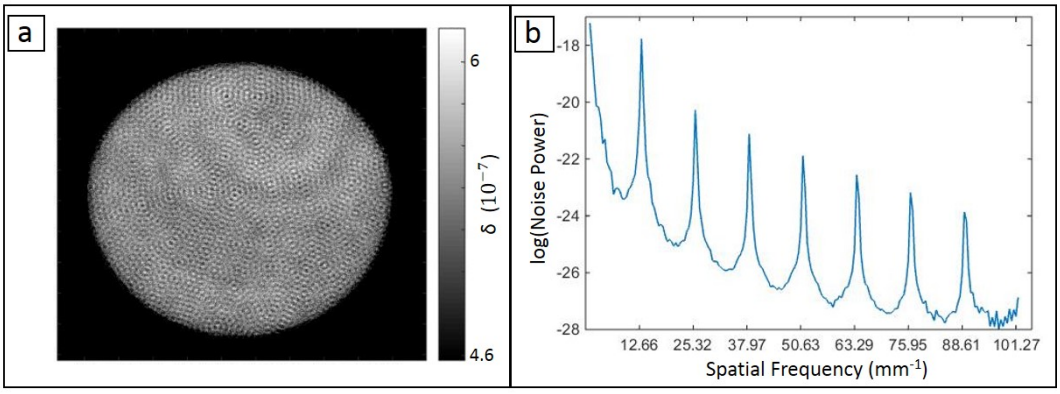

Figure 4.8: Reconstructed phase slice (a) and its NPS (b) from experimental data, where no correction was applied for intensity variations between dithering steps images.

Four different sources of errors were described and modelled, and their effect on reconstructed phase slices was examined, by both visual evaluation of the CT slices, and analysis of the NPS. It was shown that errors due to defects in the masks or detector pixels manifest as blurred, thick rings, while the use of the same flat-field image for normalization of all dithering steps in a particular view leads to a "clumpy" noise structure. In addition, random intensity variations between dithering steps, which are not fully corrected for prior to the phase retrieval step, create a repeating noise pattern on small length-scales, determined by the the number of dithering steps and the period of the sample-mask. Last, if shot noise is spatially correlated, e.g. by the detector cross-talk, it can lead to both repeating noise patterns on a short length-scale and a clumpy noise structure over longer length-scales.

A combination of these modelled errors was then used to generate a simulated phase slice with visual resemblance to an experimental slice, and good agreement between their respective NPS. This work therefore contributed to the understanding of different sources of noise and artefacts in EI CT, hence enabling the

development of strategies for their reduction, such as the phase retrieval algorithm described in the following section.

4.2 Retrieval algorithm for high-resolution, multi-modal EI CT in non-ideal environments

4.2.1 Background and motivation

As previously mentioned, through dedicated algorithms, the EI method enables the quantitative retrieval of absorption, refraction and ultra-small-angle scattering in the sample [3, 77], and the spatial resolution in the image can be increased beyond that traditionally determined by the detector pixel size, through the use of sample dithering [17]. The use of these characteristic features in combination with the lab-based CT implementation of EI, can be beneficial to a wide range of applications.

While both scan time and dose are increased with the number of dithering steps and number of retrieved contrast channels, for certain applications (e.g. material science and ex-vivo medical research), the requirements of high spatial-resolution and multi-modality may be more important than dose or scan time considerations. Such scans however are inevitably long, leaving the system susceptible to environmental changes, which can in turn lead to image artefacts in the reconstructed CT data.

In this section, a robust phase retrieval method is presented, developed to provide a solution for long, high-resolution EI CT scans in non-ideal environments. The retrieval algorithm is based on a "local" retrieval method developed by Endrizzi

et al. [78] which has been shown, using planar imaging, to be robust against a significant degree of system misalignment. The new "modified local retrieval" algorithm presented here has been developed specifically for CT scans, which are substantially longer, and more sensitive to local misalignments due to the integration step necessary for the retrieval of δ from differential phase sinograms. Furthermore, this new algorithm removes the need to acquire flat-field images at every projection, thereby leading to a substantial reduction of scan time compared to the previous method, and a potential reduction in the clumpy noise structure described previously (see section 4.1.2). Importantly, this adaptation incorporates corrections of time-varying system components, which could be due to e.g. vibrations or temperature fluctuations, affecting the source and/or the masks. This is particularly relevant since EI CT is suited for use with commercial X-ray tubes, and so its ability to provide high precision, quantitatively reliable data in environments affected by such instabilities is crucial to its future translation into realistic sites such as hospitals and factories. Possible sources of instability were analyzed, modelled, and incorporated into the simulation framework described at the beginning of this chapter. Following validation on a simple geometrical phantom, experimental results of a complex biological sample are presented, demonstrating a very significant improvement in image quality thanks to the new retrieval method.

4.2.2 Theory

Current EI phase retrieval methods allow the extraction of three different sample properties: absorption, refraction and scattering. These can be linked to changes

in the detected intensity distribution in an intuitive way, as demonstrated in Fig. 4.9, in which the beams with and without the sample in place are compared, for a single detector pixel. Sample absorption leads to a reduction in the total area, while the shift in the centre position is caused by sample refraction, and sample scattering broadens the beam.

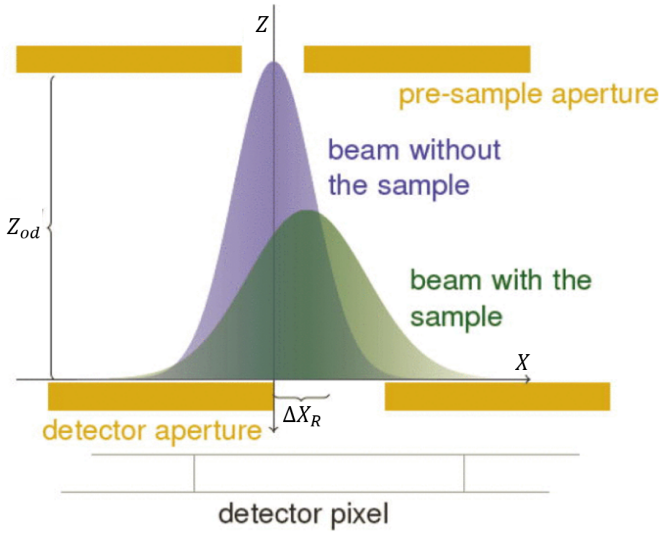

Figure 4.9: Beam distribution in an EI setup, shown for a single detector pixel. The presence of a sample leads to an attenuated, shifted and broadened intensity distribution. Adapted with permission from AIP Publishing: Applied Physics Letters, Ref [3], Copyright 2014.

The intensity recorded with the EI setup by a single detector pixel can be described by:

$$\frac{I(x)}{I_0} = (C * O)(x - \Delta x_R)T \ , \tag{4.1}$$

where I_0 is the intensity transmitted through the sample-mask aperture, C is the IC describing the intensity change as a function of relative masks positioning x (see Fig. 4.11(b)), O is the sample's scattering distribution, Δx_R is the beam shift due to sample refraction, T is the fraction of intensity transmitted through the

sample, and $*$ is the convolution operator [3]. Both C and O can be represented as a sum of Gaussian functions:

$$C(x) = \sum_{n=1}^{N} \frac{A_n}{\sqrt{2\pi\sigma_n^2}} \exp[-(x-\mu_n)^2/2\sigma_n^2] \ , \tag{4.2}$$

$$O(x) = \sum_{m=1}^{M} \frac{A_m}{\sqrt{2\pi\sigma_m^2}} \exp[-(x-\mu_m)^2/2\sigma_m^2] \ . \tag{4.3}$$

Thus Eq. 4.1 can be rewritten as:

$$\frac{I(x)}{I_0} = T \sum_m \sum_n A_{mn} \exp\left[- \frac{(x-\mu_{mn})^2}{2\sigma_{mn}^2} \right] , \tag{4.4}$$

where $\sigma_{mn}^2 = \sigma_m^2 + \sigma_n^2$, $A_{mn} = A_m A_n (1/\sqrt{2\pi\sigma_{mn}^2})$ and $\mu_{mn} = \mu_m + \mu_n$.

Equation 4.4 can be analytically inverted to obtain solutions for absorption, refraction and scattering, in the case where three images are acquired in positions $x_1 = -x_3$, $x_2 = 0$ with respect to the IC ("global retrieval") [77]. When applied to experimental data, this approach therefore assumes the same positions on the IC for every pixel over the entire FOV, not taking into account local variations due to misalignment of optical elements or masks imperfections. These variations are mostly compensated for by normalizing the raw data by flat-field images.

As has been shown by Endrizzi *et al.* [78], Eq. 4.4 can also be used to retrieve sample absorption, refraction and scattering, without making any assumptions on system alignment. This is done by applying it on a pixel-by-pixel basis, where Eq. 4.4 is used as a model function for a non-linear curve-fitting, solved by the least-squares method: the intensity values from the IC scan are used to obtain reference values for each pixel, of the amplitude, mean, standard deviation and

offset of the curve. Then, for the same pixel, the intensity values from the sample images acquired at the three different positions of the sample-mask are used in the curve-fitting process. The parameters (amplitude, mean, standard deviation and offset) of the fitted curve are then compared to the reference values, resulting in the extraction of sample absorption, refraction and scattering. Therefore, owing to its pixel-by-pixel computation, this method ("local retrieval") automatically takes system misalignment and mask defects into account and corrects for them. This has been applied to planar data, and was shown to correct for a significant degree of system misalignment [78].

While the algorithm described here is based on the local retrieval method, a further extension of the retrieval equation was required in order to adapt it for use on CT scans. Since sample properties are extracted from comparison with reference parameters drawn from the IC scan, if the latter change over time due to system instabilities, the model should account for such changes. In particular, as shown below, it was found that the mean position of the IC varies over time. To accommodate for this variation, two correction steps were implemented: the first was real-time illumination tracking during the scan (as described below), while the second was incorporated into the retrieval algorithm and involved the use of information from background regions in the images. This additional information was used to estimate the new mean position of the IC (hence updating the reference value), and therefore added a degree of freedom to the fitting process. The correction term $\Delta\mu$, corresponding to the translational shift of the IC, was incorporated into Eq. 4.4 in the following way:

$$\frac{I(x)}{I_0} = T \sum_m \sum_n A_{mn} \exp\left[- \frac{(x - \mu'_{mn})^2}{2\sigma^2_{mn}} \right], \tag{4.5}$$

where $\mu'_{mn} = \mu_m + \mu'_n$, $\mu'_n = \mu_{n(ij)} + \Delta\mu$, and i and j correspond to individual pixel coordinates.

The illumination curve's mean position can be calculated for each pixel as $\mu_{n(ij)}$ from an initial IC scan. To find the translational shift of the IC over time, begin by defining a background area in the FOV. This background region could be any part of the FOV which is not covered by the sample throughout its rotation. However, since information from this region is used to generate correction terms for the sample data, it is beneficial that the background region is chosen as close as possible to the sample, typically next to it or above it. For each pixel in the background region, the new position of the illumination curve's mean is estimated as $\mu_{n\_im(ij)}$ by means of a least-squares curve fitting using values from the three images acquired at each dithering step. The shift $\Delta\mu$ is then determined according to:

$$\Delta\mu = \frac{\sum_i \sum_j \mu_{n\_im(ij)} - \mu_{n(ij)}}{N_{ij}} \ , \tag{4.6}$$

where N_{ij} is the total number of pixels in the defined background region. The shift $\Delta\mu$ is then applied in the phase retrieval to all pixels in the same dithering step image. Notably, in contrast to the global retrieval, here no flat-field images are needed for processing, as all the required pixel-wise information is drawn from the IC scan.

A diagram of the image reconstruction workflow using the modified local retrieval algorithm is shown in Fig. 4.10.

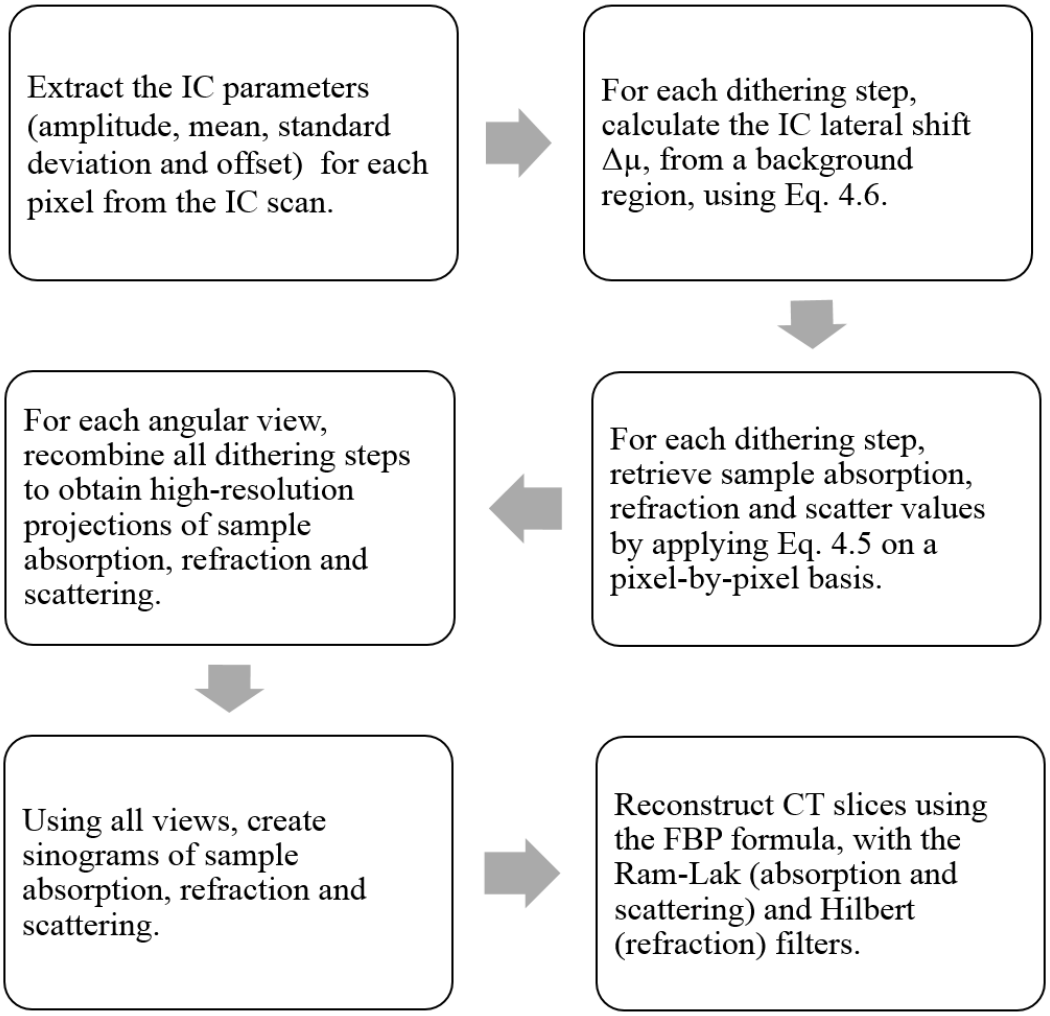

Figure 4.10: The image reconstruction workflow using the modified local retrieval algorithm.

4.2.3 Methods

Both the experimental and simulated scans described below were performed using the conventional, lab-based EI CT setup depicted in Fig. 4.11(a) (or its simulated equivalent). The working principles were described previously in chapter 2 (see 2.5), and the employed source, detector, masks and relative distances matched those described in the first part of this chapter (see 4.1.2).

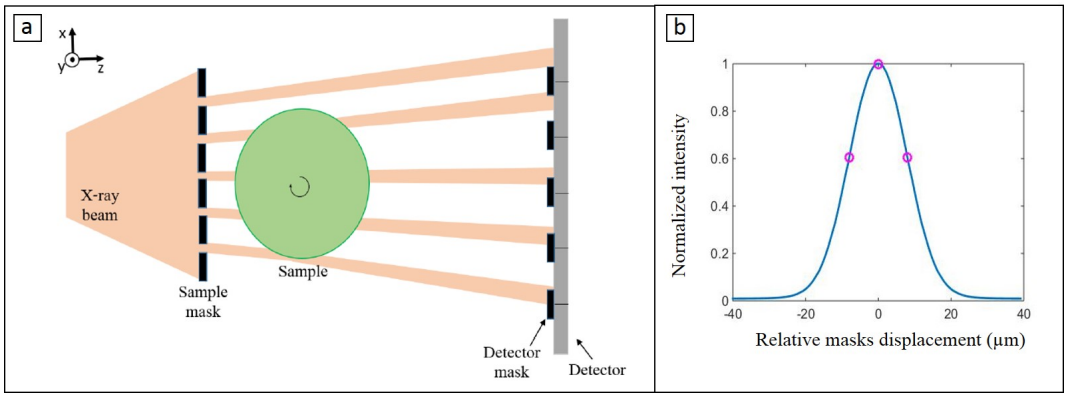

Figure 4.11: (a) A top view of an EI setup with an extended X-ray source. For CT, the axis of rotation is aligned with the y direction, while the sample is moved by sub-pixel steps along x for dithering. (b) A typical IC showing intensity variation as a function of masks displacement over one period. The circles represent typical choices of mask positions for imaging.

Simulation study

To analyze and understand the effect of system misalignment on the retrieved phase slices, a simulation study was performed, using the same simulation framework described above [106]. The simulated sample was a uniform rod (1 cm diameter) with refractive index values similar to those of the experimental data shown below (see 4.2.4): $\delta = 1.7 \times 10^{-7}$ and $\beta = 2.7 \times 10^{-10}$. A photon energy of 17.5 keV was assumed, corresponding to the k-alpha line of the molybdenum target used in the laboratory source.

To test the performance of the proposed retrieval method, system misalignment was modelled and incorporated into the simulation. This was done by extracting the IC parameters of each pixel in a detector row from an experimental measurement of the IC. The position of the mean of the IC for each pixel was used to model pixel-wise misalignment in the simulation, by adding it as an offset to the centre position of each aperture in the sample-mask, before the generation of the

simulated detected signal. This is equivalent to each pixel featuring the same IC, however centred on a different position.

To perform global retrieval, flat-field signals were generated as well, however with a slightly different misalignment, as is the case in an experimental environment. The flat-field's misalignment values were taken from the same detector row used for the sample signals, however from a subsequent experimental IC scan. Sinograms were generated at three positions on the IC (at relative masks displacement $x_e = -8, 0, +8\mu m$, see circles in Fig. 4.11(b), before adding the misalignment offset). To test the global retrieval, sample sinograms were first normalized by the flat sinograms, as would happen in a standard experimental procedure. The normalized sinograms were then processed with the 3-image global retrieval algorithm, using the same illumination curve for the entire FOV. To test the modified local retrieval, sample sinograms (no flat normalization) were processed with the proposed algorithm, using a differently centred illumination curve for each pixel, according to the input misalignment. Sinograms of the sample's differential phase, absorption and scattering properties were produced from each of the retrieval methods. For CT reconstruction of the phase maps, the FBP algorithm was used with the Hilbert filter.

IC stability

One of the greatest advantages of the EI method is that it is suited for use with commercially available X-ray source and detector technologies, making its translation to clinical and industrial environments possible. However, such environments are likely to suffer from non-ideal imaging conditions, such as temperature instabilities and vibrations of the experimental setup. As all retrieval methods

described above rely on the knowledge of the IC, and since high-resolution CT scans can last hours, it was necessary to observe changes in the IC over time. Using the experimental setup described above, multiple illumination curves (one every 15 minutes, over three days) were acquired and analyzed. While the shape and amplitude of the IC remain reasonably constant over time, the position of the mean was found to vary in a cyclical pattern, as shown in Fig. 4.12. The laboratory currently used for EI scans has no measures in place for vibration damping or temperature insulation, and the plot shown in Fig. 4.12 demonstrates that indeed environmental changes can have a significant impact on the IC. To accommodate for these large drifts and ensure that images are acquired at the correct illumination positions (thus maintaining high refraction sensitivity), real-time tracking of the illumination level was implemented into the CT scan. Here, the required spatial shift of the sample-mask is found by comparing the intensity of a background region in an image to the desired value from the initial IC scan. The positions of the sample-mask and sample are then adjusted accordingly.

Experimental data acquisition and processing

A CT scan was performed using the laboratory setup described above. The source was operated at 25 mA and 40 kVp, and the exposure time per projection was 2 s. An IC was acquired by recording the detected intensity as the sample-mask was shifted with respect to the detector-mask over one period. The scanned sample was a rat heart, placed in a plastic container. The heart was harvested from an adult Sprague-Dawley rat weighing about 300 g. The rat was sacrificed by CO_2 inhalation and cervical dislocation. Once sacrificed, a midline incision was made

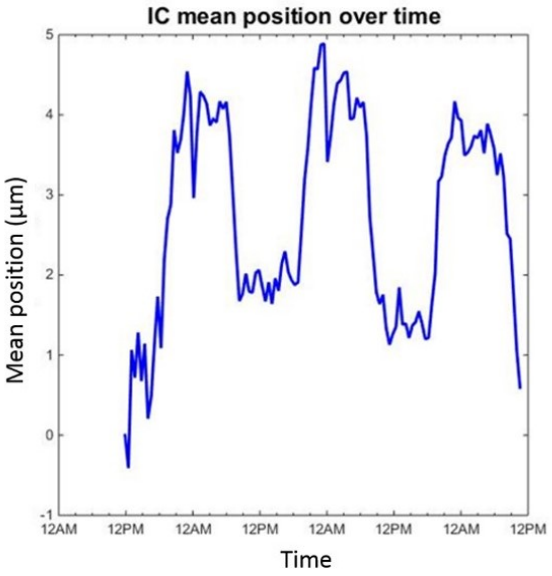

Figure 4.12: The position of the mean of the illumination curve (IC) as a function of time, taken from experimental data collected over 3 days. The IC analysis considered an area of 50x50 pixels in the centre of the FOV.

to completely expose the abdominal cavity and the heart was dissected free and removed. The organ was then washed with PBS and fixed in 4% PFA overnight. The heart was freeze-dried at a pressure of 10 mBar overnight in a petri dish.

The scan consisted of 360 views over 180 degrees, with 6 dithering steps per view corresponding to a resolution of approximately 13 μm in the x-direction, and 3 images (at different positions on the IC) for each dithering step. Flat-field images were acquired at each view, as they are required for the global-retrieval processing. The modified local retrieval does not require flat-field images for normalization, and so the new procedure allows avoiding them completely in the future.

The experimental data was processed using the two different phase retrieval methods (global and modified local), according to Eqs. 4.4 and 4.5. Although the real-time illumination tracking procedure ensures that large shifts of the IC are mitigated, a small shift of the IC was observed between consecutive dithering

steps. The shift was calculated for each dithering step image using Eq. 4.6, and the adjusted values were used in the modified local retrieval.

To reduce noise levels in the absorption and scattering sinograms, a 1-dimensional median filter was applied to the sinograms, using values from 8 (absorption) and 16 (scattering) neighbouring pixels. CT reconstruction of absorption, scattering and phase maps was performed using FBP with the ramp (absorption, scattering) and Hilbert (phase) filters.

4.2.4 Results

Data of a rod, simulated with included system misalignment, was used to compare the performance of the two retrieval methods. Figure 4.13 presents reconstructed CT images of the sample's phase, processed with the global (a) and modified local (b) retrieval. The plot shown (c) compares profiles taken through the centres of both slices. As expected, the reconstructed slices confirm that masks misalignment leads to significant artefacts when global retrieval is used, due to systematic errors in specific pixels. As well as ring artefacts, a gradient can be observed across the slice in Fig. 4.13(a). This is a result of a gradient and/or offset in the retrieved differential phase projections due to misalignment, combined with the fact that sample rotation was over a 180 degrees range. While this could in principle be reduced by acquiring projections over 360 degrees, it is completely avoided when the modified local retrieval algorithm is used, as seen in Fig. 4.13(b). As well as demonstrating the removal of artefacts such as rings and gradients, the results confirm that the method is quantitative; the retrieved δ value was $\delta_{ret} = (1.72 \pm 0.06) \times 10^{-7}$, compared to the theoretical input value

$\delta_{th} = 1.70 \times 10^{-7}$. The small variations in the locally retrieved δ profile are due to numerical errors of the fitting process used in the algorithm.

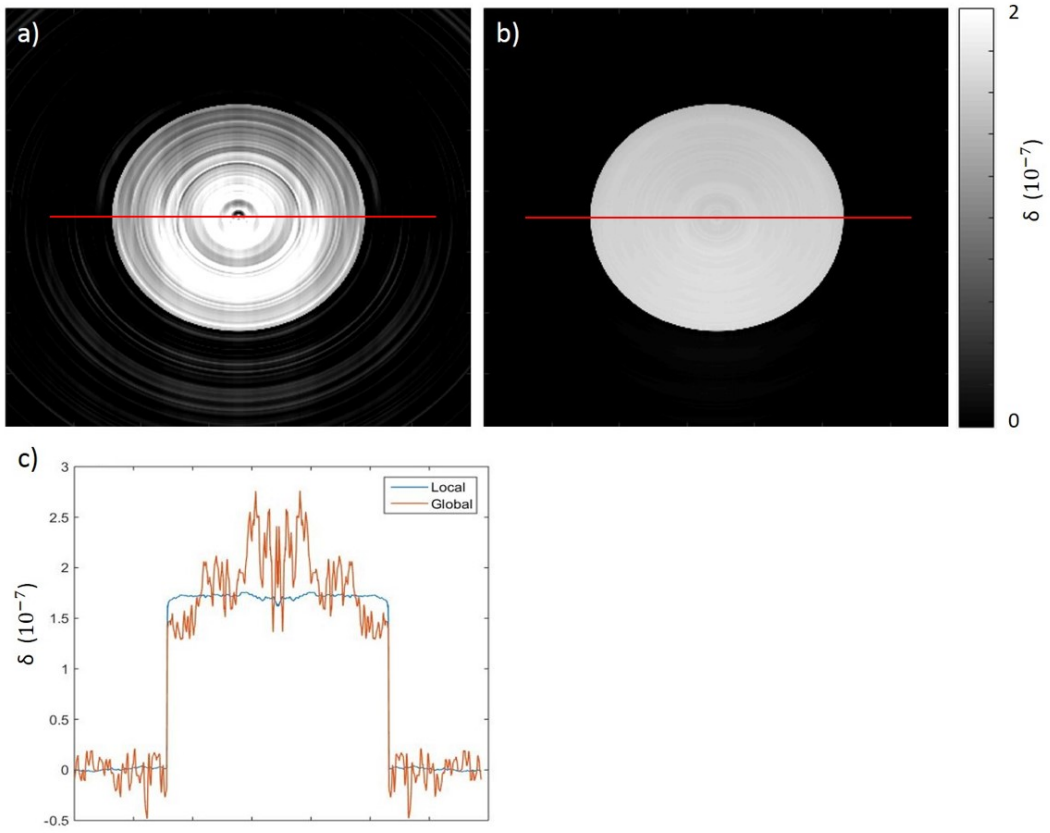

Figure 4.13: Phase maps of simulated data of a rod processed with global (a) and modified local (b) phase retrieval. The reduction of artefacts can be further appreciated by plotting a profile through the slices' centre (indicated by the red lines in (a) and (b)), as shown in (c).

Following confirmation of the effective adaptation to CT of the local retrieval approach through simulation, the method was tested on experimental data of a complex biological sample. In Fig. 4.14, slices reconstructed with global retrieval are shown on the left (a,c) while the panels on the right (b,d) display the same slices processed with the modified local retrieval approach. As can be seen, there is

a dramatic improvement in image quality. Areas of severe masks defects can cause complete loss of information (as seen in the central region in Fig. 4.14(c)), which can however be fully recovered by using the modified local retrieval. As predicted by the simulation, the globally retrieved slices also suffer from a gradient, which is completely eliminated in the locally-retrieved slices.

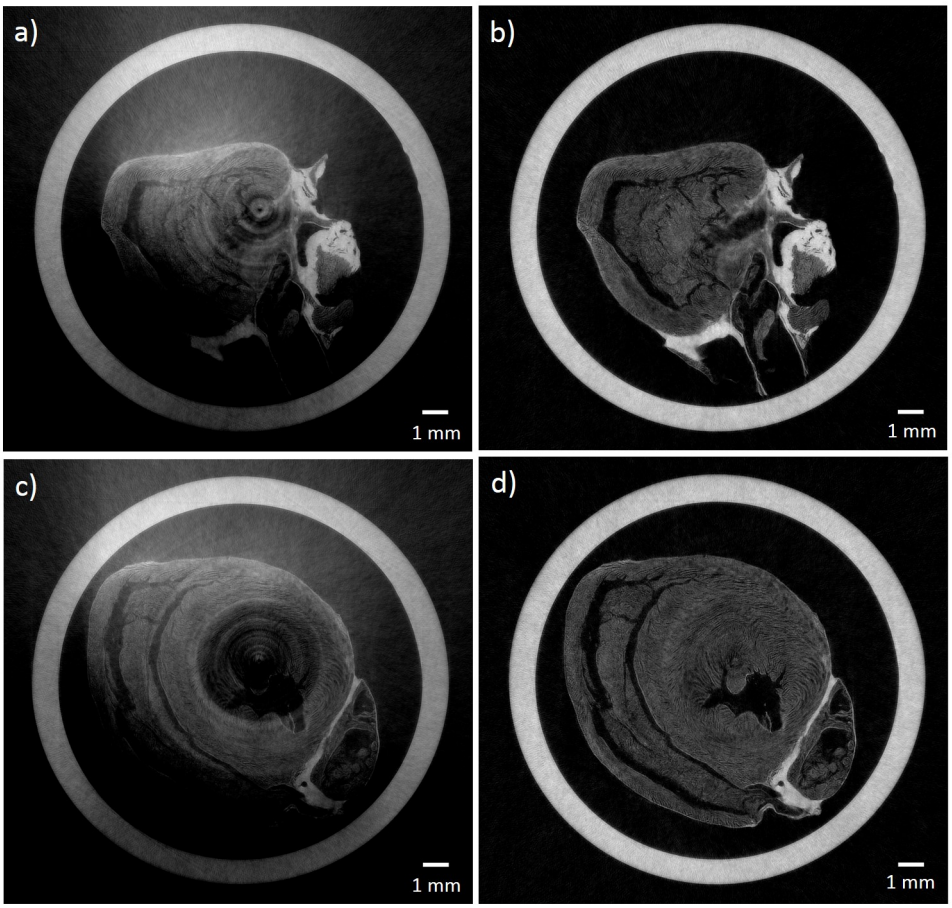

Figure 4.14: Transverse phase slices of experimental data of a rat heart, showing the superiority of data retrieved with the modified local method (b,d) compared with global retrieval (a,c).

It should be noted that the transition from global to local retrieval mostly affects the retrieved refraction image, while only marginally altering the absorption and scattering images. This is easily understood by considering that, when local mis-

alignment is not taken into account, the algorithm incorrectly attributes changes in the mean position of the IC to refraction by the sample. Absorption and scattering signals are determined by changes in the amplitude and width of the beamlets with and without the sample, which are well-described in both cases through the use of three input frames. Figure 4.15 displays the results of CT reconstruction of the phase, absorption and scattering (a-c respectively) signals of experimental data retrieved with the modified local method. Corresponding magnified views of a region in the heart (rectangle in Fig. 4.15(a)) are shown in panels (d-f). When comparing these three channels, it should be noted that the application of the median filter on absorption and scatter data has introduced a substantial blur to the reconstructed CT slices. However, it should be noted that filtering was necessary in order to improve the CNR; without filtering, most features which are now visible would have been hidden in the noise floor. For the phase slice, no median filtering was required due to its intrinsically high CNR. As a result, features in the heart are more clearly visualized in the phase slice.

The scattering distribution slice provides some complementary information about regions in the sample with refractive index inhomogeneity on a scale smaller than the aperture size of the sample-mask. For example, the disappearance of the cylinder in the scattering slice confirms it is a highly homogeneous material. The structures seen in Fig. 4.15(d) appear to be the result of "cracks" in the cardiac muscle tissue, possibly caused by the freeze-drying process.

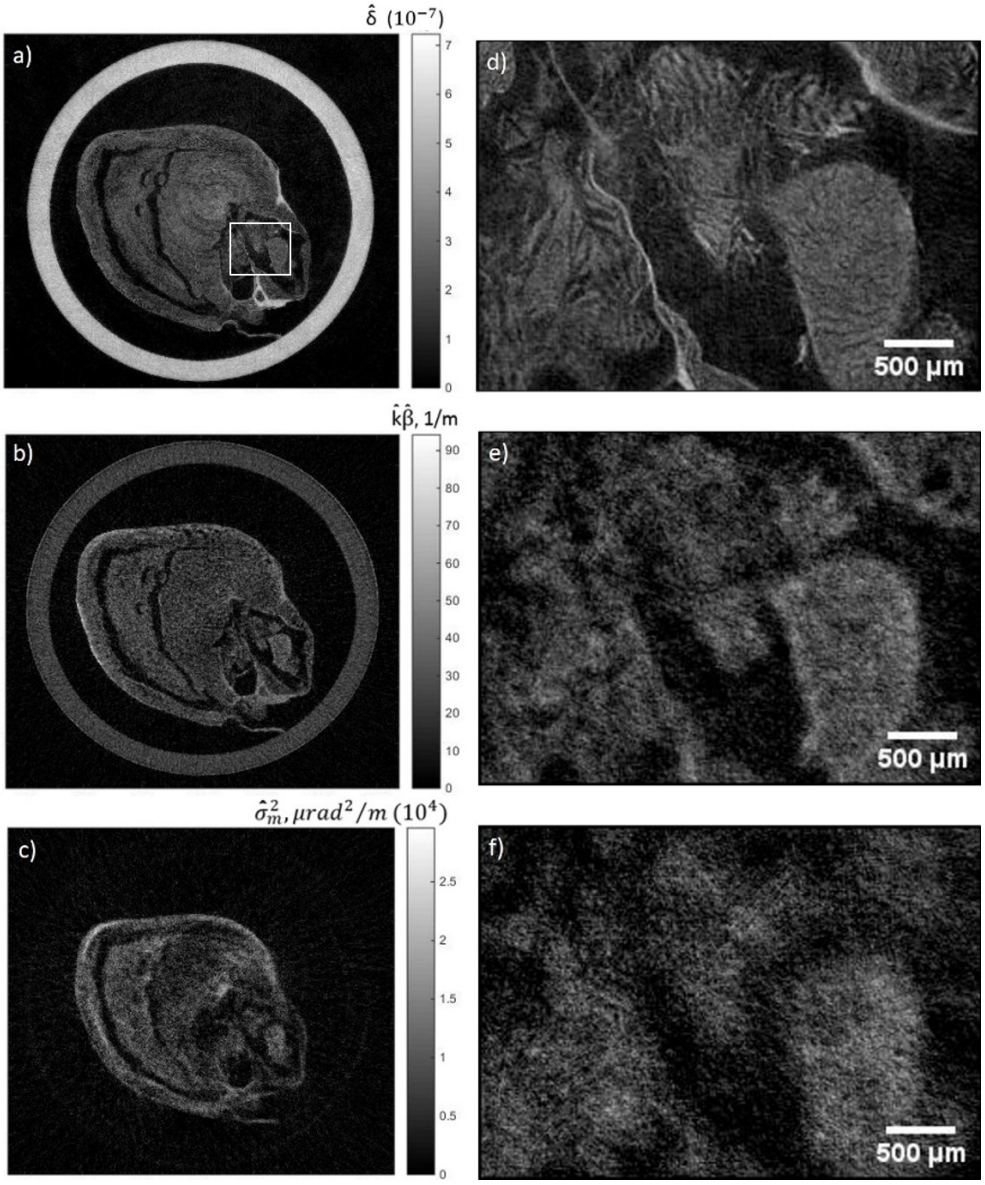

Figure 4.15: CT reconstructed slices of the phase (a), absorption (b) and scattering distribution (c) of a rat heart, processed with the modified local phase retrieval. As these data were acquired with a polychromatic spectrum, the reconstructed maps refer to sample properties estimated at effective energies, indicated by the hat symbol. (d-f) show their corresponding magnified views of the region in the rectangle in (a).

4.2.5 Discussion and conclusion

A robust phase retrieval method has been presented, capable of correcting for local misalignment and changes to system geometry that might happen during long acquisitions. This is especially relevant for long, high-resolution multi-modal CT scans, during which system parameters have been shown to vary significantly over time, as the source and/or masks can move unexpectedly, due to vibrations and/or thermal effects. By processing simulated data with the global version of a 3-image retrieval algorithm, it has been demonstrated that ring and gradient artefacts in phase slices are related to projections acquired with system misalignment and/or masks defects, as these create systematic errors in the retrieved quantities. The modified local retrieval method is able to correct for these systematic errors, resulting in the removal of artefacts and therefore in a significant improvement in the quality and quantitativeness of reconstructed images. When applied to experimental data, locally-retrieved phase slices were free of artefacts, even in areas where the globally-retrieved slices had rings with up to 100% intensity variation.

While it is common practice to acquire flat-field images before and/or after a scan, until now in EI CT, flat-field images were usually taken at each rotation angle, as has been done here for the "global" processing. In situations where there are mild changes to system parameters over time, this approach helps minimizing normalization problems. However, as has been shown, here some parameters had a significant degree of time dependency, and so the use of multiple flat-field images was not sufficient to improve image quality. In contrast, the new retrieval method provides improved image quality, while requiring no flat-field images,

thereby reducing the EI CT scan time substantially.

The proposed retrieval method is computationally intensive when compared with the global retrieval, since the fitting process has to be repeated for each pixel in the image. However, once the shift of the IC is calculated using three frames per image, the pixel-wise computation implies that the rest of the process can be parallelized. Combining this with the possibility to compute in parallel different rows in the image, different projection angles and different dithering steps images, offers opportunities to significantly reduce computation time.

As mentioned before, the retrieved refraction signal in EI is proportional to the derivative of the phase shift, and so reconstruction of the phase shift (and hence δ) requires a 1-dimensional integration (here, performed by the Hilbert filter in Fourier space). This integration is considered problematic, as any local errors in the retrieved signal are propagated and affect the image globally, resulting in artefacts [112]. This emphasizes the need for a phase retrieval method which reduces the errors in the locally-retrieved signal, such as the one presented here. Furthermore, the modified local algorithm inherently avoids/reduces 3 out of the 4 sources of error and noise described in 4.1.2: systematic errors are corrected through pixel-wise computation, flat-fields are not required for normalization, and intensity changes between dithering steps are corrected using the shift correction term $\Delta\mu$.

While the experiment reported here served as a proof-of-principle on a small biological sample, it is expected that the method should perform equally well on large samples, owing to its pixel-by-pixel computation. The resolution can be further increased by using masks with a smaller aperture size and increasing the number of dithering steps used, although at the cost of a longer scan duration

and increased computation time. Nonetheless, the presented retrieval method and associated correction for time-varying components have the potential to reliably provide CT scans with a resolution of the order of 10 μm on large samples, in non-ideal imaging environments affected by vibrations and/or temperature changes.

5

Single-image retrieval algorithm for fast CT scans of complex samples

5.1 Background and motivation

The retrieval algorithm presented in the previous chapter targeted applications which require the extraction of multiple contrast channels, from high resolution lab-based EI CT scans. Such scans are inevitably long as multiple images per view are required, corresponding to different positions of the sample-mask, and different sub-pixel positions of the object (required by the dithering process). For many applications however, in particular in the biomedical field, the ability to perform fast CT scans with reduced dose, is more important than the quantitative retrieval of multiple contrast channels. Ultimately, the development of strategies for robust and fast EI CT scans has the potential to transform it into a high

throughput imaging tool, suitable for e.g. pre-clinical in-vivo applications.

In chapter 2, when reviewing the extension of EI to CT and its subsequent developments, three retrieval algorithms aimed at reducing scan times were briefly mentioned. Out of the three, it is Diemoz's retrieval algorithm which can lead to the greatest reduction in scan time, as it requires only a single image per view, and could be implemented with a continuous sample rotation over 180 degrees [89]. In a similar way to the algorithm developed by Paganin *et al.* for FSP [56], Diemoz's algorithm for EI relies on several assumptions, the main one being that the sample is quasi-homogeneous (i.e. that it has a constant ratio between the real and imaginary parts of its complex refractive index). The single-image algorithm was first applied to planar data acquired with SR, and has been shown to provide quantitative results when imaging a homogeneous sample, and enhanced image quality when imaging complex biological samples [82]. Additional developments have made the algorithm suitable for use on CT data acquired in a laboratory environment, with an extended and polychromatic X-ray source [89]. The potential for reduction in scan time was clear: while lab-based, multi-modal high resolution CT scans can last hours, the use of the single-image algorithm resulted in the reconstruction of a high quality CT dataset from a scan with an unprecedented acquisition time of only 3.3 minutes [89] (made possible mainly due to the continuous rotation of the sample, enabled by eliminating the need to acquire multiple frames at each CT angle while displacing the sample-mask). However, although high image quality was observed for a range of samples which can be considered approximately homogeneous (e.g. rat heart), many biological samples of interest are not quasi-homogeneous (e.g. contain both soft-tissue and bone), and applying the algorithm to such samples will result in under or over-

retrieved characteristic features (dark/bright fringes, blurring). For example, still in the results presented in [89], this can be seen as blurring around a chalk detail embedded in a phantom containing various plastic materials.

The work presented in this chapter aimed to overcome the main limitation of Diemoz's algorithm (i.e. the assumption of a sample made of a single material), by extending it such that it could be applied to multi-material samples. Such a development would expand the range of samples which could benefit from fast EI CT scans, and be particularly significant for biomedical applications, since samples containing both bone and soft-tissue could be scanned.

The algorithm developed in this chapter ("multi-material, single-image algorithm") follows the work of Beltran *et al.* who extended Paganin's single-image retrieval algorithm for FSP, to the case of a multi-material object [97, 98], as was briefly described in chapter 3. While still requiring only a single image per projection, the multi-material, single-image algorithm can correctly reconstruct the interface between any two materials (when one is encased by the other), by tuning the relevant input parameters. When a sample is made of various materials, the algorithm can be applied multiple times, once for each pair of materials, and a "splicing" method can then be used to obtain a composite CT slice, in which all materials are adequately displayed.

5.2 Theory

In this section, the theoretical derivation of the EI single-image phase retrieval for samples made of multiple materials is presented. Consider the typical laboratory EI system which has been described in detail in chapter 2 and schematically

shown in Fig. 2.5. As previously explained, when the two masks are misaligned with respect to each other, refraction of the beamlets caused by the sample in the direction perpendicular to the masks' apertures is converted into detectable intensity changes, which are proportional to the first derivative of the phase, Φ. Image formation in the direction parallel to the masks' apertures can be treated as FSP, where the signal recorded is proportional to the second derivative of the phase [17, 113]. It should be noted however, that in the lab-based EI implementation, the FSP signal is very weak due to the use of an extended source. Assuming a near-field regime, and that the sample's attenuation and phase are varying slowly, the signal can be modelled by the TIE [54, 113]. Indeed, for the development of the single-image retrieval algorithm, Diemoz used the TIE as a starting point for the derivation, leading to the following expression for the normalized signal recorded by an EI setup [89]:

$$S_n = \left\{ T - T\frac{C'(x_e)}{C(x_e)} k^{-1} z_{od} \nabla_x \Phi - k^{-1} z_{od} \nabla_y [T \nabla_y \Phi] \right\} * LSF_y \ , \tag{5.1}$$

where $T = \exp(-2k \int \beta(x,y,z)dz)$ and $\Phi = -k \int \delta(x,y,z)dz$ are the transmission and phase shift caused by the sample, respectively. As before, the IC (denoted by C) describes the measured intensity as a function of the relative masks' displacement, x_e, in the absence of a sample. The object-to-detector distance is denoted by z_{od}, and LSF_y is the detector's line spread function along the direction parallel to the masks' apertures. Differentiation with respect to x or y is represented by $\nabla_{x,y}$ and $*$ indicates convolution. It can be seen that in Eq. 5.1, the first term is the conventional attenuation signal, the second term is the EI signal along x,

and the third term is the FSP signal along y.

By assuming a homogeneous sample which is sufficiently thin such that it satisfies the projection approximation, the transmission and phase at the sample's exit surface can be both expressed as a function of the sample's thickness, $t(x, y)$:

$$T(x, y) = \exp(-2k\beta t(x, y)) \ , \tag{5.2}$$

$$\Phi(x, y) = -k\delta t(x, y) \ . \tag{5.3}$$

Diemoz has shown that by substituting Eqs. 5.2 and 5.3 into Eq. 5.1 and defining $J_{EI} = z_{od}C'(x_e)C^{-1}(x_e)$, an expression for the sample's projected thickness can be obtained [82]:

$$t = -\frac{1}{\mu}\log\left[F^{-1}\left\{\frac{F\{S_n\}}{MTF_y(k_y)\cdot[1 + iJ_{EI}\delta\mu^{-1}k_x + z_{od}\delta\mu^{-1}k_y^2]}\right\}\right] \ , \tag{5.4}$$

where $\mu = 2k\beta$ is the linear attenuation coefficient, F and F^{-1} represent the 2-dimensional Fourier transform and its inverse, $k_x = 2\pi f_x$ and $k_y = 2\pi f_y$ where f_x and f_y are the Fourier space coordinates, and the system's modulation transfer function along y is given by $MTF_y(k_y) = F\{LSF_y\}$. When a polychromatic beam is used, both δ and μ should be evaluated at their *effective* energies [76, 89]. Therefore, when a homogeneous sample of known material is imaged with monochromatic radiation, Diemoz's algorithm will retrieve quantitative values for the object's thickness. While in the case of inhomogeneous samples the retrieved results would not be quantitative, often high image quality can still be achieved

by tuning the input δ and μ values following an initial guess. This however is not the case for a sample made of various materials with significantly different refractive index properties, which was the motivation behind the work presented in this chapter.

In the following, the multi-material algorithm is developed by adapting the derivation first presented for FSP by Beltran *et al.* for a ternary object (composed of two materials and voids) [97], to the case of EI. For simplicity, the algorithm is derived assuming monochromatic radiation.

Consider an object made of two materials denoted by 1 and j, where material j is fully encased by material 1. The corresponding refractive indices are $n_1 = 1 - \delta_1 + i\beta_1$ and $n_j = 1 - \delta_j + i\beta_j$, with $\beta_1 = \mu_1/2k$ and $\beta_j = \mu_j/2k$. For monochromatic radiation, Eq. 5.1 describes the detected normalized signal. Assuming the sample satisfies the projection approximation, the transmission and phase shift at the sample's exit plane are given by:

$$T(x, y) = \exp[-(\mu_1 t_1(x, y) + \mu_j t_j(x, y))], \tag{5.5}$$

$$\Phi(x, y) = -k(\delta_1 t_1(x, y) + \delta_j t_j(x, y)) \ , \tag{5.6}$$

where $t_1(x, y)$ and $t_j(x, y)$ are the projected thicknesses of materials 1 and j in the direction of wave propagation, z. By defining the total projected thickness as $A(x, y) = t_1(x, y) + t_j(x, y)$, the transmission and derivatives of the phase can be expressed as follows:

$$T = \exp[-\mu_1 A] \exp[-(\mu_j - \mu_1)t_j], \tag{5.7}$$

$$\nabla_{x,y}\Phi = -k[\delta_1 \nabla_{x,y} A + (\delta_j - \delta_1)\nabla_{x,y} t_j] \ . \tag{5.8}$$

where dependencies on x and y have been discarded for notation simplicity. By substituting Eqs. 5.7 and 5.8 into Eq. 5.1, a solution for t_j can be obtained. Eq. 5.7 is in fact the first term on the RHS of Eq. 5.1. The second term on the RHS becomes:

$$\begin{aligned} T\frac{C'(x_e)}{C(x_e)}k^{-1}z_{od}\nabla_x\Phi &= -(\delta_j - \delta_1)J_{EI}\exp[-\mu_1 A]\exp[-(\mu_j - \mu_1)t_j]\nabla_x t_j \\ &= \frac{\delta_j - \delta_1}{\mu_j - \mu_1}J_{EI}\exp[-\mu_1 A]\nabla_x \exp[-(\mu_j - \mu_1)t_j] \ , \end{aligned} \tag{5.9}$$

where the following identity was used:

$$\exp[-(\mu_j - \mu_1)t_j]\nabla_x t_j = -\frac{1}{\mu_j - \mu_1}\nabla_x \exp[-(\mu_j - \mu_1)t_j], \tag{5.10}$$

and it was assumed that the projected thickness of the encasing material is slowly varying (i.e. that the first term on the RHS of Eq. 5.8 is negligible compared to the second term), and hence the terms containing its spatial derivatives can be ignored. This assumption was previously made by Beltran *et al.* [97] and, while it is violated in certain cases (e.g. near the edges of the encasing material, where phase gradients due to the latter are non-negligible), errors resulting from these violations are localized and should not hinder the retrieval of t_j as long as the latter is not in contact with (or in the immediate vicinity of) another interface.

The third term on the RHS is expanded as:

$$\begin{aligned} k^{-1} z_{od} \nabla_y [T \nabla_y \Phi] &= -z_{od}(\delta_j - \delta_1) \exp[-\mu_1 A] \nabla_y \{\exp[-(\mu_j - \mu_1) t_j] \nabla_y t_j\} \\ &= \frac{\delta_j - \delta_1}{\mu_j - \mu_1} z_{od} \exp[-\mu_1 A] \nabla_y^2 \exp[-(\mu_j - \mu_1) t_j] \ , \end{aligned} \tag{5.11}$$

where the following identity was used:

$$\nabla_y \{\exp[-(\mu_j - \mu_1) t_j] \nabla_y t_j\} = -\frac{1}{\mu_j - \mu_1} \nabla_y^2 \exp[-(\mu_j - \mu_1) t_j] \ . \tag{5.12}$$

These terms can be substituted into Eq. 5.1 to get:

$$\frac{S_n}{\exp[-\mu_1 A]} = \left[LSF_y * (1 - \gamma J_{EI} \nabla_x - \gamma z_{od} \nabla_y^2) \right] \exp[-\Delta\mu t_j] \ , \tag{5.13}$$

where $\gamma = (\delta_j - \delta_1)/(\mu_j - \mu_1)$ and $\Delta\mu = \mu_j - \mu_1$.

By taking the 2-dimensional FT of Eq. 5.13 and making use of the Fourier derivative theorem, the following expression is obtained:

$$F\left\{ \frac{S_n}{\exp[-\mu_1 A]} \right\} = \left[MTF_y(f_y) \ (1 - 2\pi i \gamma J_{EI} f_x + 4\pi^2 \gamma z_{od} f_y^2) \right] F\{\exp[-\Delta\mu t_j]\} \ . \tag{5.14}$$

An expression for t_j can then be obtained by inverse transforming both sides of Eq. 5.14 and rearranging:

$$t_j = -\frac{1}{\Delta\mu} \log \left[F^{-1} \left\{ \frac{F\{S_n / \exp[-\mu_1 A]\}}{MTF_y(f_y)(1 - 2\pi i \gamma J_{EI} f_x + 4\pi^2 \gamma z_{od} f_y^2)} \right\} \right] \ . \tag{5.15}$$

For a given experimental setup, Eq. 5.15 can be readily implemented to obtain

quantitative results of the projected thickness of material j, provided that the total projected thickness A, and the refractive indices of both materials are known. The total projected thickness can be easily estimated in common situations when the sample is placed in a cylindrical, full container (as is the case in both examples provided below). However, in other cases where there are voids to consider, $A(x, y)$ can be estimated by forward-projecting a CT slice reconstructed by using Eq. 5.4 for material 1, and setting a threshold to separate object from void, as was previously suggested by Beltran *et al.* [97].

For samples containing multiple materials $j = 2, 3, ...N$, Eq. 5.15 can be applied $N - 1$ times, each time adjusting $\Delta\mu$ and γ such that they correspond to the pair of materials of interest. As long as each material j is fully encased by material 1, the interface between the two materials will be correctly reconstructed. N independent CT slices can be obtained by applying the conventional FBP algorithm to sinograms of t_1 and $t_{j=2,3,...N}$. Each of these slices will provide an accurate reconstruction of the corresponding pairs of materials, while other interfaces will be either under or over-retrieved (appearing either as residual fringes or as blurred interfaces). A composite CT slice, with all interfaces sharply reconstructed, can then be obtained by splicing together these CT slices, each tuned on a different pair of materials. The splicing procedure consists of extracting from each slice the area containing the correctly retrieved pair of materials, and digitally inserting these into a single, composite slice, following the adjustment of background offsets.

The diagram shown in Fig. 5.1 provides a summary of the different steps of the multi-material, single-image retrieval algorithm, and their relative order.

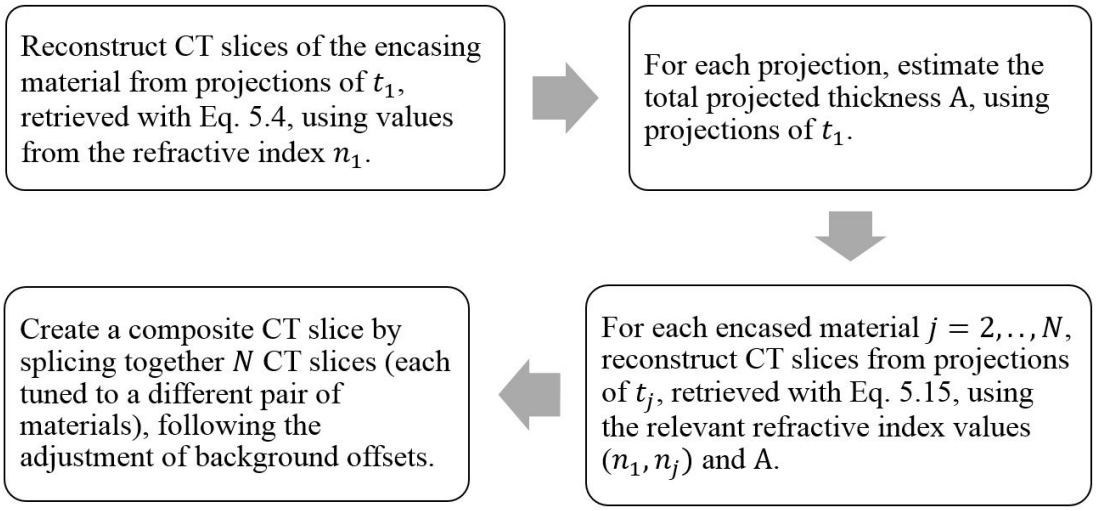

Figure 5.1: The workflow of the multi-material, single-image retrieval algorithm. If the refractive index values are unknown, these can be estimated and tuned until the interface between the two materials of interest is sharply reconstructed in the CT slice.

Note that while Eq. 5.15 was derived for the case of monochromatic radiation, an analogous expression could be developed for polychromatic beams. In a similar way to Diemoz's work [89], since both δ and β vary with energy, a polychromatic extension would involve expressing the measured detector signal as a weighted sum of all its monochromatic components, taking into account the source spectrum and the detector's energy response. Therefore, as long as there is no significant beam hardening by the sample, Eq. 5.15 can also be applied to data acquired with a polychromatic beam, if the input values for δ and β are calculated at their effective energies [76].

5.3 Quantitative validation

The novelty of the proposed algorithm lies in its ability to enable the imaging of samples containing materials with significantly different refractive index properties. In order to test its validity, a simulation study was performed, followed by the acquisition of experimental data for direct comparison. As a test sample, a water filled cylinder containing aluminium and low-density polyethylene (LDPE) rods was chosen.

Vittoria's wave-optics simulation code [106] (introduced previously in chapter 4), was used to generate the simulated data, with a photon energy of $E = 17.5$ keV. A numerical phantom was created, which consisted of a vertically-aligned cylinder of water (diameter = 1.85 cm) containing an aluminium rod (diameter = 2 mm) and an LDPE rod (diameter = 3.9 mm). Corresponding refractive index values were taken from the ICRU 44 database [4] and are reported in table 5.1.

Table 5.1: Input refractive index values used for the simulated phantom.

Material	$\boldsymbol{\delta}$	$\boldsymbol{\mu}$ **(1/cm)**
Water	$7.5E-7$	1.1
Aluminium	$1.8E-6$	13.7
LDPE	$7.1E-7$	0.5

Mask parameters were chosen to match those used in the laboratory, where each mask is 150 μm thick and made of gold. The masks' periods and aperture sizes were 48 μm and 12 μm, respectively, for the sample-mask, and 62 μm and 15 μm for the detector-mask. The masks' apertures were aligned with the vertical (y) direction. The detector pixel size was 62 $\times$ 62 μm^2. The source-to-sample distance was $z_{so} = 1.6$ m and the sample-to-detector distance was $z_{od} = 0.4$ m. For simplicity, in the simulation it was assumed that there was no gap between the

sample-mask and sample, and similarly no gap between the detector-mask and detector; in practice, a small (∼1-2 cm) gap was present, however it is not expected to have any noticeable effect on the images. An IC was simulated to obtain $C(x_e)$ and $C'(x_e)$. A CT scan was then simulated, consisting of 2400 views over 360 degrees (i.e. angular step = 0.15 degrees). The relative displacement of the sample-mask with respect to the detector-mask was set as $x_e = 10$ μm. Dithering was used to increase the spatial sampling rate; at each angular view, 4 images were taken at different sub-pixel positions of the sample and recombined to form a high-resolution image. Dithering however is not required unless an increase in spatial resolution over that determined by the detector pixel size is sought [86]. The phase retrieval part comprised of three steps. First, Eq. 5.4 was applied to the unprocessed projections using the refractive index values of water. The second and third steps consisted of applying Eq. 5.15 to unprocessed projections, once for the water-aluminium interface, and then for the water-LDPE interface, using the values listed in table 5.1. $A(x, y)$ was calculated as the projection of a circle with a diameter corresponding to that of the water cylinder. Three separate sinograms were created, corresponding to the different retrieval steps. CT slices of each of these phase-retrieved sinograms were then reconstructed by means of a FBP algorithm (and were later spliced, see below).

For experimental validation, a phantom was created which matched the simulated one (apart from the fact that a hollow plastic cylinder of unknown material, with inner and external diameters of 1.75 cm and 1.85 cm, respectively, was filled with water for practical reasons). As a source, the Rigaku MicroMax 007 HF rotating anode (molybdenum) X-ray tube (Rigaku Corporation, Japan) with a

focal spot of approximately 70 μm was used. The source was operated at 25 mA and 40 kVp, with a 30 μm Molybdenum filter. A Pixirad single photon counting, energy-resolving detector [71, 72], with a pixel size of 62×62 μm^2 was used and placed 2.07 m away from the source.

The sample and detector masks were placed at 1.6 m and 1.97 m downstream of the source, respectively. Both masks were fabricated by electroplating gold strips onto a graphite substrate (Creatv Microtech Inc., Potomac, MD, USA). The masks' period and aperture sizes were the same as used in the simulation, apart from the period of the detector-mask which was 59 μm, to compensate for the limited magnification arising from the small gap between the detector-mask and the detector.

An IC scan was performed, followed by a CT scan of the phantom with the same parameters reported for the simulation. Flat-field images were acquired at each angular view, and were later used to normalize the sample images. The exposure time per projection was 4 s.

For phase retrieval, Eqs. 5.4 and 5.15 were applied to the normalized data. Here, since the source spectrum is polychromatic and the complex refractive index varies with energy, the refractive index values used in the retrieval were estimated. In general, these can be estimated using the concept of effective energies if the source spectrum, detector energy response and sample composition and geometry are known [76].

In the case discussed in this chapter, one can consider that an optimal CT reconstruction has been achieved when two conditions are satisfied. The first one is the maximization of the sharpness of the interface between the pair of materials of interest. The second is that the reconstructed material j has a mean value of

1 in the CT slice. In order to simultaneously fulfill these conditions, CT reconstruction is carried out multiple times while varying the refractive index values. The chosen values used in the retrieval algorithm of the experimental data are presented in table 5.2, along with the effective energies these correspond to for each material. These effective energies are reasonable considering the source spectrum produced by the molybdenum target. The difference between the values obtained for water and LDPE compared to aluminium can be explained by taking into account the beam hardening caused by the higher absorption of the aluminium rod. Phase retrieved sinograms were created, followed by a CT reconstruction using FBP.

Table 5.2: Refractive index values used for the retrieval of the experimental phantom images.

Material	$\boldsymbol{\delta}$	$\boldsymbol{E_{ef,\delta}}$ **(keV)**	$\boldsymbol{\mu}$ $\boldsymbol{(1/cm)}$	$\boldsymbol{E_{ef,\mu}}$ **(keV)**
Water	$7.6E-7$	17.5	0.76	20.5
Aluminium	$9.5E-7$	24	5.5	24
LDPE	$7.1E-7$	17.5	0.48	18

For a quantitative evaluation of the proposed algorithm, simulated and experimentally retrieved projected thicknesses of each material were plotted against each other and are shown in Fig. 5.2.

The plots demonstrate the quantitativeness of the algorithm: all simulated profiles retrieve the nominal thickness values accurately (retrieving diameters of 1.85 cm, 2 mm and 3.9 mm for water, aluminium and LDPE, respectively). As expected, in each case the profiles are quantitative only for the interface between the two materials targeted by the algorithm through selection of the relative input parameters. A good agreement can also be noted between the experimental and simulated profiles for each material of interest. Discrepancies in e.g. the re-

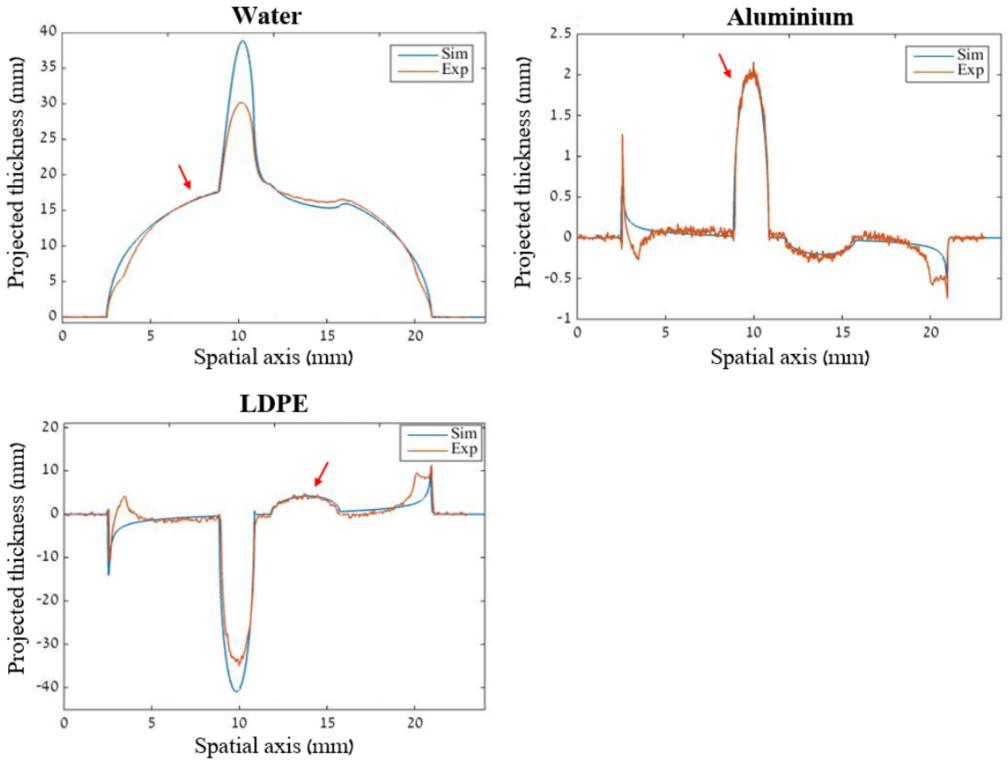

Figure 5.2: Retrieved projected thicknesses for water, aluminium and LDPE, using values reported in tables 5.1 and 5.2. The red arrows point at the material of interest in each case. The experimental profiles were averaged over 5 pixel rows.

trieved thickness of water, in the location where the aluminium rod is positioned, arise from the difference in (effective) energies between the monochromatic simulation and the experimental polychromatic spectrum. Another inconsistency in retrieved values can be observed between simulated and experimental profiles of both aluminium and LDPE, just near the edges of the cylinder. This inconsistency arises from the fact that, while a water cylinder was implemented in the simulation, the experimental phantom consisted of a plastic cylinder filled with water. Finally, by looking at the retrieved projected thickness of both aluminium and LDPE, it can be seen that the algorithm breaks down at the edges of the outer cylinder; this can be expected since in that case the assumption of a slowly

varying thickness of the encasing material is violated. However, this affects the retrieved values only locally, at the edges of the encasing material, and values at the interface of interest are not compromised.

In order to present all interfaces correctly in a single CT slice, the three different slices were spliced together. This step was performed using the open source software ImageJ, for both the experimental and simulated slices. While the segmentation part of the splicing procedure could be automated using methods such as Otsu thresholding [99, 114] or by developing expressions for the "bleed-width" in a similar fashion to Beltran's work [97], for this proof-of-concept study the segmentation was done manually, by visually estimating the blurring bleed-width.

Individual simulated CT slices, each displaying reconstructions of the water-air (a), aluminium-water (b) and LDPE-water (c) interfaces are shown in Fig. 5.3, along with the simulated and experimental spliced slices. Each slice in panels (a-c) demonstrates a sharp reconstruction of the material pair of interest, while residual phase-contrast fringes and blurred interfaces of other materials are highlighted by arrows.

In order to achieve a quantitative spliced slice preserving the δ values used in the retrieval across the entire phantom, each slice reconstructed from t_j had to be manipulated according to: $slice^*_{t_j} = [slice_{t_j} \times (\delta_j - \delta_1)] + \delta_1$, before digitally inserting its segmented area of interest into the corresponding region of $slice^*_{t_1} = slice_{t_1} \times \delta_1$. The same splicing procedure was applied to both simulation and experimental slices, however, the δ values used for quantitative splicing were different. For each case, the δ values applied during splicing were the same as the ones previously used in the retrieval algorithm, hence some differences exist (most notably for aluminium, see tables 5.1 and 5.2). This can be appreciated in

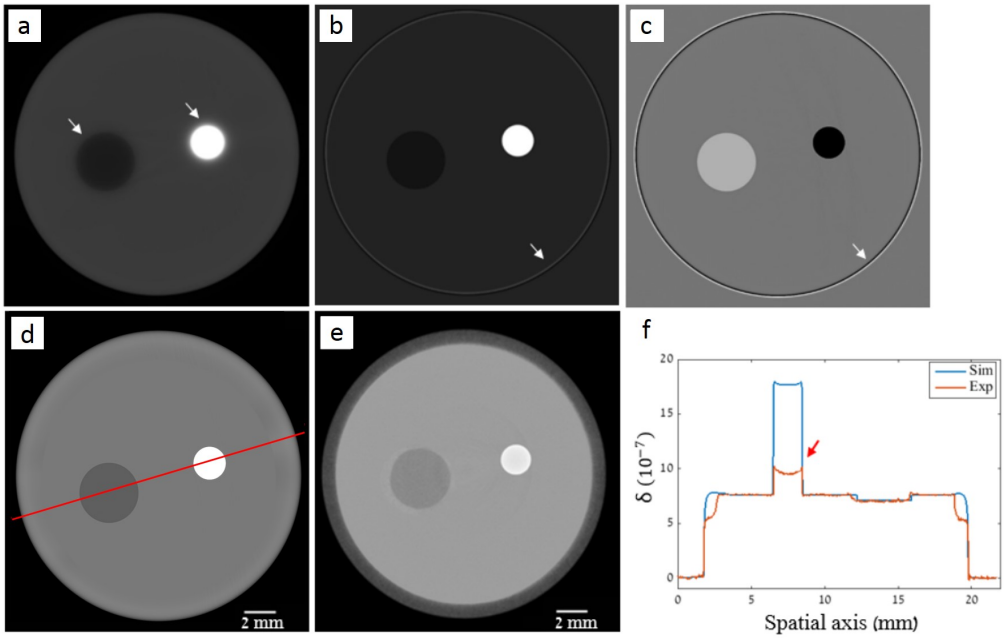

Figure 5.3: Simulated CT slices focusing on the water-air (a), aluminium-water (b) and LDPE-water (c) interfaces, using E=17.5 keV. The white arrows indicate artefacts arising from locally incorrect choices of refractive index values. Simulated (d) and experimental (e) spliced slices along with a plot of profiles through them (f), in the position indicated by the red line in (d). The difference in the retrieved values of the aluminium rod in (f, see arrow) is expected and is due to the difference in effective energies (see tables 5.1 and 5.2).

Fig. 5.3(f) where profiles across both spliced slices are plotted against each other for comparison. Ignoring the discrepancies which have already been discussed above (due to the plastic container and the polychromaticity of the spectrum, which also leads to a difference in the retrieved δ values for aluminium), both profiles demonstrate a sharp, quantitative reconstruction of all parts of the phantom. These results confirm that the algorithm is indeed quantitative for the case of monochromatic radiation, and can be applied when a polychromatic spectrum is used, if the concept of effective energies is employed [76].

5.4 Qualitative evaluation

Following validation by a phantom study, the proposed retrieval algorithm and splicing method were applied to experimental data of a complex biological sample. The imaged sample was a chicken bone surrounded by soft tissue, placed in a plastic cylinder of approximately 8 mm diameter. The sample was "fresh", i.e. no additional sample preparation was applied (e.g. formalin fixation). The same source used for the phantom scan was used, operated at 40 kVp and 25 mA, with no additional filters. The detector used for this scan was a Hamamatsu C9732DK flat panel detector with a passive-pixel CMOS sensor (Hamamatsu, Japan), and was positioned 2 m away from the source. The detector pixel size was $50 \times 50\ \mu m^2$, however the effective pixel size in the x-direction was $100\ \mu m$ due to the line-skipping design of the detector-mask, where every second detector pixel column is completely covered. This mask design is used to reduce the negative effect of pixel cross-talk on the EI signal [111]. The sample and detector masks were placed at 1.6 m and 1.96 m downstream of the source, respectively. The sample-mask period and aperture size were $79\ \mu m$ and $10\ \mu m$, respectively, while the detector-mask period was $98\ \mu m$ with a $17\ \mu m$ aperture size. Following an IC scan, a CT scan was performed with 720 views over 360 degrees (i.e. 0.5 degree step). To increase the spatial resolution through dithering, 8 projections were taken at different sub-pixel positions of the sample, at each angular view. The exposure time per projection was 3 s and the relative position of the sample-mask with respect to the detector-mask was set as $x_e = 8\ \mu m$.

Raw projections were corrected for dark current and flat-field inhomogeneities prior to the phase retrieval step, which used Eq. 5.4 once (for the cylinder-air

interface) and Eq. 5.15 twice (where the interfaces between soft tissue types, e.g. fat-muscle, and between soft tissue and bone were considered). For the retrieval of the bone-soft tissue interface, refractive index values of bone and water (which is commonly used as a tissue-equivalent material) at an *estimated* effective energy of 22 keV were used [4]. Here, the effective energy was estimated according to the theoretical source spectrum and a predicted linear detector energy response, since the detector used in this setup was an integrating detector with an energy response function which has yet to be fully characterized (unlike in the phantom scan reported in section 5.3, where a photon-counting detector was employed). Moreover, since the specific tissue types were not known and the complex sample geometry in this case did not strictly satisfy the algorithm's condition for a material fully encased by another, a purely qualitative evaluation was performed for the retrieval of the interface between soft tissue types. In practice, an iterative approach was employed, where $\Delta\mu$ and γ were varied until the contrast between the different soft tissues, was maximized.

The reconstructed slices are shown in Fig. 5.4. On the left hand side, three separate reconstructions are shown, each rendering a specific interface while exhibiting the expected blurring\fringes at other interfaces. A spliced, composite CT slice is presented in the larger image on the right, in which all different materials are adequately reconstructed.

As previously noted, although the algorithm was derived for the case of a material j fully encased within material 1, this is not strictly the case for the chicken bone sample. However, as already observed by Beltran, a locally incorrect choice of refractive index values will only affect the part of the interface for which the choice is not ideal [97]. Since quantitative results were not expected, the composite slice

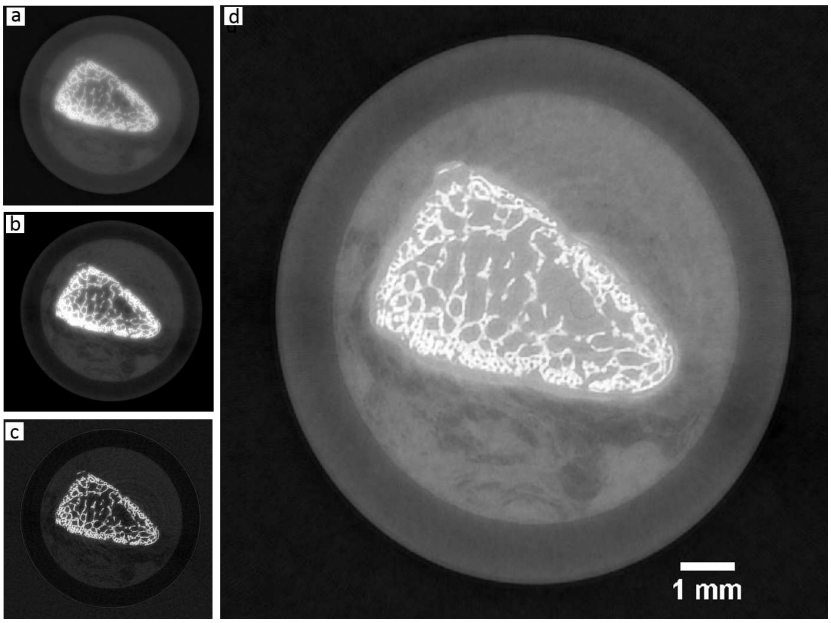

Figure 5.4: Axial slices of a chicken bone sample reconstructed using values optimized for the cylinder-air interface (a), contrast between soft-tissue types (b) and bone-soft tissue interface (c). Panel (d) shows a composite slice obtained by splicing slices (a-c).

was created by windowing each retrieved slice differently, in order to achieve the best visualization. As before, the splicing procedure was performed using ImageJ and manual segmentation. The spliced image shown in Fig. 5.4(d) demonstrates that this method could be used to obtain high-quality, albeit not quantitative, images of complex samples with unknown composition, using a single image per projection.

5.5 Discussion and conclusion

An algorithm capable of quantitatively retrieving the projected thickness of multi-material samples illuminated by monochromatic radiation, using a single input image acquired with an EI setup, has been presented. A CT phantom simulation

study was used to validate the algorithm's accuracy, while results from an experimental scan provided good agreement, within the limits of polychromaticity. A "splicing" method was then presented as a means for producing a composite CT slice where all parts of a sample are adequately reconstructed, thereby eliminating artefacts previously arising from locally incorrect choices of refractive index values for multi-material samples, during the phase retrieval step.

For strictly quantitative results, one material must be fully encased by the other, and the refractive indices of both materials and the total projected thickness must be known. Therefore, for quantitative imaging, certain applications (e.g. in the field of materials science) could benefit from using the proposed method on data acquired using monochromatic radiation. However, the work presented here has shown that enhanced image quality and visualization can be achieved for complex samples of unknown materials, also when imaged with a polychromatic beam produced by a laboratory source.

It should be noted that, if the requirement for quantitativeness is relinquished and when splicing is used, similar results can be obtained by using Eq. 5.4 multiple times, and replacing δ and μ with $\Delta\delta = \delta_j - \delta_1$ and $\Delta\mu = \mu_j - \mu_1$. This approach might be more practical since it does not require the total projected thickness as input; however, the retrieved projected thickness profiles will not be quantitative as they are not "normalized" by the encasing material. Nevertheless, during the splicing step, the CT slices are scaled and can be windowed to achieve similar results to those obtained by using Eq. 5.15.

The EI single-image retrieval algorithm recently developed by Diemoz has shown great potential for reducing scan times, particularly for CT scans, by simplifying the acquisition sequence [89]. Previously, different retrieval algorithms required

the position of the sample-mask to be varied at least once per projection, leading to increased scan times as well as potentially introducing instabilities to the imaging system. In this proof-of-principle study, dithering was performed in both reported scans, meaning that multiple images of the sample at different sub-pixel positions were acquired at each view, thereby increasing the delivered dose and scan duration. However, dithering is not strictly necessary and is only used to increase the spatial resolution, as previous studies have shown that quantitative information can be extracted from EI CT also when no dithering is performed [86]. Although not exploited in this study, when dithering is not required, single-image retrieval enables a continuous rotation of the sample, which can lead to significantly reduced scan times, as was recently reported [89]. It is therefore expected that the development presented in this chapter will enable obtaining similar results for complex samples containing materials with a wide range of refractive index values, thereby making EI CT suitable for a wider range of applications. Furthermore, since the algorithm requires only one input image as opposed to the previously needed minimum of two [73], future work should focus on investigating its potential for dose reduction strategies.

Conclusions

XPCi techniques have the potential to revolutionize the field of X-ray imaging, thanks to the increase in image contrast they provide when compared to attenuation-based imaging. Currently, the main obstacle preventing XPCi from becoming a commonly used imaging tool is the need for specialized setups, often requiring highly coherent X-ray sources. The EI method however does not rely on spatial coherence, and can be implemented with conventional X-ray source and detector equipment. It therefore shows great potential for translation into clinical and industrial environments, an essential step in making XPCi a widespread imaging technique in a range of fields.

The work presented in this thesis aimed to explore further developments of the EI method, and specifically its CT modality, in order to increase the range of applications which could benefit from its various advantages. First, the underlying principles of attenuation-based X-ray imaging were presented, along with the theoretical background to CT reconstruction. The concept of XPCi was then introduced, followed by a review of the most prominent XPCi techniques. The working principles of each technique were presented, and their advantages and limitations were discussed. Particular focus was given to the EI method and its adaptation to a CT modality, and the previous literature specifically dedicated

to this method was reviewed.

Prior to the work presented in this thesis, the entirety of EI CT research comprised of demonstrating that EI CT is feasible, and can be performed at both synchrotrons and laboratories. It was therefore necessary to carry out studies aimed at optimizing both the acquisition strategy and the processing of EI CT data, such that it could be used for a wide range of applications, which typically have different requirements with regards to dose, speed and spatial resolution.

In the first study described in this thesis, a new application which could potentially benefit from EI CT has been identified: perinatal post-mortem imaging. As perinatal autopsy rates continue to fall for a variety of reasons, the use of non-invasive imaging as an alternative is being investigated, using a range of imaging techniques. In light of the high spatial-resolution and soft-tissue sensitivity provided by XPCi methods, this study aimed to demonstrate the feasibility of using XPCi tomography for this purpose. In this proof-of-principle study, a new-born piglet was scanned at a synchrotron using a FSP setup. The reconstructed phase slices were assessed for diagnostic quality by a radiologist, and were determined to be clinically satisfactory, as they presented high soft-tissue contrast and sufficient resolution for resolving organ structure. Furthermore, all key organs for the purpose of a post-mortem examination (heart, lungs, kidneys, liver and intestines) were easily identified and adequately visualized. The study therefore provided evidence that XPCi could be used for the purpose of whole body post-mortem imaging. However, to make XPCi CT a practical alternative to perinatal autopsy, further developments are required in order to translate this application to a clinical environment. As a first step, the experiment should be

repeated with an animal model using the laboratory implementation of EI. Upon obtaining successful results in the laboratory, the next step would be to scan human foetal tissue, and make a direct comparison to data obtained with conventional imaging techniques (CT and MRI). The lab-based EI CT system thus needs to be further optimized for human use, particularly smaller foetuses, before being introduced into clinical practice. New data acquisition strategies and phase retrieval approaches, such as the "local" and "single-image" retrieval algorithms presented in this thesis, are essential steps in achieving this goal.

In the second study presented here, a "local" retrieval algorithm was developed, which enables to obtain high-quality EI CT images from high-resolution, multimodal lab-based scans. The ability of the EI method to provide multiple contrast channels (absorption, phase, scatter) is one of its greatest advantages, as complementary information from such images can be useful in many applications. However, instabilities of the imaging system during the scan or imperfections in the optical elements and their alignment can introduce errors during data processing. Such errors can lead to poor image quality in the phase slices, which often suffer from artefacts.

In order to improve image quality and reduce image artefacts in long lab-based scans, possible sources of noise and error were first modeled in a simulation study, and their effect on the reconstructed phase slices was analyzed. Four sources of error were considered ((1) masks/detector imperfections, (2) flat-field normalization, (3) intensity changes between dithering steps, (4) correlated shot noise), the combination of which was shown to result in a similar noise structure to the one observed in experimental data.

After the main sources of noise and image artefacts were identified, a new retrieval algorithm was developed, the "modified local" algorithm. This algorithm is a further development of a previous one capable of retrieving the absorption, refraction and scatter information of a sample in cases where the imaging system is misaligned. The modified local algorithm was developed specifically for high-resolution, multi-modal CT scans in non-ideal environments. Such scans can last hours, during which system parameters can vary due to environmental changes. Variations in system parameters (both over time, as well as local variations over the FOV) which are not taken into account during data reconstruction can introduce errors which severely degrade the reconstructed phase slices.

Specifically, it was shown that there is a significant lateral shift in the position of the IC over time. As a first step to compensate for these shifts, a real-time illumination tracking procedure was implemented into the CT scan. Then, the algorithm was modified to include a correction term for the shift of the IC between dithering steps images. Simulated data was used to quantitatively validate the algorithm's performance in the case of system misalignment, while a qualitative evaluation was performed using experimentally acquired data of a complex biological sample. The algorithm's performance was evaluated in comparison to a previously used "global" retrieval algorithm, and was shown to result in the removal of all major artefacts, leading to a significant improvement in image quality. Furthermore, the algorithm is applied on a pixel-by-pixel basis, and does not require the acquisition of any flat-field images. Its use is therefore expected to enable the acquisition of high-resolution, reliable CT data of large samples in realistic settings.

For many applications, in particular in the biomedical field, the ability to obtain high-quality CT data from fast scans can be more important than the retrieval of multiple contrast channels. Furthermore, depending on the sample, the spatial-resolution given by the de-magnified detector pixel size might be sufficient, in which case dithering is not required. In the last study presented in this thesis, the "multi-material, single-image" algorithm was developed, as means to perform scans of this type. This algorithm requires a single image per projection, as opposed to the conventional EI retrieval algorithms which require the acquisition of multiple ones while the position of the sample-mask is varied. The multi-material, single-image algorithm was developed as an extension to a previous single-image algorithm, with the aim of overcoming the latter's main limitation, i.e. the assumption of a homogeneous sample. Such a development is essential for biomedical applications, as it will enable the performance of fast EI CT scans on samples containing materials with significantly different refractive index values, such as soft-tissue and bone. Notably, it has the potential to make small-animal imaging possible, including in-vivo applications.

The theoretical derivation of the algorithm was presented, and its capability to quantitatively retrieve the projected thickness of multi-material samples illuminated by monochromatic radiation was demonstrated. Using simulated and real versions of the same phantom, the algorithm's quantitativeness was validated from both simulated and experimental data, the latter showing good agreement within the limits of polychromaticity. To eliminate image artefacts related to locally incorrect choices of refractive index values during the phase retrieval step, a splicing method was described for obtaining a composite CT slice where all parts of a sample are adequately reconstructed. Furthermore, the algorithm's ability

to provide high-quality, albeit not quantitative, CT slices of complex samples was demonstrated by applying it to experimental data of a biological sample containing both bone and soft-tissue.

Although this proof-of-principle study involved the use of dithering, many applications might not require the increase in spatial resolution provided by the dithering procedure. Such applications can benefit the most from this algorithm, as the sample can be continuously rotated over 180 degrees, and scan times substantially reduced as a consequence. It is therefore expected that by using the multi-material, single-image algorithm, high-quality CT reconstructions of complex samples will be obtained from fast scans performed in a laboratory setting. In the future, the algorithm's potential for dose reduction should be investigated, through comparison with the dose requirements of EI algorithms requiring multiple images per projection.

References

[1] A. Kak and M. Slaney. *Principles of Computerized Tomographic Imaging*. Society for Industrial and Applied Mathematics USA, 1987. 12, 29, 37, 38, 39, 40

[2] M. B. Szafraniec, T. P. Millard, K. Ignatyev, R. D. Speller, and A. Olivo. **Proof-of-concept demonstration of edge-illumination x-ray phase contrast imaging combined with tomosynthesis**. *Phys. Med. Biol.*, **59**(5):N1–N10, 2014. 13, 60

[3] M. Endrizzi, P. C. Diemoz, T. P. Millard, J. Louise Jones, R. D. Speller, I. K. Robinson, and A. Olivo. **Hard X-ray dark-field imaging with incoherent sample illumination**. *Appl. Phys. Lett.*, **104**(2):024106, 2014. 17, 26, 64, 107, 109, 110

[4] **Tissue Substitutes in Radiation Dosimetry and Measurement, ICRU report 44**. Technical report, International Commission on Radiation Units and Measurements, 1989. 20, 76, 92, 136, 144

[5] A. Haase, G. Landwehr, and E. Umbach. *Röntgen Centennial: X-Rays in Natural and Life Sciences*. World Scientific Publishing Company, 1997. 23, 32, 35

[6] S. W. Wilkins, Ya. I. Nesterets, T. E. Gureyev, S. C. Mayo, A. Pogany, and A. W. Stevenson. **On the evolution and relative merits of hard X-ray phase-contrast imaging methods**. *Phil. Trans. R. Soc.*, **372**:20130021, 2014. 25, 43, 46

[7] A. Olivo and E. Castelli. **X-ray phase contrast imaging: From synchrotrons to conventional sources**. *Riv. Del Nuovo Cim.*, **37**(9):467–508, 2014. 25, 46, 55

[8] A. Bravin, P. Coan, and P. Suortti. **X-ray phase-contrast imaging: from pre-clinical applications towards clinics.** *Phys. Med. Biol.*, **58**(1):R1–35, 2013. 25, 46

[9] A. Olivo, F. Arfelli, G. Cantatore, R. Longo, R. H. Menk, S. Pani, M. Prest, P. Poropat, L. Rigon, G. Tromba, E. Vallazza, and E. Castelli. **An innovative digital imaging set-up allowing a low-dose approach to phase contrast applications in the medical field**. *Med. Phys.*, **28**(8):1610, 2001. 25, 45, 57

[10] M. Endrizzi, F. A. Vittoria, G. Kallon, D. Basta, P. C. Diemoz, A. Vincenzi, P. Delogu, R. Bellazzini, and A. Olivo. **Achromatic approach to phase-based multi-modal imaging with conventional X-ray sources**. *Opt. Express*, **23**(12):16473, 2015. 25, 59

[11] A. Olivo and R. Speller. **Modelling of a novel x-ray phase contrast imaging technique based on coded apertures.** *Phys. Med. Biol.*, **52**(22):6555–73, 2007. 25, 59

[12] A. Olivo, K. Ignatyev, P.R.T. Munro, and R.D. Speller. **Design and realization of a coded-aperture based X-ray phase contrast imaging for**

homeland security applications. *Nucl. Instruments Methods Phys. Res. Sect. A*, **610**(2):604–614, 2009. 26

[13] P. C. Diemoz, M. Endrizzi, C. E. Zapata, A. Bravin, R. D. Speller, I. K. Robinson, and A. Olivo. **Improved sensitivity at synchrotrons using edge illumination X-ray phase-contrast imaging**. *J. Instrum.*, **8**:C06002, 2013. 26

[14] C. K. Hagen, P. Maghsoudlou, G. Totonelli, P. C. Diemoz, M. Endrizzi, L. Rigon, R.-H. Menk, F. Arfelli, D. Dreossi, E. Brun, P. Coan, A. Bravin, P. De Coppi, and A. Olivo. **High contrast microstructural visualization of natural acellular matrices by means of phase-based x-ray tomography.** *Sci. Rep.*, **5**:18156, 2015. 26, 57, 68, 84, 87

[15] M. Endrizzi, B. I. S. Murat, P. Fromme, and A. Olivo. **Edge-illumination X-ray dark-field imaging for visualising defects in composite structures**. *Compos. Struct.*, **134**:895–899, 2015. 26

[16] A. Olivo, S. Gkoumas, M. Endrizzi, C. K. Hagen, M. B. Szafraniec, P. C. Diemoz, P. R. T. Munro, K. Ignatyev, B. Johnson, J. A. Horrocks, S. J. Vinnicombe, J. L. Jones, and R. D. Speller. **Low-dose phase contrast mammography with conventional x-ray sources.** *Med. Phys.*, **40**(9):090701, 2013. 26

[17] P. Diemoz, F. Vittoria, and A. Olivo. **Spatial resolution of edge illumination X-ray phase-contrast imaging.** *Opt. Express*, **22**(13):15514–15529, 2014. 26, 59, 107, 129

[18] C. K. Hagen, P. C. Diemoz, M. Endrizzi, L. Rigon, D. Dreossi, F. Arfelli, F. C. M. Lopez, R. Longo, and A. Olivo. **Theory and preliminary**

experimental verification of quantitative edge illumination x-ray phase contrast tomography. *Opt. Express*, **22**(7):7989–8000, 2014. 26, 65, 67, 87

[19] T. S. Curry, J. E. Dowrdey, and R. C. Murry. *Christensen's Physics of Diagnostic Radiology*. Lea & Febiger, fourth edition, 1990. 29, 32

[20] S. Webb. *Webb's Physics of Medical Imaging*. CRC Press, New-York, second edition, 2012. 29, 32, 34

[21] J. Als-Nielsen and D. McMorrow. *Elements of Modern X-ray Physics*. Wiley, second edition, 2011. 29, 30

[22] D. M. Paganin. *Coherent X-ray Optics*. Oxford University Press, 2006. 33, 42, 43

[23] S. Dixon. **Diagnostic Imaging Dataset Annual Statistical Release 2015/16**. Technical report, Operational Information for Commissioning, NHS England, 2016. 35

[24] L. A. Feldkamp, L. C. Davis, and J. W. Kress. **Practical cone-beam algorithm**. *J. Opt. Soc. Am. A*, **1**(6):612–619, 1984. 40

[25] H. K. Tuy. **An Inversion Formula for Cone-Beam Reconstruction**. *SIAM J. Appl. Math.*, **43**(3):546–552, 1983. 40

[26] C. C. Shaw. *Cone Beam Computed Tomography*. Taylor & Francis, 2014. 40

[27] Wilkins, S. W. and Gureyev, T. E. and Gao, D. and Pogany, A. and Stevenson, A. W. **Phase-contrast imaging using polychromatic hard X-rays**. *Nature*, **384**:335–338, 1996. 44, 53, 54, 55, 83

[28] U. Bonse and M. Hart. **an X-Ray Interferometer**. *Appl. Phys. Lett.*, **6**(8):155–156, 1965. 45, 46

[29] T. J. Davis, D. Gao, T. E. Gureyev, A. W. Stevenson, and S. W. Wilkins. **Phase-contrast imaging of weakly absorbing materials using hard X-rays**. *Nature*, **373**:595–598, 1995. 45, 48

[30] A. Snigirev, I. Snigireva, V. Kohn, S. Kuznetsov, and I. Schelokov. **On the possibilities of x-ray phase contrast microimaging by coherent high-energy synchrotron radiation**. *Rev. Sci. Instrum.*, **66**(12):5486, 1995. 45, 53, 54

[31] A. Momose, S. Kawamoto, I. Koyama, Y. Hamaishi, K. Takai, and Y. Suzuki. **Demonstration of X-Ray Talbot Interferometry**. *Jpn. J. Appl. Phys.*, **42**:L866–L868, 2003. 45, 51

[32] F. Pfeiffer, T. Weitkamp, O. Bunk, and C. David. **Phase retrieval and differential phase-contrast imaging with low-brilliance X-ray sources**. *Nat. Phys.*, **2**(4):258–261, 2006. 45, 52, 83

[33] A. Olivo and R. Speller. **A coded-aperture technique allowing x-ray phase contrast imaging with conventional sources**. *Appl. Phys. Lett.*, **91**(7):074106, 2007. 45, 58, 83

[34] A. Momose and J. Fukuda. **Phase-contrast radiographs of nonstained rat cerebellar specimen**. *Med. Phys.*, **22**(4):375–379, 1995. 47, 48

[35] M. Takeda, H. Ina, and S. Kobayashi. **Fourier-transform method of fringe-pattern analysis for computer-based topography and interferometry**. *J. Opt. Soc. Am.*, **72**(1):156–160, 1982. 48

[36] H. Wen, A. Gomella, A. Patel, S. Lynch, N. Morgan, S. Anderson, E. Bennett, X. Xiao, C. Liu, and D. Wolfe. **Subnanoradian X-ray**

phase-contrast imaging using a far-field interferometer of nanometric phase gratings. *Nat. Commun.*, **4**:2659, 2013. 48

[37] V. N. Ingal and E. A. Beliaevskaya. **X-ray plane-wave topography observation of the phase contrast from a non-crystalline object**. *J. Phys. D. Appl. Phys.*, **28**(11):2314–2317, 1995. 48

[38] F. Arfelli, V. Bonvicini, A. Bravin, G. Cantatore, E. Castelli, L. Palma, M. Michiel, M. Fabrizioli, R. Longo, R. Menk, A. Olivo, S. Pani, D. Pontoni, P. Poropat, M. Prest, A. Rashevsky, M. Ratti, L. Rigon, G. Tromba, A. Vacchi, E. Vallazza, and F. Zanconati. **Mammography with Synchrotron Radiation: Phase-Detection Techniques**. *Radiology*, **215**(111):286–293, 2000. 49

[39] Chapman, D. and Thomlinson, W. and Johnston, R. E. and Washburn, D. and Pisano, E. and Gmur, N. and Zhong, Z. and Menk, R. and Arfelli, F. and Sayers, D. **Diffraction enhanced x-ray imaging**. *Phys. Med. Biol.*, **42**:2015–2025, 1997. 50, 62

[40] P. Diemoz, P. Coan, C. Glaser, and A. Bravin. **Absorption, refraction and scattering in analyzer-based imaging: comparison of different algorithms.** *Opt. Express*, **18**(4):3494–3509, 2010. 50

[41] D. Chapman, I. Nesch, M. O. Hasnah, and T. I. Morrison. **X-ray optics for emission line X-ray source diffraction enhanced systems**. *Nucl. Instruments Methods Phys. Res. A*, **562**:461–467, 2006. 50

[42] I. Nesch, D. P. Fogarty, T. Tzvetkov, B. Reinhart, A. C. Walus, G. Khelashvili, C. Muehleman, and D. Chapman. **The design and ap-**

plication of an in-laboratory diffraction-enhanced x-ray imaging instrument. *Rev. Sci. Instrum.*, **80**:093702, 2009. 50

[43] P. Cloetens, J. Guigay, C. Martinoa, M. Saomé, M. Schenker, and D. Dyck. **Quantitative aspects of coherent hard X-ray imaging : Talbot images and holographic reconstruction**. *Optical Science, Engineering and Instrumentation*, **3154**:72–82, 1997. 51

[44] P. Cloetens, J. P. Guigay, C. De Martino, J. Baruchel, and M. Schlenker. **Fractional Talbot imaging of phase gratings with hard x rays**. *Opt. Lett.*, **22**(14):1059, 1997. 51

[45] C. David, B. Nohammer, H. H. Solak, and E. Ziegler. **Differential x-ray phase contrast imaging using a shearing interferometer**. *Appl. Phys. Lett.*, **81**(17):3287, 2002. 51

[46] T. Weitkamp, A. Diaz, C. David, F. Pfeiffer, M. Stampanoni, P. Cloetens, and E. Ziegler. **X-ray phase imaging with a grating interferometer**. *Opt. Express*, **13**(16):6296–6304, 2005. 51, 52

[47] C. David, J. Bruder, T. Rohbeck, C. Grünzweig, C. Kottler, a. Diaz, O. Bunk, and F. Pfeiffer. **Fabrication of diffraction gratings for hard X-ray phase contrast imaging**. *Microelectron. Eng.*, **84**:1172–1177, 2007. 52

[48] F. Pfeiffer, J. Herzen, M. Willner, M. Chabior, S. Auweter, M. Reiser, and F. Bamberg. **Grating-based X-ray phase contrast for biomedical imaging applications.** *Z. Med. Phys.*, **23**(3):176–185, 2013. 53

[49] P. Cloetens, R. Barrett, J. Baruchel, J. Guigay, and M. Schlenker. **Phase objects in synchrotron radiation hard x-ray imaging**. *J. Phys. D. Appl. Phys.*, **29**(1):133–146, 1996. 53

[50] A. Peterzol, A. Olivo, L. Rigon, S. Pani, and D. Dreossi. **The effects of the imaging system on the validity limits of the ray-optical approach to phase contrast imaging**. *Med. Phys.*, **32**(12):3617–3627, 2005. 53

[51] O. Hemberg, M. Otendal, and H. M. Hertz. **Liquid-metal-jet anode electron-impact x-ray source**. *Appl. Phys. Lett.*, **83**(7):1483–1485, 2003. 54

[52] M. Töpperwien, M. Krenkel, D. Vincenz, F. Stöber, A. M. Oelschlegel, J. Goldschmidt, and T. Salditt. **Three-dimensional mouse brain cytoarchitecture revealed by laboratory-based x-ray phase-contrast tomography**. *Sci. Rep.*, **7**:42847, 2017. 54

[53] A. Pogany, D. Gao, and S. W. Wilkins. **Contrast and resolution in imaging with a microfocus x-ray source**. *Rev. Sci. Instrum.*, **68**(7):2774, 1997. 55

[54] M. Reed Teague. **Deterministic phase retrieval: a Green's function solution**. *J. Opt. Soc. Am.*, **73**(11):1434, 1983. 55, 129

[55] P. Cloetens, W. Ludwig, J. Baruchel, D. Van Dyck, J. Van Landuyt, J. P. Guigay, and M. Schlenker. **Holotomography: Quantitative phase tomography with micrometer resolution using hard synchrotron radiation x rays**. *Appl. Phys. Lett.*, **75**(19):2912, 1999. 55

[56] D Paganin, S C Mayo, T E Gureyev, P R Miller, and S W Wilkins. **Simultaneous phase and amplitude extraction from a single defocused image of a homogeneous object.** *J. Microsc.*, **206**:33–40, 2002. 55, 56, 74, 127

[57] S. Sanchez, P. E. Ahlberg, K. M. Trinajstic, A. Mirone, and P. Tafforeau. **Three-dimensional synchrotron virtual paleohistology:**

a new insight into the world of fossil bone microstructures. *Microsc. Microanal.*, **18**:1095–1105, 2012. 57

[58] D. Rousseau, T. Widiez, S. Di Tommaso, H. Rositi, J. Adrien, E. Maire, M. Langer, C. Olivier, F. Peyrin, and P. Rogowsky. **Fast virtual histology using X-ray in-line phase tomography: application to the 3D anatomy of maize developing seeds**. *Plant Methods*, **11**(1):55, 2015. 57

[59] A. Bronnikov. **Theory of quantitative phase-contrast computed tomography**. *J. Opt. Soc. Am. A*, **19**(3):472, 2002. 57

[60] A. Groso, M. Stampanoni, R. Abela, P. Schneider, S. Linga, and R. Muller. **Phase contrast tomography: An alternative approach**. *Appl. Phys. Lett.*, **88**(21):214104, 2006. 57

[61] T. E. Gureyev, D. M. Paganin, G. R. Myers, Ya. I. Nesterets, and S. W. Wilkins. **Phase-and-amplitude computer tomography**. *Appl. Phys. Lett.*, **89**(3):034102, 2006. 57

[62] T. E. Gureyev, S. C. Mayo, D. E. Myers, Ya. Nesterets, D. M. Paganin, A. Pogany, a. W. Stevenson, and S. W. Wilkins. **Refracting Rontgen's rays: Propagation-based x-ray phase contrast for biomedical imaging**. *J. Appl. Phys.*, **105**(10):102005, 2009. 57

[63] M. Langer, P. Cloetens, J. Guigay, and F. Peyrin. **Quantitative comparison of direct phase retrieval algorithms in in-line phase tomography**. *Med. Phys.*, **35**(10):4556, 2008. 57

[64] Y. De Witte, M. Boone, J. Vlassenbroeck, M. Dierick, and L. Van Hoorebeke. **Bronnikov-aided correction for x-ray computed tomography**. *J. Opt. Soc. Am. A*, **26**(4):890–894, 2009. 57

[65] M. Boone, W. Devulder, M. Dierick, L. Brabant, E. Pauwels, and L. Van Hoorebeke. **Comparison of two single-image phase-retrieval algorithms for in-line x-ray phase-contrast imaging.** *J. Opt. Soc. Am.*, **29**(12):2667–2672, 2012. 57

[66] P. Bidola, K. Morgan, M. Willner, A. Fehringer, S. Allner, F. Prade, F. Pfeiffer, and K. Achterhold. **Application of sensitive, high-resolution imaging at a commercial lab-based X-ray micro-CT system using propagation-based phase retrieval**. *J. Microsc.*, **266**(2):211–220, 2017. 57

[67] A. Olivo, K. Ignatyev, P.R.T. Munro, and R.D. Speller. **A coded-aperture based method allowing non-interferometric phase contrast imaging with incoherent X-ray sources**. *Nucl. Instruments Methods Phys. Res. A*, **648**:S28–S31, 2011. 59

[68] A. Astolfo, M. Endrizzi, B. Price, I. Haig, and A. Olivo. **The first large area, high x-ray energy phase contrast prototype for enhanced detection of threat object in baggage screening**. *SPIE Secur. Def.*, **999504**:999504, 2016. 59

[69] T. P. Millard, M. Endrizzi, K. Ignatyev, C. K. Hagen, P. R T Munro, R. D. Speller, and A. Olivo. **Method for automatization of the alignment of a laboratory based x-ray phase contrast edge illumination system**. *Rev. Sci. Instrum.*, **84**(8), 2013. 59

[70] G. K. Kallon, M. Wesolowski, F. A. Vittoria, M. Endrizzi, D. Basta, T. P. Millard, P. C. Diemoz, and A. Olivo. **A laboratory based edge-illumination x-ray phase-contrast imaging setup with two-directional sensitivity**. *Appl. Phys. Lett.*, **107**(20):103–108, 2015. 60

[71] R. Bellazzini, G. Spandre, A. Brez, M. Minuti, M. Pinchera, and P. Mozzo. **Chromatic X-ray imaging with a fine pitch CdTe sensor coupled to a large area photon counting pixel ASIC**. *J. Instrum.*, **8**(2):C02028, 2013. 61, 138

[72] M. Endrizzi, P. C. Diemoz, C. K. Hagen, F. A. Vittoria, P. R. T. Munro, L. Rigon, D. Dreossi, F. Arfelli, F. C. M. Lopez, R. Longo, M. Marenzana, P. Delogu, A. Vincenzi, L. De Ruvo, G. Spandre, A. Brez, R. Bellazzini, and A. Olivo. **Edge-illumination X-ray phase contrast imaging: matching the imaging method to the detector technology**. *J. Instrum.*, **9**(11):C11004, 2014. 61, 138

[73] P. R. T. Munro, K. Ignatyev, R. D. Speller, and a. Olivo. **Phase and absorption retrieval using incoherent X-ray sources**. *Proc. Natl. Acad. Sci.*, **109**(35):13922–13927, 2012. 61, 62, 87, 147

[74] P. C. Diemoz, M. Endrizzi, C. E. Zapata, Z. D. Pešić, C. Rau, a. Bravin, I. K. Robinson, and a. Olivo. **X-ray phase-contrast imaging with nanoradian angular resolution**. *Phys. Rev. Lett.*, **110**(13):138105, 2013. 61, 87

[75] P. Munro, C. Hagen, M. Szafraniec, and A. Olivo. **A simplified approach to quantitative coded aperture X-ray phase imaging.** *Opt. Express*, **21**(9):11187–201, 2013. 62, 63

[76] P. Munro and A. Olivo. **X-ray phase-contrast imaging with polychromatic sources and the concept of effective energy**. *Phys. Rev. A*, **87**(5):053838, 2013. 63, 130, 135, 138, 142

[77] Marco Endrizzi and Alessandro Olivo. **Absorption, refraction and scattering retrieval with an edge-illumination-based imaging setup**. *J. Phys. D. Appl. Phys.*, **47**(50):505102, 2014. 64, 107, 110

[78] M. Endrizzi, D. Basta, and A. Olivo. **Laboratory-based X-ray phase-contrast imaging with misaligned optical elements**. *Appl. Phys. Lett.*, **107**:124103, 2015. 64, 108, 110, 111

[79] L. Rigon, A. Astolfo, F. Arfelli, and R. H. Menk. **Generalized diffraction enhanced imaging: Application to tomography**. *Eur. J. Radiol.*, **68**:3–7, 2008. 64

[80] F. A. Vittoria, M. Endrizzi, P. C. Diemoz, A. Zamir, U. H. Wagner, C. Rau, I. K. Robinson, and A. Olivo. **X -ray absorption, phase and dark-field tomography through a beam tracking approach**. *Sci. Rep.*, **5**:16318, 2015. 64

[81] M. Endrizzi, F. A. Vittoria, L. Rigon, D. Dreossi, and A. Olivo. **X-ray Phase-Contrast Radiography and Tomography with a Multiaperture Analyzer**. *Phys. Rev. Lett.*, **118**:243902, 2017. 64

[82] P. C. Diemoz, F. A. Vittoria, C. K. Hagen, M. Endrizzi, P. Coan, E. Brun, U. H. Wagner, C. Rau, I. K. Robinson, A. Bravin, and A. Olivo. **Single-image phase retrieval using an edge illumination X-ray phase-contrast imaging setup**. *J. Synchrotron Radiat.*, **22**(4):1072–1077, 2015. 64, 68, 84, 127, 130

[83] E. L. Ritman. **Current status of developments and applications of micro-CT**. *Annu. Rev. Biomed. Eng.*, **13**(1):531–552, 2011. 65

[84] Z. Huang, K. Kang, Z. Li, P. Zhu, Q. Yuan, W. Huang, J. Wang, D. Zhang, and A. Yu. **Direct computed tomographic reconstruction for directional-derivative projections of computed tomography of diffraction enhanced imaging**. *Appl. Phys. Lett.*, **89**(4):041124, 2006. 65, 66

[85] C. K. Hagen, P. R. T. Munro, M. Endrizzi, P. C. Diemoz, and A. Olivo. **Low-dose phase contrast tomography with conventional x-ray sources.** *Med. Phys.*, **41**(7):070701, 2014. 67

[86] C. K. Hagen, P. C. Diemoz, M. Endrizzi, and A. Olivo. **The effect of the spatial sampling rate on quantitative phase information extracted from planar and tomographic edge illumination x-ray phase contrast images**. *J. Phys. D. Appl. Phys.*, **47**(45):455401, 2014. 67, 137, 147

[87] C. K. Hagen, M. Endrizzi, P. C. Diemoz, and A. Olivo. **Reverse projection retrieval in edge illumination x-ray phase contrast computed tomography**. *J. Phys. D. Appl. Phys.*, **49**:255501, 2016. 68

[88] Y. Chen, H. Guan, C. K. Hagen, A. Olivo, and M. A. Anastasio. **Single-shot edge illumination x-ray phase-contrast tomography enabled by joint image reconstruction**. *Opt. Lett.*, **42**(3):619, 2017. 68

[89] P.C. Diemoz, C.K. Hagen, M. Endrizzi, M. Minuti, R. Bellazzini, L. Urbani, P. De Coppi, and A. Olivo. **Single-Shot X-Ray Phase-Contrast Computed Tomography with Nonmicrofocal Laboratory Sources**. *Phys. Rev. Appl.*, **7**(4):044029, 2017. 68, 127, 128, 129, 130, 135, 146, 147

[90] J. L. Burton and J. Underwood. **Clinical, educational, and epidemiological value of autopsy.** *Lancet*, **369**(9571):1471–80, 2007. 70

[91] H. E. McHaffie, P. W. Fowlie, R. Hume, I. A. Laing, D. J. Lloyd, and A. J. Lyon. **Consent to autopsy for neonates.** *Arch. Dis. Child. Fetal Neonatal Ed.*, **85**(1):F4–F7, 2001. 70

[92] S. Thayyil, J. Cleary, N. Sebire, R. Scott, K. Chong, R. Gunny, C. Owens, O. Olsen, A. Offiah, H. Parks, L. Chitty, A. Price, T. Yousry, N. Robertson, M. Lythgoe, and A. Taylor. **Post-mortem examination of human fetuses: a comparison of whole-body high-field MRI at 9.4 T with conventional MRI and invasive autopsy.** *Lancet*, **374**(9688):467–75, 2009. 70, 71

[93] S. Thayyil, N. Sebire, L. Chitty, A. Wade, W. Chong, O. Olsen, R. Gunny, A. Offiah, C. Owens, D. Saunders, R. Scott, R. Jones, W. Norman, S. Addison, A. Bainbridge, E. Cady, E. De Vita, N. Robertson, and A. Taylor. **Post-mortem MRI versus conventional autopsy in fetuses and children: a prospective validation study.** *Lancet*, **382**(9888):223–33, 2013. 70, 71

[94] O. J. Arthurs, A. M. Taylor, and N. J. Sebire. **The less-invasive perinatal autopsy: current status and future directions**. *Fetal Matern. Med. Rev.*, **24**:45–59, 2013. 71, 85

[95] J. Mollenhauer, M. E. Aurich, Z. Zhong, C. Muehleman, A. A. Cole, M. Hasnah, O. Oltulu, K. E. Kuettner, A. Margulis, and L. D. Chapman. **Diffraction-enhanced X-ray imaging of articular cartilage.** *Osteoarthritis Cartilage*, **10**(3):163–71, 2002. 72, 84

[96] A. Sztrókay, P. C. Diemoz, T. Schlossbauer, E. Brun, F. Bamberg, D. Mayr, M. F. Reiser, A. Bravin, and P. Coan. **High-resolution breast**

tomography at high energy: a feasibility study of phase contrast imaging on a whole breast. *Phys. Med. Biol.*, **57**(10):2931–42, 2012. 73

[97] M. A. Beltran, D. M. Paganin, K. Uesugi, and M. J. Kitchen. **2D and 3D X-ray phase retrieval of multi-material objects using a single defocus distance.** *Opt. Express*, **18**(7):6423–36, 2010. 75, 128, 131, 132, 134, 141, 144

[98] M. A. Beltran, D. M. Paganin, K. K. W. Siu, A. Fouras, S. B. Hooper, D. H. Reser, and M. J. Kitchen. **Interface-specific x-ray phase retrieval tomography of complex biological organs**. *Phys. Med. Biol.*, **56**(23):7353–7369, 2011. 75, 128

[99] A. Horng, E. Brun, A. Mittone, S. Gasilov, L. Weber, T. Geith, S. Adam-Neumair, S. D. Auweter, A. Bravin, M. F. Reiser, and P. Coan. **Cartilage and Soft Tissue Imaging Using X-rays**. *Invest. Radiol.*, **49**(9):627–634, 2014. 78, 84, 141

[100] C. Parham, Z. Zhong, D. M. Connor, L. D. Chapman, and E. D. Pisano. **Design and implementation of a compact low-dose diffraction enhanced medical imaging system.** *Acad. Radiol.*, **16**(8):911–917, 2009. 83

[101] F. Pfeiffer, O. Bunk, C. David, M. Bech, G. Le Duc, A. Bravin, and P. Cloetens. **High-resolution brain tumor visualization using three-dimensional x-ray phase contrast tomography**. *Phys. Med. Biol.*, **52**(23):6923–6930, 2007. 84

[102] J. Keyriläinen, A. Bravin, M. Fernández, M. Tenhunen, P. Virkkunen, and P. Suortti. **Phase-contrast X-ray imaging of breast.** *Acta Radiol.*, **51**(8):866–884, 2010. 84

[103] P. Coan, F. Bamberg, P. C. Diemoz, A. Bravin, K. Timpert, E. Mutzel, J. G. Raya, S. Adam-Neumair, M. F. Reiser, and C. Glaser. **Characterization of Osteoarthritic and Normal Human Patella Cartilage by Computed Tomography X-ray Phase-Contrast Imaging**. *Invest. Radiol.*, **45**(7):437–444, 2010. 84

[104] Y. Zhao, E. Brun, P. Coan, Z. Huang, A. Sztrókay, P. C. Diemoz, S. Liebhardt, A. Mittone, S. Gasilov, J. Miao, and A. Bravin. **high resolution, low-dose phase contrast x-ray tomography for 3D diagnosis of human breast cancers**. *PNAS*, **109**(45):18290–18294, 2012. 84

[105] A. Tapfer, R. Braren, M. Bech, M. Willner, I. Zanette, T. Weitkamp, M. Trajkovic-Arsic, J. T. Siveke, M. Settles, M. Aichler, A. Walch, and F. Pfeiffer. **X-Ray Phase-Contrast CT of a Pancreatic Ductal Adenocarcinoma Mouse Model**. *PLoS One*, **8**(3):e58439, 2013. 84

[106] F. A. Vittoria, P. C. Diemoz, M. Endrizzi, L. Rigon, F. C. Lopez, D. Dreossi, P. R. T. Munro, and A. Olivo. **Strategies for efficient and fast wave optics simulation of coded-aperture and other x-ray phase-contrast imaging methods**. *Appl. Opt.*, **52**(28):6940–6947, 2013. 90, 114, 136

[107] S. J. Riederer, N. J. Pelc, and D. A. Chesler. **The Noise Power Spectrum in Computed X-ray Tomography**. *Phys. Med. Biol.*, **23**(3):446–454, 1978. 98

[108] K. Faulkner and B. M. Moores. **Analysis of x-ray computed tomography images using the noise power spectrum and autocorrelation function**. *Phys. Med. Biol.*, **29**(11):1343–1352, 1984. 98

[109] X. Tang, Y. Yang, and S. Tang. **Characterization of imaging performance in differential phase contrast CT compared with the conventional CT Noise power spectrum NPS (k)**. *Med. Phys.*, **38**(7):4386–4395, 2011. 98

[110] K. L. Boedeker, V. N. Cooper, and M. F. McNitt-Gray. **Application of the noise power spectrum in modern diagnostic MDCT : part I . Measurement of noise power spectra and noise equivalent quanta**. *Phys. Med. Biol.*, **52**:4027–4046, 2007. 98

[111] K. Ignatyev, P. R. T. Munro, R. D. Speller, and A. Olivo. **Effects of signal diffusion on x-ray phase contrast images.** *Rev. Sci. Instrum.*, **82**(7):073702, 2011. 103, 143

[112] T. Thuring, P. Modregger, B. R. Pinzer, Z. Wang, and M. Stampanoni. **Non-linear regularized phase retrieval for unidirectional X-ray differential phase contrast radiography**. *Opt. Express*, **19**(25):25545–25558, 2011. 124

[113] T. E. Gureyev, Y. I. Nesterets, A. W. Stevenson, P. R. Miller, A. Pogany, and S. W. Wilkins. **Some simple rules for contrast, signal-to-noise and resolution in in-line x-ray phase-contrast imaging.** *Opt. Express*, **16**(5):3223–3241, 2008. 129

[114] N. Otsu. **A Threshold Selection Method from Gray-Level Histograms**. *IEEE Trans. Syst. Man. Cybern.*, **9**(1):62–66, 1979. 141